

UCSF

UC San Francisco Electronic Theses and Dissertations

Title

Spatiotemporal Control of Cellular Signalling with Light

Permalink

<https://escholarship.org/uc/item/938935tz>

Author

Levskaya, Anselm C.

Publication Date

2009

Peer reviewed|Thesis/dissertation

Spatiotemporal Control of Cellular Signalling with Light

by

Anselm Levskaya

DISSERTATION

Submitted in partial satisfaction of the requirements for the degree of

DOCTOR OF PHILOSOPHY

in

Biophysics

in the

GRADUATE DIVISION

of the

UNIVERSITY OF CALIFORNIA, SAN FRANCISCO

Copyright 2009

by

Anselm Levskaya

Dedication and Acknowledgements

I should like to thank my triumvirate of graduate advisers: Chris Voigt, Wendell Lim, and Orion Weiner for countless hours of discussions regarding scientific matters both technical and strategic and an unending show of financial support and patience for a set of quite long-winded projects. I'd like to thank Bassem Al-Sady and the lab of Peter Quail at UC Berkeley for vital technical assistance and the gifts of many phytochrome and PIF constructs that were enabling for much of my work in eukaryotic system. I thank Kurt Thorn for assistance and advice on the use of the Nikon core facility's microscopes. Lastly, I'd like to thank Chris Anderson, Greg Kapp, and the members of the Voigt, Lim, and Weiner labs for untold hours of discussion and technical advice.

This thesis is composed of the four publications that I have been significantly involved with in some part:

Levskaya et al. Synthetic biology: engineering *Escherichia coli* to see light. *Nature* (2005) vol. 438 (7067) pp. 441-2

Temme et al. Induction and relaxation dynamics of the regulatory network controlling the type III secretion system encoded within *Salmonella* pathogenicity island 1. *J. Mol. Biol.* (2008) vol. 377 (1) pp. 47-61

Tabor et al. A synthetic genetic edge detection program. *Cell* (2009) vol. 137 (7) pp. 1272-81

Levskaya et al. Spatiotemporal Control of Cell Signalling Using a Light-Switchable Protein Interaction. *In press Nature* (2009)

Spatiotemporal Control of Cellular Signalling with Light

Genetically-encodable optical reporters, such as Green Fluorescent Protein, have revolutionized the observation and measurement of cellular states. However, the inverse challenge of using light to precisely control cellular behavior has only recently begun to be addressed; in recent years, semi-synthetic chromophore-tethered receptors and naturally-occurring channel rhodopsins have been used to directly perturb neuronal networks. The difficulty of engineering light sensitive proteins remains a significant impediment to the optical control of most cell-biological processes. I have focused my work over the last five years on the production of genetically-encoded light-sensitive reagents for the control of both bacterial and eukaryotic signalling networks. I have demonstrated minute-timescale control of bacterial transcriptional networks with engineered light-sensitive histidine kinases. I have also demonstrated the use of a new genetically encoded light-control system based on an optimized reversible protein-protein interaction from the phytochrome signaling network of *Arabidopsis thaliana*. Because protein-protein interactions are one of the most general currencies of cellular information, this latter system can in principle be generically used to control diverse functions. I show that this system can be used to precisely and reversibly translocate target proteins to the membrane with micrometer spatial resolution and second time resolution. I show that light-gated

translocation of the upstream activators of rho-family GTPases, which control the actin cytoskeleton, can be used to precisely reshape and direct the cell morphology of mammalian cells. The light-gated protein-protein interaction that has been optimized in this latter work should be useful for the design of diverse light-programmable reagents, potentially enabling a new generation of perturbative, quantitative experiments in cell biology.

Table of Contents

- 1 Prokaryotic Transcriptional Control (Synthetic Biology: Engineering E.coli to see Light.)
- 11 Analysis of a Complex Temporally-ordered Transcriptional Program in a Model Prokaryote (Induction and relaxation dynamics of the regulatory network controlling the type III secretion system encoded within Salmonella pathogenicity island.)
- 26 Using Light-control of Transcription as an Input for Complex Synthetic Spatial 'Programs' in Prokaryotes (A synthetic genetic edge detection program.)
- 36 Controlling Signal Transduction Cascades in Eukaryotes with Light (Spatiotemporal Control of Cell Signalling Using a Light-Switchable Protein Interaction.)

BRIEF COMMUNICATIONS

Engineering *Escherichia coli* to see light

These smart bacteria 'photograph' a light pattern as a high-definition chemical image.

We have designed a bacterial system that is switched between different states by red light. The system consists of a synthetic sensor kinase that allows a lawn of bacteria to function as a biological film, such that the projection of a pattern of light on to the bacteria produces a high-definition (about 100 megapixels per square inch), two-dimensional bacterial gene expression could be used to 'print' complex biological materials, for example, and to investigate signalling pathways through precise spatial and temporal control of their phosphorylation steps.

Plants and some bacteria use a class of protein photoreceptors known as phytochromes to control phototaxis, photosynthesis and the production of protective pigments¹⁻³. Photoreceptors are not found in enterobacteria, such as *Escherichia coli*, so we created a light sensor that functions in *E. coli* by engineering a chimaera that uses a phytochrome from a cyanobacterium.

A phytochrome is a two-component system that consists of a membrane-bound, extracellular sensor that responds to light and an intracellular response-regulator. The response-regulators of most phytochromes do not have DNA-binding domains and do not directly regulate gene expression, so we fused a cyanobacterial photoreceptor to an *E. coli* intracellular histidine kinase domain (Fig. 1a, and see supplementary information). This design was based on the well studied *E. coli* EnvZ–OmpR two-component system, which normally regulates porin expression in response to osmotic shock⁴. The EnvZ histidine kinase domain has been used for the construction of functional chimaeras^{5,6}, and a plant phytochrome has previously been used to construct a two-hybrid gene expression system in yeast.

To create the chimaera, we aligned members of the phytochrome family with EnvZ and identified potential functional crossover points between the *Synechocystis* phytochrome Cph1 and EnvZ. (For methods, see supplementary information.) The length and composition of the peptide that links a photoreceptor to its response-regulator can affect signal transduction^{5,6}, and we therefore constructed a series of chimaeras with variable linker lengths. The variants were transformed into a Δ EnvZ *E. coli* strain containing a chromosomal fusion between the OmpR-dependent *ompC* promoter and the *lacZ* reporter⁴, which

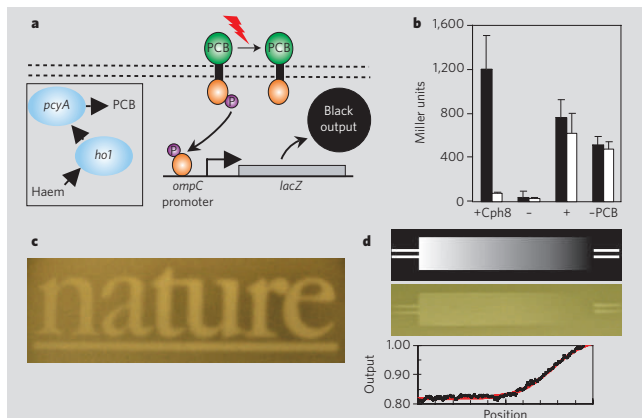


Figure 1 | Light imaging by engineered *Escherichia coli*. **a**, The chimaeric light receptor Cph8 contains the photoreceptor from Cph1 (green) and the histidine kinase and response-regulator from EnvZ–OmpR (orange); inset, conversion of haem to phycocyanobilin (PCB), which forms part of the photoreceptor. Red light drives the sensor to a state in which autophosphorylation is inhibited (right), turning off gene expression. For details of genes, see text **b**, Miller assay showing that Cph8 is active in the dark (black bars) in the presence of PCB and inactive in the light (white bars). There is no light-dependent activity in the absence of Cph8 (–) and there is constitutive activity when only the histidine kinase domain of EnvZ is expressed (+), or when the PCB metabolic pathway is not included (– PCB). **c**, When an image is projected on to a bacterial lawn, the *lacZ* reporter is expressed only in the dark regions. **d**, Transfer function of the circuit. As the intensity of the light is increased by using a light gradient projected from a 35-mm slide, the circuit output gives a graded response.

enzymatically produces a black compound.

The part of the photoreceptor that responds to light, phycocyanobilin, is not naturally produced in *E. coli*. We therefore introduced two phycocyanobilin-biosynthesis genes (*ho1* and *pcyA*) from *Synechocystis* that convert haem into phycocyanobilin⁸ (parts BBa_I15008, BBa_I15009; MIT Registry of Standard Biological Parts) (Fig. 1a, inset). Individual Cph1–EnvZ chimaeras were then activated at 37 °C for 4 h with broad-spectrum light and assayed for expression of the *lacZ* reporter. The chimaera Cph8 (BBa_I15010) produced a particularly strong response to light (Fig. 1b).

For bacterial photography, we grew a lawn of bacteria on agar. The *lacZ* reporter was visualized by addition of S-gal (3,4-cyclohexenoesculetin- β -D-galactopyranoside): LacZ catalyses the formation of a stable, insoluble, black precipitate from S-gal. Light repressed gene expression in the bacteria, giving a high-contrast replica of the applied image on

the biological film, in which light regions appeared light and dark regions were dark (Fig. 1c, and see supplementary information). The *lacZ* activity showed a graded response to increasing light intensity that was minimal in the brightest light (Fig. 1d).

Our creation of a novel genetic circuit with an image-processing function demonstrates the power and accessibility of the tool sets and methods available in the nascent field of synthetic biology. The principle of programmed light regulation should enable gene expression to be spatially and temporally controlled in individual cells and in populations, leading to potential application in bacterial microlithography, manufacture of biological material composites and the study of multicellular signalling networks.

Anselm Levskaya[†], Aaron A. Chevalier[†], Jeffrey J. Tabor[†], Zachary Booth Simpson[†], Laura A. Lavery[†], Matthew Levy[†], Eric A. Davidson[†], Alexander Scouras[†], Andrew D. Ellington[†]‡, Edward M. Marcotte[†]‡, Christopher A. Voigt^{*†§}||

*Biophysics Program, University of California, San Francisco, California 94143, USA
e-mail: cavoigt@picasso.ucsf.edu

†Center for Systems and Synthetic Biology and Institute for Cell and Molecular Biology, and ‡Department of Chemistry and Biochemistry, University of Texas, Austin, Texas 78712, USA

§Department of Synthetic Biology, Lawrence Berkeley National Laboratory, Berkeley, California 94720, USA

||Department of Pharmaceutical Chemistry, University of California, San Francisco, California 94107, USA

1. Yeh, K.-C., Wu, S.-H., Murphy, J. T. & Lagarias, J. C. *Science* **277**, 1505–1508 (1997).
2. Schmitz, O., Katayama, M., Williams, S. B., Kondo, T. & Golden, S. S. *Science* **289**, 765–768 (2000).
3. Davis, S. J., Vener, A. V. & Vierstra, R. D. *Science* **286**, 2517–2520 (1999).
4. Utsumi, R. *et al. Science* **245**, 1246–1249 (1989).
5. Jin, T. & Inoué, M. *J. Mol. Biol.* **244**, 477–481 (1994).
6. Kwon, O., Georgellis, D. & Lin, E. C. *J. Biol. Chem.* **278**, 13192–13195 (2003).
7. Shimizu-Sato, S., Huq, E., Tepperman, J. M. & Quail, P. H. *Nature Biotechnol.* **20**, 1041–1044 (2002).
8. Gambetta, G. A. & Lagarias, J. C. *Proc. Natl Acad. Sci. USA* **98**, 10566–10571 (2001).

Supplementary information accompanies this communication on Nature's website.

Competing financial interests: declared none.

doi:10.1038/nature04405

INSECT COMMUNICATION

'No entry' signal in ant foraging

Forager ants lay attractive trail pheromones to guide nestmates to food^{1,2}, but the effectiveness of foraging networks might be improved if pheromones could also be used to repel foragers from unrewarding routes^{3,4}. Here we present empirical evidence for such a negative trail pheromone, deployed by Pharaoh's ants (*Monomorium pharaonis*) as a 'no entry' signal to mark an unrewarding foraging path. This finding constitutes another example of the sophisticated control mechanisms used in self-organized ant colonies.

To investigate whether foragers lay a negative signal on the unrewarding branch of a trail bifurcation, we removed paper substrate from immediately after the fork on the unrewarding branch (the other branch led to a sucrose feeder) after it had been used by a trail-laying colony of ants. This paper substrate was transferred to the entrance of one branch of a similar set-up, in which both branches had previously led to sucrose and had been used by a second colony of ants. The other branch of the second set-up received a neutral control paper substrate (for details, see supplementary information). Foragers walking from the nest could choose either of the test branches or make a U-turn.

We found that 69% continued to walk away from the nest and make a branch choice. Of these, most (71%) chose the branch with the control substrate ($\chi^2=22.1$, d.f.=1, $n=137$, $P<0.001$); the remainder U-turned towards the nest on reaching the trail bifurcation. U-turns were more than four times as likely if the ant had contacted the unrewarding-branch substrate (55%) as opposed to the neutral-control substrate (13%) ($\chi^2=40.9$, d.f.=1, $n=200$, $P<0.0001$). Neither substrate came from a previously rewarding trail, so this result cannot be attributed to differences in positive-trail pheromone concentrations.

We next investigated the negative signal's location by taking substrate from five locations on a bifurcating trail that had one rewarding

and one unrewarding branch. These sections, along with neutral controls, were tested on unbranched foraging trails (see supplementary information) by noting whether individual foragers walking over them did a U-turn. Compared with ants on the control substrate, almost twice as many ants U-turned when walking on substrate from the unrewarding branch near the bifurcation (N_b) (19% and 34%, respectively; $P<0.001$) (Fig. 1a). However, U-turns were as frequent on substrate from the unrewarding branch end (N_e) (27%) as on the control (27%) (NS) (Fig. 1a). Ants U-turned less often on sections from the rewarding trail (stem S, 12%; feeder branch close to the bifurcation F_b , 12%; and feeder-branch end F_e , 13%). These values are significantly lower than those for the relevant control (S, $P<0.001$; F_b , $P<0.05$; F_e , $P<0.001$) (Fig. 1a).

In the same experiment, we also determined whether foragers could detect the negative signal before reaching the substrate on which it had been laid, using walking behaviour (zigzagging versus walking straight) as a bioassay. Our results show that significantly more ants zigzagged when approaching substrate from an unrewarding branch just after the bifurcation ($P<0.01$) or at the branch end ($P<0.05$) than did controls (Fig. 1b). Conversely, significantly fewer zigzagged when approaching substrate leading to the feeder (S, $P<0.01$; F_b , $P<0.05$; F_e , $P<0.05$) (Fig. 1b).

Our results show that Pharaoh's ants use a sophisticated trail system with a negative, repellent pheromone to mark unrewarding branches. The signal is concentrated at decision points — trail bifurcations⁵. As it is volatile, it provides advance warning — like human road signs situated before junctions. Across a trail network, the pheromone could help direct foragers to food by closing off unrewarding sections. Exactly how negative pheromones enhance foraging efficiency in trail networks is not known, but they might complement attractive trail pheromones^{6,7}

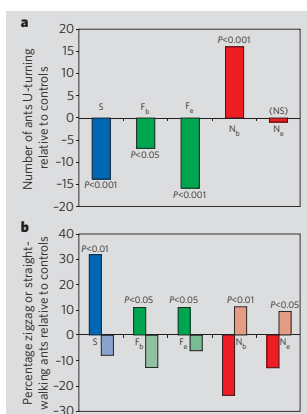


Figure 1 | Identifying the location of the negative pheromone. The ants' response is monitored by their walking behaviour, with U-turning or zigzagging on unbranched trails indicating detection. Test sections: S, 1 mm before bifurcation; F_b and N_b , 3 mm after bifurcation on feeder and non-feeder branches, respectively; F_e and N_e , 60 mm from bifurcation at the ends of feeder and non-feeder branches, respectively. (For details and chi-squared tests, see supplementary information.) **a**, Number of ants that U-turned while walking on different test sections, relative to controls. **b**, Percentage of straight-walking (left bars) or zigzagging (right bars) ants, relative to controls.

used by Pharaoh's ants in trail choice, or they could prevent strong positive feedback by attractive pheromones from locking the system into suboptimal solutions⁸.

Elva J. H. Robinson*, Duncan E. Jackson†, Mike Holcombe†, Francis L. W. Ratnieks*

*Laboratory of Apiculture and Social Insects, Department of Animal and Plant Sciences, University of Sheffield, Sheffield S10 2TN, UK
e-mail: e.robinson@dcs.sheffield.ac.uk

†Department of Computer Science, University of Sheffield, Sheffield S1 4DP, UK

1. Sumpter, D. J. T. & Beekman, M. *Anim. Behav.* **66**, 273–280 (2003).
2. Camazine, S. *et al. Self-Organization in Biological Systems* (Princeton Univ. Press, Princeton and Oxford, 2001).
3. Stickland, T. R., Britton, N. F. & Franks, N. R. *Information Processing in Social Insects* (eds Detrain, C., Deneubourg, J. L. & Pasteels, J. M.) 83–100 (Birkhäuser, Basel, 1999).
4. Britton, N. F., Stickland, T. R. & Franks, N. R. *J. Biol. Syst.* **6**, 315–336 (1998).
5. Jackson, D. E., Holcombe, M. & Ratnieks, F. L. W. *Nature* **432**, 907–909 (2004).
6. Sudd, J. H. *Br. J. Anim. Behav.* **5**, 104–109 (1957).
7. Jeanson, R., Deneubourg, J. L. & Ratnieks, F. L. W. *Physiol. Entomol.* **28**, 192–198 (2003).
8. Beckers, R., Deneubourg, J. L., Goss, S. & Pasteels, J. M. *Insectes Soc.* **37**, 258–267 (1990).

Supplementary information accompanies this communication on Nature's website.

Competing financial interests: declared none.

doi:10.1038/438442a

BRIEF COMMUNICATIONS ARISING online

www.nature.com/bcsee Nature contents.

Supplementary information

Materials and Methods

Strains and Plasmids. *Escherichia coli* RU1012 [MC4100 ara+ Φ (OmpC-*lacZ*) 10-25 $\Delta envZ::Kan^R$] was used to screen for active light receptors (obtained from G. Hazelbauer) (Utsumi *et al.*, 1989). This strain contains a chromosomally-encoded *ompC* reporter fused to a *lacZ* reporter. The chromophore phycocyanobilin (PCB) biosynthetic pathway was introduced into RU1012 via the pPL-PCB plasmid (obtained from J.C. Lagarias) (Gambetta and Lagarias, 2001), which was modified to replace the Kanamycin resistance with Ampicillin resistance. This plasmid contains a p15a origin of replication (*ori*). This plasmid contains the two-gene metabolic pathway *pcyA* and *hoI* to convert heme to PCB under the control of a *Para/lac* promoter. All *E. coli* strains were grown in Luria-Bertrani Media at 37°C. When used, antibiotics were at the following concentrations: Ampicillin (25 $\mu\text{g}/\text{mL}$), Chloramphenicol (34 $\mu\text{g}/\text{mL}$), Kanamycin (10 $\mu\text{g}/\text{mL}$). To induce PCB synthesis, arabinose was added to the media at a concentration of 2mM. The *cpH1* gene was isolated from the cyanobacteria *Synechocystis* PCC6803 (ATCC 27184) after growth and isolation of genomic DNA using the Sigma GenElute kit. Cyanobacterial strains were grown using cyanobacterial medium BG11 (ATCC medium 636) at 37° under broad-spectrum white light.

All of the bacterial images were recorded using *E. coli* strain CP919. CP919 is derived from RU1012, and carries an additional transposon insertion which knocks out

rbsB and rbsK (ribose binding protein and ribokinase) (Baumgartner et al., 1994). It was transformed with the light receptor and PCB plasmids to create a light-sensitive strain.

Plasmid Construction. The chimeric phytochromes were cloned into the pPROTet (Clontech). This plasmid contains a Chloramphenicol resistance gene and a ColE1 ori, which is compatible with the p15a ori pPL-PCB plasmid. This plasmid also contains the *tet* promoter, which was used to constitutively drive the expression of the chimeric phytochromes (all of the *E. coli* strains used do not contain the *tetR* gene). Prior to cloning the phytochrome fragments, the histidine kinase domain of *envZ* was ligated into pPROTet producing pPRO-HK. This domain consists of the C-terminal 229 amino acids that have been previously successful in constructing sensor chimeras (Utsumi *et al.*, 1989). The wild-type nucleotide sequence at this cut point encodes the NdeI restriction site. The *envZ* fragment was amplified from *E. coli* K12 genomic DNA using primers containing the NdeI and XbaI restriction sites and then cloned using these enzymes into the pPROTet plasmid. The phytochrome fragments were then inserted during a second ligation using the KpnI and NdeI sites.

Phytochrome Libraries. Using the pPRO-HK plasmid, a number of phytochrome signaling domains were inserted using the KpnI/NdeI restriction sites and tested for activity. First, we ran a CLUSTALW alignment of EnvZ against Cph1 (bioweb.pasteur.fr/seqanal/interfaces/clustalw-simple.html). A small library was then produced by varying

the number of Cph1 amino acids included (± 9 amino acids), while holding the number of EnvZ amino acids fixed. The most active chimera occurred with one less Cph1 amino acid than predicted from the sequence alignment. The active chimera contains the first 517 amino acids of Cph1 and the last 229 amino acids of EnvZ (cloned into pPRO-HK to form pCPH8). In addition, there is a single I \rightarrow V mutation at position 136 of the HK EnvZ domain. There were no amino acid substitutions in the Cph1 domain.

Screening Assay for Light Induction. RU1012 strains transformed with pPL-PCB and a plasmid encoding one of the chimeras were grown overnight (~12 hours) at 37°C and shaken at 250 rpm in 5 ml LB containing Ampicillin, Kanamycin, and Chloramphenicol. The overnights are then diluted 1:1000 into 2 mL fresh media containing antibiotics in two Falcon 24-well plates. One plate was exposed with a standard broad-spectrum glowing lamp (Venture Uni-FORM MH 100W/U/PS R Kr85 M90) and the other was wrapped in aluminum foil and kept in darkness. Both plates were maintained at 37°C. Each strain was then diluted 1:100 into a new, identical set of 24-well plates and the exposure procedure repeated for another 4 hours. The cells were then collected for analysis of ompC-promoter driven expression of β -galactosidase. To perform the Miller assay, 2 mL of the final culture were spun at 6000 rpm for 10 minutes in a microcentrifuge and then resuspended in 2mL of Z buffer (Miller, 1972). The cell density was recorded by measuring the OD₆₀₀ using a (HP8453) spectrophotometer. Then, 0.5 mL of the resuspended cells were diluted to 1mL in Z buffer and permeabilized by the

addition of 100 μ L of chloroform and 50 μ L of 0.1% SDS. This mixture was vortexed and allowed to equilibrate at 28°C for 5 minutes. Then, 0.2 mL of a solution containing 4 mg/ml *o*-nitrophenyl- β -galactoside (ONPG, Sigma) was added to the permeabilized cells and incubated at 28°C. The assay was allowed to proceed until sufficient yellow color developed to be seen by eye, the time was recorded and the assay quenched by the addition of 0.5 mL of 1M Na₂CO₃⁴ with vortexing. The chloroform was removed by centrifuging 1 mL of the quenched reaction at 13,200 rpm for 5 minutes. Finally, the OD₄₂₀ and OD₅₅₀ were measured. The Miller units were then calculated using the formula: $1000 \times [(OD_{420} - 1.75 \times OD_{550})] / [(Time\ of\ reaction) \times (volume\ of\ cells) \times OD_{600}]$. The final OD of the light and dark samples ranged from 0.5 – 0.6.

Bacterial Photography. *E. coli* strain CP919 was transformed with pPCB and pCPH8 for the bacterial photography experiments. 50 μ l of a 5 ml overnight culture grown to saturation was used to inoculate 50 ml of LB plus 4% Seaplaque Agarose (Cambrex, Pittsburg, PA) with appropriate antibiotics at 40°C. The LB agarose contained 15 mg of the LacZ substrate 3,4-cyclohexenoesculetin- β -D-galactopyranoside (S-Gal) and 25 mg of ferric ammonium citrate (Sigma Aldrich, St. Louis, MO). The molten cells/media were poured into a flat-surfaced mold, solidified, and grown at 37°C for 12 hours with the image projected onto the slab surface using a 100W Mercury vapor lamp, focusing on the slab surface (Supplemental Figure S1–S3). The Mercury lamp has power characteristics of .1331 watts/cm² from 620-680nm (active state of the phytochrome)

and .0132 watts/cm² from 715-755nm (inactive state of phytochrome), as determined by a EPP2000C Concave Grating spectrometer (Stellarnet, Oldsmar, FL). For laser repression, a 5mW red laser diode with an output of 0.45 watts/cm² from 640-680 nm and .0018 watts/cm² from 715-755 nm when projected across the slab surface.

Supplementary References

Baumgartner, J. W., Kim, C., Brissette, R. E., Inouye, M., Park, C., & Hazelbauer, G. L.,
J. Bacteriol., 176, 1157-1163 (1994).

Gambetta, G. A., & Lagarias, J. C., *Proc. Natl. Acad. Sci. USA*, **98**, 10566-10571 (2001).

Miller, J.H., *Experiments in Molecular Genetics*, Cold Spring Harbor Press, New York
(1972).

Utsumi, R., *et al.*, *Science*, **245**, 1246-1249 (1989).

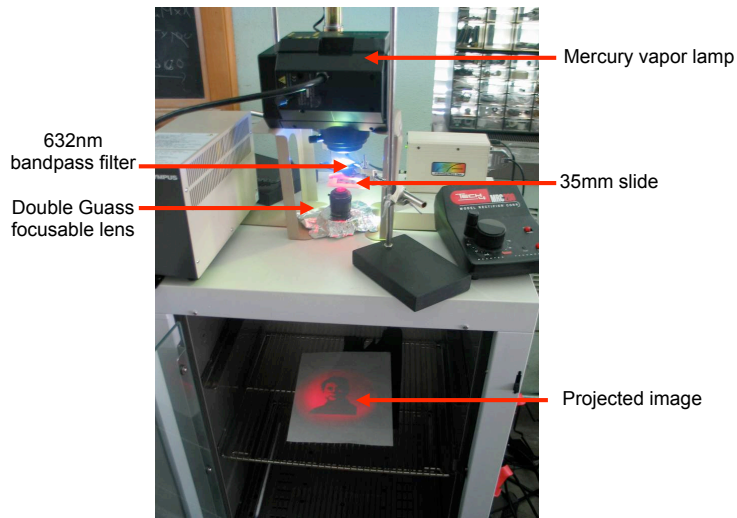


Figure S1: The bacterial “camera” used to record images. A 100W Mercury lamp was used as the light source for the image projector. The image projector consisted of a 25mm MVO Focusing Double Gauss macro imaging lens (Edmunds Optics, Barrington, NJ) with the Mercury lamp mounted 75mm above a 632nm Narrow Bandpass interference filter (Edmunds Optics, Barrington, NJ). Below the filter is a 35mm slide which has the image photo recorded on to it mounted on an electric actuator used for adjusting focus. The image is projected 38cm below the lens into an incubator and onto a large plate containing a lawn of bacteria.



Figure S2: *Escherichia Ellington*, an example of bacterial portraiture. The left panel shows the projected image and the right panel shows the resulting LacZ image recorded on the lawn of bacteria.



Figure S3: Bacterial photographs using different image masks. The top two rows show images recorded using inverse masks. The bottom row shows a negative control, where pCph8 was replaced with a plasmid expressing wild type EnvZ, and the cells were grown on S-gal agar and exposed to the 'Hello World' mask.



Induction and Relaxation Dynamics of the Regulatory Network Controlling the Type III Secretion System Encoded within *Salmonella* Pathogenicity Island 1

Karsten Temme^{1,2}, Howard Salis², Danielle Tullman-Ercek², Anselm Levskaya^{2,3}, Soon-Ho Hong² and Christopher A. Voigt^{1,2,3*}

¹UCSF/UCB Joint Graduate Group in Bioengineering, San Francisco, CA, USA

²Department of Pharmaceutical Chemistry, University of California-San Francisco, 600 16th Street, Suite 518, Box 2280, San Francisco, CA 94143-2280, USA

³Biophysics Program, San Francisco, CA, USA

Received 8 March 2007;
received in revised form
14 December 2007;
accepted 18 December 2007
Available online
28 December 2007

Bacterial pathogenesis requires the precise spatial and temporal control of gene expression, the dynamics of which are controlled by regulatory networks. A network encoded within *Salmonella* Pathogenicity Island 1 controls the expression of a type III protein secretion system involved in the invasion of host cells. The dynamics of this network are measured in single cells using promoter-green fluorescent protein (gfp) reporters and flow cytometry. During induction, there is a temporal order of gene expression, with transcriptional inputs turning on first, followed by structural and effector genes. The promoters show varying stochastic properties, where graded inputs are converted into all-or-none and hybrid responses. The relaxation dynamics are measured by shifting cells from inducing to noninducing conditions and by measuring fluorescence decay. The gfp expressed from promoters controlling the transcriptional inputs (*hilC* and *hilD*) and structural genes (*prgH*) decay exponentially, with a characteristic time of 50–55 min. In contrast, the gfp expressed from a promoter controlling the expression of effectors (*sicA*) persists for 110±9 min. This promoter is controlled by a genetic circuit, formed by a transcription factor (InvF), a chaperone (SicA), and a secreted protein (SipC), that regulates effector expression in response to the secretion capacity of the cell. A mathematical model of this circuit demonstrates that the delay is due to a split positive feedback loop. This model is tested in a Δ *sicA* knockout strain, where *sicA* is complemented with and without the feedback loop. The delay is eliminated when the feedback loop is deleted. Furthermore, a robustness analysis of the model predicts that the delay time can be tuned by changing the affinity of SicA:InvF multimers for an operator in the *sicA* promoter. This prediction is used to construct a targeted library, which contains mutants with both longer and shorter delays. This combination of theory and experiments provides a platform for predicting how genetic perturbations lead to changes in the global dynamics of a regulatory network.

Published by Elsevier Ltd.

Edited by J. Karn

Keywords: bistability; cascade; genetic circuit; invasion; stochastic

*Corresponding author. Box 2540, 1700 4th St, San Francisco, CA 94158-2330, USA. E-mail address: cavoigt@picasso.ucsf.edu.

Abbreviations used: gfp, green fluorescent protein; T3SS, type III secretion system; SPI, *Salmonella* Pathogenicity Island; rbs, ribosome-binding site; ODE, ordinary differential equation.

Introduction

Type III secretion is a virulence mechanism shared by many Gram-negative pathogens.^{13,25} It consists of a needle-like structure that crosses both the inner and the outer bacterial membranes and extends ~50 nm from the cell surface.⁴⁷ It functions to translocate effector proteins from the bacterial cytoplasm to the host cell, where they hijack signaling

processes and reorganize actin to facilitate endocytosis.²⁶ The type III secretion system (T3SS) is a complex molecular machine that requires more than 40 structural, effector, and chaperone genes, most of which are encoded together on a genomic island.²⁸ An internal regulatory network controls when and where each of the genes is expressed.⁴¹

Salmonella enterica contains two T3SS that facilitate the different stages of an infection. The needle encoded in *Salmonella* Pathogenicity Island (SPI) 1 can be induced in culture and is required for bacteria to invade mammalian cells.^{12,33} Once in the intracellular environment, SPI-1 is strongly repressed and SPI-2 is activated, encoding a different type III apparatus and new effectors.²⁴ Additional effectors exist at other genomic locations and in the *spv* operon on a virulence plasmid.^{20,48}

The network is organized such that environmental and cell state regulators converge on three transcription factors (HilC, HilD, and HilA) whose regulation is highly interconnected (Fig. 1).^{4,9,42,51,57} These transcription factors form a commitment circuit and differentially control the transcription of SPI-1 operons. HilA is required for the transcription of the *prg* operon, whose genes form the inner membrane ring and needle shaft.^{36,39,64} All three *hil* transcription factors induce the long *invFGEABCspaM-NOPQRSsicAsipBCDAiacPscPsptP* operon, which encodes the outer membrane ring and functional components, chaperones, translocators, and effectors.^{36,40,64} Two upstream promoters, which are activated by HilC/HilD and HilA, respectively, control the *inv* operon.^{2,20,40} In addition, there is an internal promoter upstream of the *sicA* gene, whose activity is controlled by InvF transcription factor and SicA chaperone.¹⁴

The SPI-1 network contains several regulatory motifs whose dynamics have been previously characterized.³ The network is centered on a four-tiered regulatory cascade.⁴¹ Transcriptional cascades have been shown to alter the timing and stochastic properties of gene expression.^{32,54,55} A coherent feedforward motif occurs when an input activates an intermediate regulator and together they turn on a downstream process (e.g., HilD activates HilC and together they activate HilA).⁵⁰ These motifs can filter short pulses of input and can delay the activation and relaxation of the circuit.^{34,44} The SPI-1 network contains several such interlocked feedforward motifs.²²

Several promoters also have interesting architectures that can convert the signaling properties of a pathway. The *hilA*, *invF*, and *prgH* promoters contain multiple cooperative binding sites.³⁹ In addition, the activator-binding sites of the *hilA* promoter can also be bound by repressor in a mutually exclusive manner.^{57,58} These properties have been shown previously to result in all-or-none activation, where individual cells in a population either fully express a gene or do not express it at all.^{6,56,61} The *inv* operon is also controlled by multiple promoters, which can act to integrate the properties of different input signals.^{2,40}

Positive feedback loops can amplify expression and introduce irreversibility into a switch.^{5,53,71} The commitment circuit formed by HilC/HilD/HilA contains several positive feedback loops.^{18,51} Another positive feedback loop is present in a SPI-1 circuit that upregulates the expression of effector proteins in response to the capacity of the cell to export proteins (Fig. 1).¹⁴⁻¹⁶ At the core of the circuit is the InvF transcription factor, which is only active

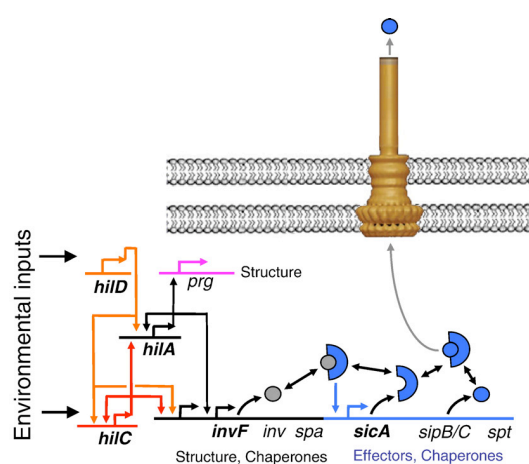


Fig. 1. The regulatory network encoded within SPI-1 is shown. The SPI-1 T3SS is induced by a number of environmental and cell state signals, such as osmolarity, Mg^{2+} , and extracellular phosphate, which differentially affect the regulators *hilD*, *hilC*, and *hilA*.²¹ These transcription factors coregulate each other and control different operons internal to SPI-1. Only HilA regulates the expression of genes forming the inner membrane ring and shaft (*prg*), but all three converge at two promoters controlling a long operon that begins with the *invF* gene. There is a promoter internal to this operon that is activated by InvF when bound to the SicA chaperone.¹⁴⁻¹⁶ The chaperone is sequestered by the SipC protein until it is exported, after which SicA can bind to InvF, leading to the up-regulation of additional effector proteins. The colors correspond to the temporal data shown in Fig. 2. The cryo electron microscopy structure of the needle complex is shown.⁴⁷

when bound to the SicA chaperone. Prior to the completion of functional needles, SipC binds to and sequesters SicA.⁶⁷ Once the needle is functional, SipC is exported and SicA is free to bind InvF. The InvF:SicA complex then activates the *sicA* promoter, thereby upregulating the expression of additional chaperones and effectors, including some that are encoded outside SPI-1.^{16,20} This circuit forms a “split” positive feedback loop, where SicA is internal to the loop but InvF is encoded outside the loop.

The cascade, feedforward/feedback motifs, and promoter architectures collectively determine the dynamics of the regulatory pathway. To characterize these dynamics, we construct plasmid-based reporters with transcriptional fusions between SPI-1 promoters and green fluorescent protein (gfp). Cells are shifted from noninducing to inducing conditions, and activation dynamics are measured in single cells using flow cytometry. These experiments reveal a temporal ordering in the activation of each promoter and a conversion between graded and all-or-none responses. After induction, the cells are shifted into noninducing conditions, and the decay of fluorescence is measured. There is a pronounced delay in the decay of gfp expressed from the promoter controlling effector expression (*sicA*). In contrast, the gfp from the other SPI-1 promoters decays rapidly and exponentially. Genetic mutants and a mathematical model are used to demonstrate that the delay is due to the split positive feedback loop formed by InvF and SicA. The model is used to predict how the delay can be varied by changing a biochemical parameter. This prediction is confirmed by applying random mutagenesis to an operator and by measuring the change in relaxation delay. Together, the experiments and theory provide a quantitative framework for studying the dynamics of this virulence pathway.

Results

Activation dynamics of the SPI-1 regulatory network

A series of reporter plasmids consisting of transcriptional fusions between four SPI-1 promoters and gfp is constructed (see Materials and Methods). The *hilC*, *hilD*, *prgH*, and *sicA* promoters were chosen to be representative of transcriptional inputs, T3SS structural genes, and effectors, respectively. These plasmids are used in parallel growth experiments³⁵ in *Salmonella typhimurium* SL1344 to measure the network dynamics in response to shifts in environmental conditions.

The SPI-1 genes are induced when *Salmonella* enters stationary phase in Luria-Bertani (LB) broth.^{38,43} This induction is dependent on the concentration of NaCl. SPI-1 is not induced in 0.085 M NaCl (L-broth) and is maximally induced in 0.3 M NaCl (inducing medium). To induce the SPI-1 genes, *Salmonella* cultures are grown overnight in L-broth and then diluted into the inducing medium (see

Materials and Methods). As the culture grows, aliquots are taken every half hour, and expression is stopped by adding kanamycin and by putting the cells on ice. The samples are then analyzed for fluorescence using flow cytometry. Single-cell experiments are critical when only a subset of the population is active, as has been observed previously for SPI-1 genes.^{10,30}

The average gated fluorescence is shown in Fig. 2 as a function of cell density (OD_{600}). As the cell density increases, the *hilD* and then the *hilC* promoters turn on first. Next, the *prgH* promoter, which controls the expression of T3SS structural components, is activated. This delay is consistent with the transcriptional cascade and feedforward loops, which can act to implement an input threshold that must be reached before downstream promoters are activated.³ Finally, the *sicA* promoter, which controls the expression of chaperones, effectors, and translocators, is induced. A similar transcriptional ordering has been observed during the assembly of the flagella basal body in *Escherichia coli*³⁵ and *Caulobacter crescentus*.³⁷

Different promoters in the SPI-1 network also generate different stochastic effects (Fig. 3). Both transcriptional inputs (*HilC* and *HilD*) follow a

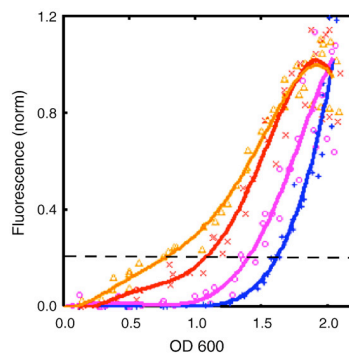
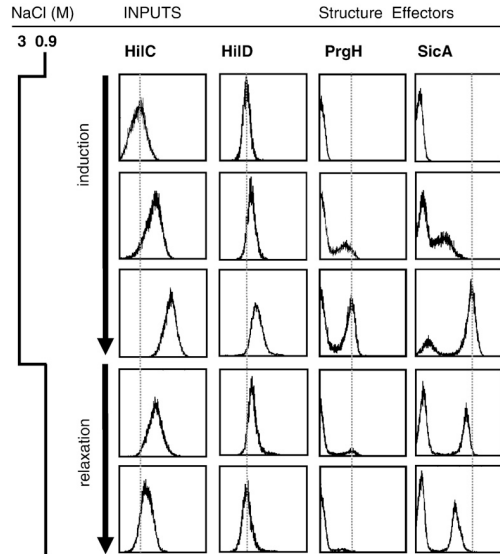


Fig. 2. The SPI-1 promoters are induced in a temporal order. The *hilD* (orange), *hilC* (red), *prgH* (purple), and *sicA* (blue) promoters are transcriptionally fused to gfp and introduced into cells on a plasmid. Cells are grown in noninducing media (L-broth) and diluted into inducing media, and fluorescence is measured in single cells as a function of density (OD_{600}). The average gated fluorescence of the population is calculated for the fraction of the population that turns on at the end of the induction experiment. The average is then normalized by the maximum.³⁵ The data represent four replicate experiments performed on different days for each promoter. Each data point is an aliquot from these 16 growth experiments. The lines are drawn for each promoter using a polynomial averaging algorithm. The dashed line is drawn as a reference for the point when the promoter reaches 20% of its maximum.



prgH promoters decays rapidly to the preinduced level. However, expression from these *sicA* promoter persists strongly. After dilution in L-broth, time points are shown after 50 and 140 min. The dashed lines are drawn as a guide to the eye.

graded induction, where the entire population uniformly turns on expression under inducing conditions. In contrast, the *prgH* promoter, which controls structural genes, is activated in an all-or-none manner, where individuals in the population either fully express this operon or do not express it at all.⁵⁰ The fraction of the population expressing *prg* genes increases as the population is induced. The architectures of the *hilA* and *prgH* promoters contain motifs that have been previously shown to be able to convert a graded input into an all-or-none output.^{6,56,57} The *sicA* promoter, which controls the expression of effectors, has both graded and all-or-none properties. Only a fraction of the population turns on, but that population increases in fluorescence by 200-fold as cells are induced.

Relaxation dynamics of the SPI-1 regulatory network

The regulatory motifs present in the SPI-1 network could also impact the inactivation of the network when the input signal is removed.³ In particular, the presence of positive feedback loops and feedforward motifs can impact relaxation time.^{5,34} Thus, experiments were performed to determine how the network relaxes when cells are shifted into an environment where SPI-1 is repressed. After SPI-1 is fully induced, an aliquot of bacteria is washed and rediluted into noninducing L-broth, and time points are taken every half hour (see Materials and

Methods). As before, the fluorescence in individual cells is analyzed by flow cytometry. After dilution, the fluorescent reporters expressed from the *hilC*, *hilD*, and *prgH* promoters decay rapidly, whereas expression from the *sicA* promoter persists (Fig. 3). The *gfp* expressed from the *hilC* and *hilD* promoters decays with a half-life of 55 ± 6 and 50 ± 14 min, respectively (Fig. 4). The *gfp* expressed from the *prgH* promoter, which controls the expression of structural genes, also degrades with a half-life of 50 ± 11 min. Because a stable variant of *gfp* is used, the primary contributor to fluorescence decay is dilution due to cell division. Indeed, for all three promoters, the decay fits a simple exponential model, which appears as a linear fit on a semilog plot. The *sicA* promoter exhibits approximately a 1-h delay, with a half-life of 110 ± 9 min (Fig. 4). In contrast to the upstream promoters, the decay does not fit an exponential model, implying that it follows nonlinear kinetics, as would be expected from a positive feedback loop. It is noteworthy that the maximum fluorescence from the *hilC* and *sicA* promoters are nearly identical prior to dilution, thus eliminating any potential nonlinear effects due to fluorescence as the source of the delay.

Methods). As before, the fluorescence in individual cells is analyzed by flow cytometry.

After dilution, the fluorescent reporters expressed from the *hilC*, *hilD*, and *prgH* promoters decay rapidly, whereas expression from the *sicA* promoter persists (Fig. 3). The *gfp* expressed from the *hilC* and *hilD* promoters decays with a half-life of 55 ± 6 and 50 ± 14 min, respectively (Fig. 4). The *gfp* expressed from the *prgH* promoter, which controls the expression of structural genes, also degrades with a half-life of 50 ± 11 min. Because a stable variant of *gfp* is used, the primary contributor to fluorescence decay is dilution due to cell division. Indeed, for all three promoters, the decay fits a simple exponential model, which appears as a linear fit on a semilog plot.

The *sicA* promoter exhibits approximately a 1-h delay, with a half-life of 110 ± 9 min (Fig. 4). In contrast to the upstream promoters, the decay does not fit an exponential model, implying that it follows nonlinear kinetics, as would be expected from a positive feedback loop. It is noteworthy that the maximum fluorescence from the *hilC* and *sicA* promoters are nearly identical prior to dilution, thus eliminating any potential nonlinear effects due to fluorescence as the source of the delay.

Reconstitution of *sicA* with and without positive feedback

There are two regulatory mechanisms that together lead to persistence in effector expression.

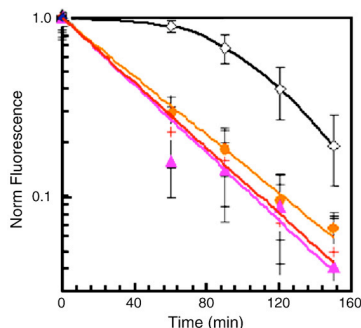


Fig. 4. Expression from the *sicA* promoter persists after cells are shifted into noninducing conditions. Cells are grown in inducing media (0.3 M NaCl LB broth) until the network is fully activated after 400 min (see Materials and Methods). Cells are then shifted into noninducing media (0.085 M NaCl LB broth) and grown for 150 min. The decay of fluorescence is shown after the cells are shifted into noninducing conditions ($t=0$ min). The fluorescence values are normalized by the maximum fluorescence prior to dilution. On a semilog plot, exponential decay appears as a straight line, as is the case for the *hilC* (orange circles), *hilD* (red +), and *prgH* (pink triangles) promoters. There is a significant delay in the decay of the *sicA* promoter (white diamonds). The straight lines are the best fitted to an exponential equation, as determined using linear regression algorithm. It is noteworthy that the *sicA* and *hilC* promoters have almost equal fluorescence prior to the shift to noninducing conditions. Each data point represents the average of four experiments performed on different days, and the standard deviation of these experiments is shown as error bars.

First, the *sicA* promoter is activated by SicA:InvF multimers.¹⁵ This forms a split positive feedback loop because InvF is encoded upstream of the *sicA* promoter and outside the loop (Figs. 1 and 6). Positive feedback loops can lead to a delay in the deactivation of a circuit. A second mechanism is continued leaky secretion due to a delay in the loss of functional T3SS structures from the cells. Leaky secretion continues to allow free SicA to be available for binding InvF. It is expected that both leaky secretion and a feedback loop are required for the effector expression to persist.

To assess the role of the feedback loop in the delay, a Δ *sicA* knockout strain, which eliminates the feedback loop, was obtained.¹⁵ In this knockout strain, expression from the *sicA* promoter is completely abolished (Fig. 5b, PBAD30) (see Materials and Methods). The feedback loop can be reconstituted by introducing the *sicA* promoter and the *sicA* gene on a plasmid (Fig. 5a, P30.psicA.sicA). This plasmid is based on the p15a origin of replication and is cotransformed with the ColE1-based *sicA* reporter plasmid. The reconstituted feedback loop recovers wild-type expression from the *sicA* promoter (Fig.

5b). The delay that occurs when the network relaxes is slightly longer (165 ± 22 min) than the wild-type feedback loop, which may be the result of reconstituting the loop on a multicopy (p15a origin) plasmid. However, the maximum fluorescence observed from the *sicA* reporter does not increase significantly.

A second plasmid was designed to complement the expression of *sicA*, but to eliminate the positive feedback loop. To complement *sicA*, a plasmid that contains the *sicA* gene under the control of an arabinose-inducible promoter was constructed (Fig. 5a, PBAD30.sicA). Here, *sicA* is no longer under the control of the *sicA* promoter; thus, the feedback loop has been broken but the network can still be activated by adding arabinose to the media. The network is induced by growing cells in the presence of arabinose, and relaxation is measured by shifting cells into media lacking arabinose (see Materials and Methods). An advantage of using the arabinose-inducible system is that this strain retains the arabinose utilization operon. Thus, the addition of arabinose produces a pulse of expression that reaches a peak 60 min after induction and is completely off 140 min after induction (not shown). This eliminates any potential positive feedback effects that could occur in the inducible system itself. The pulse of activity is uniform throughout the cell population.

Constructing the arabinose-inducible plasmid required variation of the ribosome-binding site (rbs) controlling *sicA* expression. Initially, a strong rbs was used†. This construct produced a constitutively active variant where, in the absence of arabinose, sufficient SicA was expressed through leaky transcription to turn on the *sicA* promoter on the reporter plasmid (not shown). A weak rbs was then tested (BBa_B0033), producing the opposite problem where, even in the presence of arabinose, too little SicA was expressed and the network did not turn on. Finally, an intermediate rbs (BBa_B0032), which was just right, was used. In the absence of arabinose, there is only a slight shift in the fluorescence recorded from the *psicA_gfp* reporter (Fig. 5b). When 1.3 mM arabinose is added to the inducing media, the expression from the *sicA* promoter reporter reaches the same fluorescence as wild type.

Growth induction and dilution experiments were performed to assay the impact of the positive feedback loop on the relaxation of expression from the *sicA* promoter. The arabinose inducer is added to the media after 150 min (see Materials and Methods). This roughly mimics an alternative regulatory structure where *sicA* is regulated by a cascade with InvF as an upstream regulator, as opposed to one containing a positive feedback loop (Fig. 6, Topology 2). After the network is fully induced, the cells are diluted into L-broth lacking arabinose, and the relaxation dynamics are measured. While the inducible construct achieves the same level of

† Part BBa_B0030 from <http://parts.mit.edu>

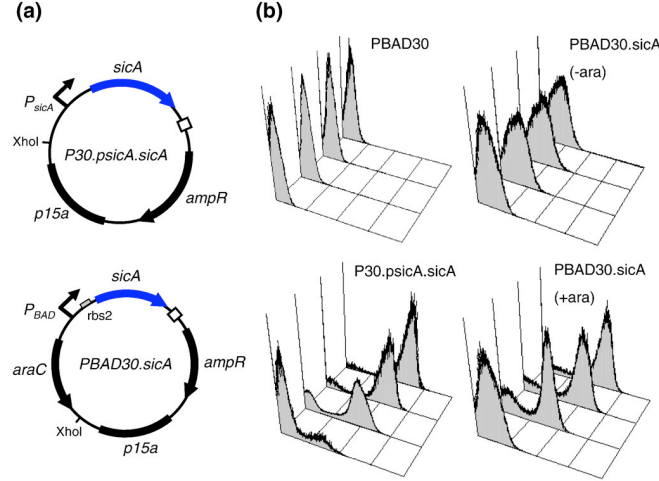


Fig. 5. An inducible *sicA* plasmid was constructed and tested for complementation in a $\Delta sicA$ knockout strain. (a) To reconstitute the feedback loop, the *sicA* promoter and gene were cloned together from the *Salmonella* genome and ligated into PBAD30 at an introduced XhoI site that eliminates the *araC* gene and the P_{BAD} promoter (top). To create an inducible system without the feedback loop, the *sicA* gene was cloned into the PBAD30 plasmid (bottom). Different *rbs* were tested to obtain an inducible construct. (b) Cytometry data are shown for the $\Delta sicA$ knockout containing the *psicA_gfp* reporter on a ColE1 plasmid. Data are shown (bottom to top) 2, 4, 6, and 8 h after the shifting of the cells into inducing conditions. No activity from the *sicA* promoter was observed when $\Delta sicA$ cells carried the empty PBAD30 plasmid as a control (top left). When the *sicA* gene is driven by the wild-type *sicA* promoter (P30.psicA.sicA), induction is recovered (bottom left). When the *sicA* gene is fused to an arabinose-inducible promoter (PBAD30.sicA), the *sicA* promoter is induced in the presence of 1.33 mM arabinose (bottom right), but not in the absence of arabinose (top right).

activation during induction (Fig. 5b), the fluorescence rapidly decays after cells are shifted into media lacking the inducer. The delay fits an exponential model with a half-life of 51 ± 5 min, which is equivalent to what is observed for the *hilC*, *hilD*, and *prgH* promoters (Fig. 7). The delay returns when the full feedback loop is reconstituted on the plasmid. Together, these experiments demonstrate that the split positive feedback loop is required for the observed relaxation delay.

Mathematical model of the SicA:InvF genetic circuit

A simple mathematical model of the SicA:InvF positive feedback loop is constructed to quantify the observed relaxation dynamics. A schematic of the circuit and biochemical parameters is shown in Fig. 6. The model is abstracted to describe a genetic circuit containing three proteins. The transcription factor *X* (InvF) is activated when bound by chaperone *Y* (SicA). The chaperone also binds to the effector protein to be secreted, *Z* (SipC). The formation of protein complexes is assumed to be fast with respect to transcription and translation. This leads to a set of three ordinary differential

equations (ODEs) that capture the change in the total number of each protein (X_T , Y_T , and Z_T) in the cell:

$$\frac{dX_T}{dt} = \alpha_x k_0 - \gamma_x (X_T - C_{XY}) - \gamma_{xy} C_{XY} \quad (1)$$

$$\frac{dY_T}{dt} = a_y \left(\eta k_0 + k_1 \frac{C_{XY}}{K + C_{XY}} \right) - \gamma_y (Y_T - C_{XY} - C_{YZ}) - \gamma_{xy} C_{XY} - \gamma_{yz} C_{YZ} \quad (2)$$

$$\frac{dZ_T}{dt} = a_z \left(\eta k_0 + k_1 \frac{C_{XY}}{K + C_{XY}} \right) - \gamma_z (Z_T - C_{YZ}) - \gamma_{yz} C_{YZ} - k_z C_{YZ} \quad (3)$$

where the parameters are defined in Table 1 and shown in Fig. 6. The number of *X:Y* and *Y:Z* complexes is given by the relationships $C_{XY} = K_{XY} X_0 Y_0$ and $C_{YZ} = K_{YZ} Y_0 Z_0$, where K_{XY} and K_{YZ} are equilibrium constants, and X_0 , Y_0 , and Z_0 are the numbers of unbound proteins. In addition, there are three conservation relationships for the total number of each protein: $X_T = X_0 (K_{XY} Y_0 + 1)$, $Y_T = Y_0 (K_{XY} X_0 + K_{YZ} Z_0 + 1)$, and $Z_T = Z_0 (K_{YZ} Y_0 + 1)$. Here, we assume that *X* (InvF) and *Y* (SicA) form a 1:1

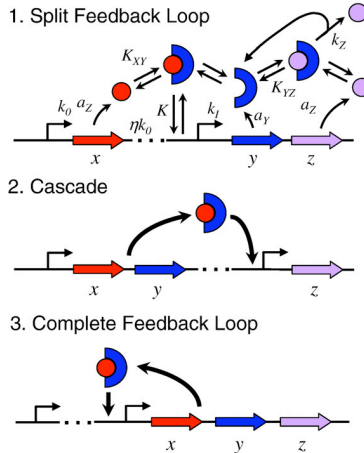


Fig. 6. A generalized schematic of the secretion-control circuit is shown for the topology that appears in *Salmonella* and for two alternative topologies (Topologies 2 and 3). Topology 1 shows the split positive feedback loop motif, where the transcription factor X (InvF) appears external to the feedback loop, but the activating chaperone y (SicA) is internal to the loop. The parameters used in the model are shown (Eqs. (1)–(3) and Table 1). Topology 2 is a simple cascade where both the transcription factor and the chaperone are outside the internal promoter, thus eliminating any feedback. This topology is roughly recreated when *sicA* is placed under inducible control and inducer is added at the time when *invF* is expressed (Figs. 5a and 7). Topology 3 is a complete feedback loop, where all of the necessary components are internal to the loop.

complex. It has been proposed that SicA could interact with InvF as a dimer.¹⁶ If this turns out to be the case, then bistability could be introduced into the model, although even then the bistability occurs in a very narrow slice of parameter space due to the split nature of the feedback loop (not shown).

To solve the equations, the network is initially induced by setting $k_0=1.0$ transcripts/min (see Materials and Methods). Once the network reaches steady state, the shift to noninducing conditions is simulated by stopping transcription from the upstream promoter ($k_0=0$). The relaxation of the network is then recorded. The presence of the positive feedback loop yields the observed delay (Fig. 7). Importantly, the activity of the feedback loop requires continued secretion from the T3SS ($k_z>0$). When there is no secretion, the delay is eliminated (as the secretion rate constant $k_z\rightarrow 0$ in Fig. 8).

When *sicA* is knocked out of the genome and reconstituted on the P_{BAD} inducible plasmid, this produces a circuit architecture resembling a cascade (Fig. 6, Topology 2). The feedback loop encoded in

the *sicA* promoter is not present, and it is predicted that this would reduce the observed delay. To simulate P_{BAD} data, the first term of Eq. (2) is changed to $\alpha_y k_0$; otherwise, the equations remain the same. This has the effect of decreasing the delay, which is observed in the experiments (Fig. 7).

Robustness and evolvability of the SicA:InvF genetic circuit

The mathematical model is used to perform a robustness analysis for the circuit.⁶⁸ Starting from the set of nominal parameter values (Table 1), each parameter is independently varied through a physiologically relevant range. For each parameter set, Eqs. (1)–(3) are solved, and secretion-dependent induction and timescale for the delay in deactivation are measured (Fig. 8).

Some combinations of parameters result in a circuit that can no longer be induced when secretion becomes active. To keep track of this, the expression from the *sicA* promoter is recorded for cells that are secreting (upper green lines) and compared to the expression when cells are not secreting (lower red lines). When both of these curves are high or low, the

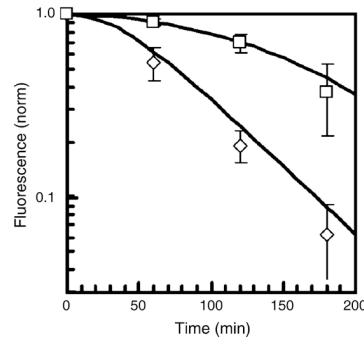


Fig. 7. The persistence of expression from the *sicA* promoter is eliminated by disruption of the positive feedback loop. Data are shown for the $\Delta sicA$ deletion mutant, where the *sicA* gene is complemented either by an inducible construct (Fig. 5a, $P_{BAD30.sicA}$) or under the control of the *sicA* promoter ($P_{30.psicA.sicA}$). Cells are grown in inducing conditions and then shifted into noninducing conditions ($t=0$ min), and the decay in fluorescence is measured. When the *sicA* promoter is under the control of an inducible promoter, the total fluorescence from the reporter reaches approximately the same maximum (Fig. 5b), but the delay is eliminated (diamonds). When the feedback loop is reconstituted on the plasmid, the delay is recovered (squares). The lines represent the fit to the model (Eqs. (1)–(3) and Table 1). Each data point is the average of six experiments performed on different days, and error bars represent the standard deviation. The data are normalized by the maximum fluorescence under inducing conditions.

Table 1. Model parameters

| Name | Description | Value | Units |
|-------------------------|---|-------|-----------------------------------|
| k_0 | Transcription rate of external promoter | 1 | transcripts min^{-1} |
| k_1 | Transcription rate of internal promoter ^a | 22 | transcripts min^{-1} |
| η | Efficiency of transcriptional read-through ^b | 0.01 | |
| α_x | X proteins produced per transcript ^c | 12 | proteins transcript ⁻¹ |
| α_y | Y proteins produced per transcript ^d | 14 | proteins transcript ⁻¹ |
| α_z | Z proteins produced per transcript ^e | 90 | proteins transcript ⁻¹ |
| γ_x, γ_{xy} | Degradation rate of X and XY complexes ^d | 0.022 | min^{-1} |
| γ_Y | Degradation rate of $Y^{a,c}$ | 0.046 | min^{-1} |
| γ_z | Degradation rate of Z^f | 0.139 | min^{-1} |
| γ_{zy} | Degradation rate of ZY complexes ^{f,g} | 0.022 | min^{-1} |
| K_{xy} | Equilibrium dissociation constant for XY dimers ^{a,h} | 1700 | nM |
| K_{yz} | Equilibrium dissociation constant for YZ dimers ^{h,i} | 28 | nM |
| k_z | Secretion rate of Z ^j | 0.1 | min^{-1} |
| K | Equilibrium dissociation constant of XY to the internal promoter ^h | 33 | nM |

^a These data were fitted to the experimental data shown in Fig. 7 (Materials and Methods). The remainder was fixed to values estimated from the literature.

^b This parameter captures the probability that an mRNA transcribed from the upstream promoter also encodes the *sicA* gene. The two genes are encoded 25 kb apart.

^c The production rate is set to reach a steady state of 6000–10,000 SipC proteins/cell. The intracellular concentration of SipA has been measured to be 6000 ± 3000 molecules/cell.⁵⁹

^d Corresponds to a ~32-min *in vivo* half-life. SicA does not affect the stability of InvF *in vivo*.¹⁶

^e The degradation rate of SicA is set to a half-life of 15 min.

^f In the absence of chaperone, the SipC protein degrades rapidly *in vivo*. This rate has been shown to range between 2 and 10 min *in vivo* in *Salmonella*⁶⁰ and *Shigella*.⁴⁹ Here, the rate is chosen to yield a half-life of 5 min.

^g The SipC protein is stabilized when bound to SicA.⁶⁷ In the presence of SicA, the *in vivo* half-life of SipC has been measured to be ~30 min. The monomeric form of SipC interacts with SipB, greatly increasing its degradation rate. Dilution is the primary mode of degradation, so this half-life reflects the cell division time. For the analogous system in *Shigella*, IpaC degrades in the cytoplasm with a half-life of ~5 min, but is stabilized when bound to IpgC (>20 min).^{7,49}

^h Assumes an intracellular volume of 10^{-15} L. The units are converted from concentration to molecules for Eqs. (1)–(3).

ⁱ The SipC:SicA binding affinity has been measured.³²

^j The rate of IpaC (homologous to SipC) secretion has directly been measured to be 0.17 min^{-1} in *Yersinia*.²³ The secretion rate of SipA was similarly measured and found to be 0.06 min^{-1} .⁵⁹

circuit is either always on or always off, independent of secretion. The difference between these curves indicates the degree to which the circuit can be induced by secretion. Some of the parameters, such as the degradation rate of free SicA (γ_Y), are robust (Fig. 8). In contrast, other parameters only have narrow regions that result in functional circuits, including the degradation rate of SicA:SipC complexes (γ_{yz}), which needs to be slow.

The delay in the deactivation dynamics of each parameter set is also recorded. The timescale is defined as the time required for half of the maximum fluorescence to degrade ($\tau_{1/2}$). Some of the parameters that are relatively robust, such as the expression rate of SipC (a_z), have almost no effect on the delay (Fig. 8). The only parameter that has a significant effect on the delay is the binding constant (K) for InvF:SicA binding to the internal *sicA* promoter. By varying this parameter over a physiologically relevant range, the model predicts that the delay can be varied from 1 h (where the delay to feedback is eliminated) to 4 h and still produce a

secretion-inducible circuit. In essence, this parameter could act as an evolutionary “tuning knob” where mutations could control how long protein expression persists after the network is deactivated.

To test this prediction of the model, the binding constant K was varied experimentally by mutating the known SicA:InvF operator in the *sicA* promoter.¹⁶ Targeted random mutagenesis was used to vary the sequence of the operator on the plasmid containing the reconstituted feedback loop (Fig. 5a, P30.psicA.sicA) in the $\Delta sicA$ strain (see Materials and Methods). The relaxation dynamics of seven sequenced mutants were measured (Fig. 9a). A remarkable diversity of relaxation times was obtained from this small library. The fastest mutant has $\tau_{1/2} = 78 \pm 17$ min, which is only slightly slower than for the *hilC*, *hilD*, *prgH*, and PBAD.sicA decay times (Fig. 9b). Interestingly, mutants with slower decay times were also obtained, with the slowest being $\tau_{1/2} = 210 \pm 33$ min. Each relaxation trajectory was fitted with the model to obtain the predicted binding constant K (Fig. 9a). It is intriguing that such

Fig. 8. A robustness analysis of the model is performed. Each parameter is independently varied from the nominal set (Table 1). For each set of parameters, Eqs. (1)–(3) are solved, and three values are recorded from the simulation: the maximum fluorescence without secretion (top graph, red line), the maximum fluorescence with secretion (top graph, green line), and the half-life for the decay of fluorescence ($\tau_{1/2}$; bottom graph). Very few of the parameters have the capacity to affect the decay half-life without resulting in a circuit that cannot be induced by secretion. Note that when there is no secretion ($k_z = 0$), the positive feedback loop is broken, and the delay is eliminated. The units for the parameters are provided in Table 1.

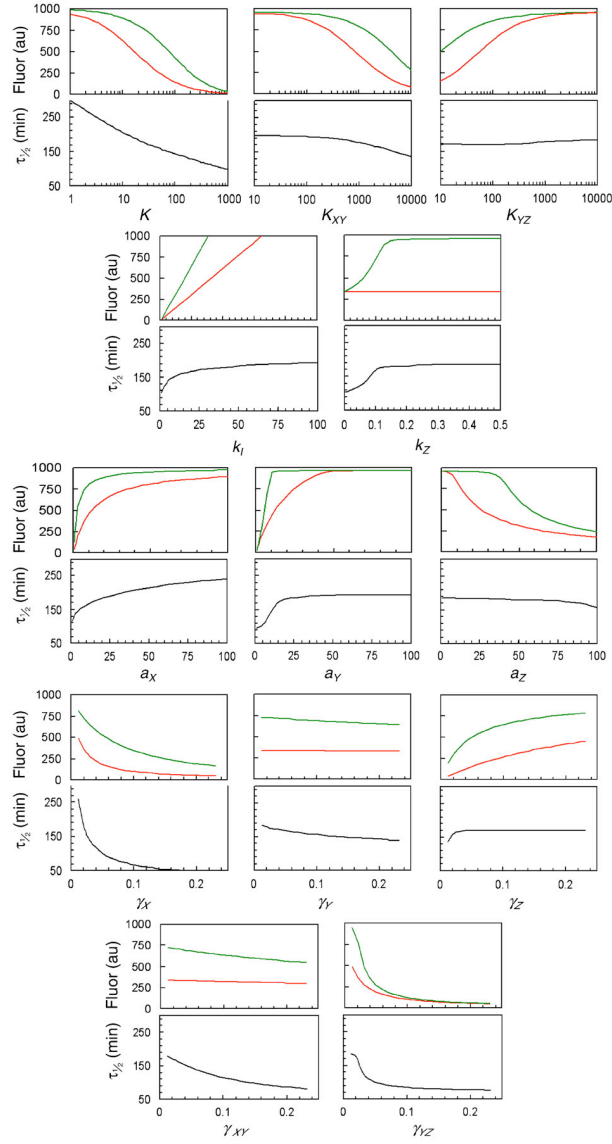


Fig. 8 (legend on previous page)

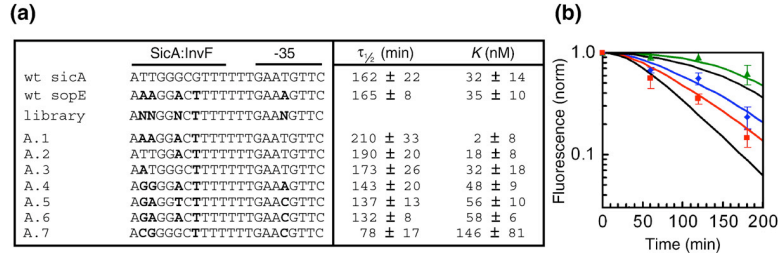


Fig. 9. Mutations to the SicA:InvF-binding site in the internal promoter vary the strength of the positive feedback loop, resulting in different relaxation times. (a) The -50 to -30 region of the *sicA* promoter, which includes the previously identified SicA:InvF-binding site, is shown.¹⁶ For each sequence, the resulting empirical half-life ($\tau_{1/2}$) is shown in addition to the binding constant (K) derived from fitting the mutant data to the model. Error bars are reported as the standard deviation of six experiments performed on different days. When the binding site from the *sicA* promoter is mutated to the *sopE* site, there is no change in the observed half-life. A small library, where the differences between the *sicA* and *sopE* operators were randomly mutated (library), was then created. The resulting mutants have a significant diversity of decay times (A.1–A.7). (b) The decay data are shown for three representative mutants. The wild-type *sicA* promoter (top black line) and the PBAD30.*sicA* (lower black line) data are shown as reference (Fig. 7). The mutant with the longest decay time (A.1, red triangles) and two mutants with the fastest decay times (A.6, blue diamonds; A.7, red squares) are shown. Error bars represent the standard deviation of six experiments performed on different days.

a large variety of delay times could be obtained from such a small mutant library.

Discussion

Pathogens interact with their hosts through the timed release of multiple protein and chemical effectors. This timing has to be carefully controlled to reflect the specific requirements of particular microenvironments encountered during an infection. Complex molecular machines, such as the T3SS, also require regulation to coordinate their self-assembly and function. Here, we have experimentally characterized the induction and relaxation dynamics of the regulatory network controlling the *S. typhimurium* T3SS encoded within SPI-1. This network contains a series of integrated genetic circuits that control the temporal and stochastic properties of gene expression when the secretion system is induced. In addition, a split positive feedback loop is shown to affect the relaxation dynamics, where effector expression persists after cells are shifted into noninducing conditions.

Upon induction, the SPI-1 promoters are activated in a manner that is consistent with the self-assembly of the needle. The overall dynamics are very similar to that observed for flagella,³⁵ despite significant divergence with the SPI-1 operon structure and regulatory interactions. In addition, when induced, only a fraction of bacteria turn on the SPI-1 genes.^{5,10,30} Single-cell experiments are critical for characterizing the dynamics of networks that are only active in a subset of the population.⁶³

Other *Salmonella* genes have been shown to be induced within a subpopulation. For example, intracellular bacteria differ in their induction of

SPI-2 and other virulence genes.^{17,19,30} Stochastic gene expression may lead to different physiological roles; for example, individuals within a single host cell have been observed to bifurcate into a static or a rapid growth state.¹ Population heterogeneity has been observed for other intracellular pathogens, such as the presence of both static and motile *Mycobacterium* phenotypes within a single host cell.⁶² The stochastic control of virulence genes enables individuals in a population to probabilistically vary their physiological behavior at each stage of an infection.⁷⁰

Within the SPI-1 regulatory network, there is a genetic circuit that links the expression of effectors with the secretion state of the cell.¹⁶ A unique aspect of this circuit is that the positive feedback loop is split (Fig. 6, Topology 1). One can imagine two alternate network topologies. Each topology can be secretion-inducible, but they differ in the way the network relaxes. First, both the chaperone and the transcription factor could be encoded upstream of the internal promoter (Fig. 6, Topology 2). This would produce a cascade, as is often found in regulatory networks.⁶⁰ This topology produces a significantly shorter relaxation delay, and it is difficult to increase the delay by changing the model parameters. This topology is roughly simulated when the *sicA* gene is placed under inducible control, in which case the network is similarly induced, but the delay is almost eliminated (Fig. 7).

The SicA:InvF circuit, including the split feedback loop, is conserved in *Yersinia enterocolitica* (YsaE, SycB, and YspC are homologous to InvF, SicA, and SipC).⁶⁹ Interestingly, *Shigella flexneri* also has homologues to these proteins (MxiE, IpgC, and IpaC); however, the genomic organization and the

resulting genetic circuit differ considerably.⁴⁵ In this circuit, the IpgC:MxiE complexes activate outside promoters controlling effector expression, but they do not upregulate their own production.²⁷ Therefore, there is no positive feedback loop, and the circuit resembles a simple cascade (Topology 2). It will be interesting to compare the induction and relaxation dynamics of the *Salmonella* circuit with those encoded in *Yersinia* and *Shigella*.

A third topology, where both the transcription factor and the chaperone are downstream of the internal promoter, is also possible (Fig. 6, Topology 3). This forms a complete positive feedback loop, where all of the required genes are internal to the loop. If there is higher-order cooperativity in the nonlinear term, this topology can produce a bistable switch, which is difficult to deactivate once it is turned on.^{5,53,71} A similar topology is present in the regulatory network controlling the expression of flagella.¹¹ Within the network, a genetic circuit controls the expression of flagellin, which forms the filament. After the basal body is constructed, the sigma factor FliA (analogous to *X*) activates its own expression and an anti-sigma factor FlgM (analogous to *Y*), which is secreted. After the filament is constructed, FlgM accumulates in the cytoplasm and deactivates the positive feedback loop by binding to FliA. The irreversibility intrinsic to this topology with respect to the input signal enables the circuit to continue the formation of filament until the flagellum is fully constructed once the pathway is initiated. This irreversibility would be disadvantageous in the case of SPI-1 because the effectors are temporally induced to promote invasion, after which their expression needs to be downregulated.

The SicA:InvF split feedback loop and the resulting relaxation delay may have a physiological role in controlling a physiological bifurcation that occurs immediately post-invasion. After invading a macrophage, *Salmonella* either persists and grows in the intracellular environment or rapidly induces apoptosis within an hour.^{43,46} Rapid apoptosis is dependent on the SipB effector (transcribed from the *sicA* promoter) and caspase-1.^{31,46} Transcription from the *sicA* promoter has been shown to persist during the first hours after invasion.⁸ The inability to turn off SipB expression post-invasion (via a Δlon mutant) has been shown to increase the probability of apoptosis.^{65,66} The length of effector expression post-invasion could alter the ratio of persistent cells to apoptotic cells, and, ultimately, the speed of pathogenesis.²⁹ The SicA:InvF operator in the *sicA* promoter could act as an evolutionary tuning knob by which the probability of inducing apoptosis could be controlled. This hypothesis could be tested by perturbing the strength of the feedback loop and by measuring the fraction of infected macrophages that enter an apoptotic state.

The combination of theory with experiments provides a quantitative platform for understanding the dynamics of regulatory networks. These tools enable more refined methods to interrogate networks by perturbing their underlying biochemical

mechanisms. Here, this approach is applied to the regulatory network controlling SPI-1 in two ways. First, we were able to rewire the network to convert a split positive feedback loop into a cascade. Second, mutations were made to a transcription-binding site. In both cases, the model was used both to predict the effect of making these genetic changes and then to quantitatively frame the resulting change in dynamics. This represents a powerful approach to perturbing and understanding how sets of biochemical interactions lead to the observed complex global dynamics.

Materials and Methods

Plasmids and strains

The reporter plasmids were constructed based on the pPROTet Cm^r system (ColE1 ori) available from Clontech/BD. The SPI-1 promoters were cloned from *S. enterica* Typhimurium SL1344 genomic DNA, transcriptionally fused with *gfp* (*gfpmut3*) using SOEing PCR, and ligated into pPRO using the XhoI/XbaI restriction sites. A large upstream region associated with each promoter was cloned: *hilD* (−312), *hilC* (−432), *prgH* (−317), and *sicA* (−166). The *hilC* region contains two promoters in series. The 5' untranslated region was included in the start codon of each respective gene. SVM687, a *sicAaphT* mutant of SL1344, was used for all complementation experiments.¹⁵ A plasmid encoding *psicA:sicA* was cloned from SL1344 genomic DNA and ligated into PBAD30 using a XhoI site introduced upstream of the P_{BAD} promoter together with the XbaI site in the multiple cloning site. An inducible *sicA* construct was made by cloning the *sicA* gene with an optimized rbs (TCACACAGGAAAAG)[‡] from SL1344 genomic DNA and by ligating into the KpnI and XbaI sites of PBAD30.

Salmonella growth curves

All optical densities were measured using a Cary 50 Bio spectrophotometer. Bacteria transformed with a reporter plasmid were grown overnight (~13 h) in 5 ml of L-broth (Difco, Lennox, CA) supplemented with 34.4 µg/ml chloramphenicol (Cm). The overnight cultures were then diluted 1:500 into 5 ml of fresh L-broth and grown for 150 min at 37 °C to OD₆₀₀ ~ 0.15. A 2-ml aliquot was then added to 50 ml of inducing media (7 g/L NaCl added to Difco LB broth, Miller) in a nonbaffled 250-ml flask. The cultures were grown in a shaker at 37 °C at 160 rpm. During growth, 500-µl aliquots were taken every 30 min, OD₆₀₀ was measured, and the cells were spun down, resuspended in 200 µl of phosphate-buffered saline with 2 mg/ml kanamycin, and put on ice to stop *gfp* expression. For the dilution experiments, cells were grown to maximum induction of SPI-1 (OD₆₀₀ ~ 2.05). A 500-µl aliquot was then taken, spun down, washed with fresh L-broth, and then diluted 1:100 into 50 ml of fresh L-broth containing Cm. Aliquots were taken every 30 min, and the sample was spun down and resuspended in phosphate-buffered saline as before.

[‡] BBa_B0032 from parts.mit.edu

Test for plasmid loss

To test for potential plasmid loss effects, 500- μ l samples were taken from the last time point after the shift to noninducing conditions. The samples were serially diluted 1:10⁶, 20 μ l of which was spread on a plate with no antibiotics and on one containing Cm. The plates were grown overnight, and colonies were counted. The *sicA* promoter reporter produced 16 \pm 5 colonies on the plate lacking antibiotics and 14 \pm 5 colonies on the plate with Cm. The *hilC* promoter produced 25 \pm 9 colonies on the plate lacking antibiotics and 24 \pm 8 on the plate with Cm. The data represent eight replicates on different days. This demonstrates that the delay is not due to a change in plasmid stability.

Complementation assays

Cultures were handled as described in the reporter assay with the following exceptions. Binary plasmid systems were grown in media supplemented with 34.4 μ g/ml Cm and 100 μ g/ml ampicillin. Overnight cultures were diluted 1:100 into fresh L-broth. After 150 min, a 3-ml aliquot was added to 30 ml of inducing media. Cultures were induced after 150 min with 60 μ l of 100 mg/ml arabinose, leading to a final concentration of 1.33 mM arabinose. During growth, 600- μ l aliquots were taken hourly. Three hours post-arabinose induction, a 600- μ l aliquot was taken, spun down, washed with fresh L-broth, and diluted 1:50 into 30 ml of fresh L-broth containing appropriate antibiotics. Postdilution aliquots were taken hourly.

SicA promoter library construction

A small library was constructed of the SicA:InvF-binding site in the *sicA* promoter. In addition to this library, the SicA:InvF-binding site in the *sicA* promoter was changed to the one from the *sopE* promoter. The *psopE*-binding site mutant and the library of *psicA*-binding sites were constructed using the phosphorylated primers aaGgAcTHTTTTGAaGTTCACTAACCACCGTCCGGGGTTAATAACTGC (for the *psopE* site) and nnGGnCHTTTTTGAAnGTTCACTAACCACCGTCCGGGGTTAATAACTGC (for the library) and a reverse primer TGAATACATCGCTACTGCCTTACGCGGCTC. Mutagenesis was carried out in accordance with the Finnzyme's Phusion Site-Directed Mutagenesis protocol, with no alterations. The primers were used to amplify the *psicA*:*sicA* plasmid using Hot Start Phusion DNA polymerase, and each resulting PCR product was ligated and transformed into *E. coli* strain DH10B and plated on ampicillin-selective plates. Sequencing confirmed that the InvF-binding site of *psicA* was replaced with that of *psopE*. Seven colonies from the library plate were chosen, and sequencing revealed that each plasmid had a unique SicA:InvF-binding site of *psicA*. These seven plasmids were cotransformed with the *psicA*:GFP plasmid into Δ *sicA* strain SVM687.

Flow cytometry

Flow cytometry data were obtained with a BD FACSCalibur system as part of the University of California-San Francisco core facility. Each bacterial data set consists of at least 30,000 cells. The data were

gated by forward scatter and side scatter to observe bacteria-sized particles. Data analysis was performed using the programs WINMDI and FlowJo.

Solution of model equations

Numerical solutions were obtained for the system of ODEs (Eqs. (1)–(3)) using MATLAB. The solution to these differential equations also depends on three algebraic equations for the total number of molecules (X_T , Y_T , and Z_T), as well as on two algebraic equations that describe the equilibrium relationships for the formation of dimers. First, a physically relevant analytic solution is obtained for the sixth-order polynomial that results from the algebraic equations. Then, the nonlinear ODEs are numerically solved using a multistep stiff solver (ode15s). The simulations were started without secretion ($k_c=0$) and then shifted to $k_c=0.1$ at time T_1 . During this time, the external promoter was activated ($k_0=1.0$). At T_2 , the external promoter was turned off ($k_0=0$), and the relaxation dynamics were recorded. The times T_1 and T_2 are selected so that the system has reached steady state prior to each event.

To model the expression of *gfp* from the *sicA* promoter reporter, an additional differential equation was added to the model: $\frac{dg}{dt} = a_g \left(\frac{C_{XY}}{K + C_{XY}} \right) - \gamma_g g$, where a_g and γ_g are the expression and degradation rates of *gfp*, respectively. The degradation rate was set to 0.022 to reflect degradation due to cell division. All of the fluorescence data were fitted in normalized form, so the expression rate was arbitrarily set to 1.0. The model with this equation was solved in the same manner as described above.

Parameter fitting

The parameters were either fixed to estimated values using data from the literature or fitted using the experimental data presented in this article (Table 1). The parameters that were fitted were determined by identifying values that minimize the collective L_1 distance between the normalized experimental and model data sets, or $\chi = \frac{1}{N} \sum_{i=1}^N |GFP_{exp}^{norm}(t_i) - GFP_{model}^{norm}(t_i)|$, taken at time points t_i and for each data set, including time series data from both P30.*psicA*:*sicA* and PBAD30.*sicA* data (Fig. 7). The dynamics of the GFP fluorescence are normalized by dividing them by its initial value at time T_2 (for the model) and $t=0$ h (for the experiment time series). A combination of manual fitting and automated simulated annealing resulted in a parameter set that fitted the P30.*psicA*:*sicA* and PBAD30.*sicA* experimental data with L_1 distances of 0.0186 and 0.0181, respectively. Using a similar procedure, the affinity of the InvF:SicA complex for each mutant promoter (Fig. 9a) was determined by identifying the affinity (K) that minimized the L_1 distance between the respective mutant time series data and the resulting model solution, while keeping all other parameters of the model constrained. For fitting the mutant data, only the K for *sicA* expression was varied because the mutants are on a plasmid and only affect that gene (*SipC* expression uses the data fit for the wild type). Using the standard deviations of the experimental time series data as upper and lower bounds, the standard deviations of the affinities for each mutant promoter

were also determined in accordance with the same fitting procedure.

Acknowledgements

C.A.V. was supported by Pew and Packard Foundations, NIH EY016546, NIH AI067699, NSF BES-0547637, and a Sandler Family Opportunity Award. C.A.V., H.S., and K.T. are part of the NSF SynBERC ERC (www.synberc.org). K.T. and A.L. are supported by an NSF Graduate Research Fellowship.

References

- Abshire, K. Z. & Neidhardt, F. C. (1993). Growth rate paradox of *Salmonella typhimurium* within host macrophages. *J. Bacteriol.* **175**, 3744–3748.
- Akbar, S., Schechter, L. M., Lostroh, C. P. & Lee, C. A. (2003). Ara/XylS family members, HilD and HilC, directly activate virulence gene expression independently of HilA in *Salmonella typhimurium*. *Mol. Microbiol.* **47**, 715–728.
- Alon, U. (2006). *An Introduction to Systems Biology: Design Principles of Biological Networks*. CRC Press, London, UK.
- Bajaj, V., Lucas, R. L., Hwang, C. & Lee, C. A. (1996). Co-ordinate regulation of *Salmonella typhimurium* invasion genes by environmental and regulatory factors is mediated by control of *hilA* expression. *Mol. Microbiol.* **22**, 703–714.
- Becskei, A., Seraphin, B. & Serrano, L. (2001). Positive feedback in eukaryotic gene networks: cell differentiation by graded to binary response conversion. *EMBO J.* **20**, 2528–2535.
- Biggar, S. R. & Crabtree, G. R. (2001). Cell signaling can direct either binary or graded transcriptional responses. *EMBO J.* **20**, 3167–3176.
- Birket, S. E., Harrington, A. T., Espina, M., Smith, N. D., Terry, C. M., Darboe, N. *et al.* (2007). Preparation and characterization of translocator/chaperone complexes and their component proteins from *Shigella flexneri*. *Biochemistry*, **46**, 8128–8137.
- Boddicker, J. D. & Jones, B. D. (2004). Lon protease activity causes down regulation of *Salmonella* pathogenicity island 1 invasion gene expression after infection of epithelial cells. *Infect. Immun.* **72**, 2002–2013.
- Boddicker, J. D., Knosp, B. M. & Jones, B. R. (2003). Transcription of the *Salmonella* invasion gene activator, *hilA*, requires HilD activation in the absence of negative regulators. *J. Bacteriol.* **185**, 525–533.
- Bumann, D. (2002). Examination of *Salmonella* gene expression in an infected mammalian host using green fluorescent protein and two-color flow cytometry. *Mol. Microbiol.* **43**, 1269–1283.
- Chilcott, G. S. & Hughes, K. T. (2000). Coupling of flagellar gene expression to flagellar assembly in *Salmonella enterica* serovar Typhimurium and *Escherichia coli*. *Microbiol. Mol. Biol. Rev.* **64**, 694–708.
- Clark, M. A., Jepson, M. A., Simmons, N. L. & Hirst, B. M. (1994). Preferential interaction of *Salmonella typhimurium* with mouse Peyer's patch M cells. *Res. Microbiol.* **145**, 543–552.
- Cornelis, G. R. (2006). The type III secretion injectosome. *Nat. Rev.* **4**, 811–825.
- Darwin, K. H. & Miller, V. L. (1999). InvF is required for expression of genes encoding proteins secreted by the SPI-1 type III secretion apparatus in *Salmonella typhimurium*. *J. Bacteriol.* **181**, 4949–4954.
- Darwin, K. H. & Miller, V. L. (2000). The putative invasion protein chaperone SicA acts together with InvF to activate the expression of *Salmonella typhimurium* virulence genes. *Mol. Microbiol.* **35**, 949–960.
- Darwin, K. H. & Miller, V. L. (2001). Type III secretion chaperone-dependent regulation: activation of virulence genes by SicA and InvF in *Salmonella typhimurium*. *EMBO J.* **20**, 1850–1862.
- Drecktrah, D., Knodler, L. A., Ireland, R. & Steele-Mortimer, O. (2006). The mechanism of *Salmonella* entry determines the vacuolar environment and intracellular gene expression. *Traffic*, **7**, 39–51.
- de Keersmaecker, S. C. J., Marchal, K., Verhoeven, T. L. A., Engelen, K., Vanderleyden, J. & Detweiler, C. S. (2005). Microarray analysis and motif detection reveal new targets of the *Salmonella enterica* serovar Typhimurium HilA regulatory protein, including *hilA* itself. *J. Bacteriol.* **187**, 4381–4391.
- Detweiler, C. S., Monack, D. M., Brodsky, I. E., Mathew, H. & Falkow, S. (2003). *virK*, *sonA* and *rcsC* are important for systemic *Salmonella enterica* serovar Typhimurium infection and cationic peptide resistance. *Mol. Microbiol.* **48**, 385–400.
- Eichelberg, K. & Galan, J. E. (1999). Differential regulation of *Salmonella typhimurium* type III secreted proteins by pathogenicity island 1 (SPI-1)-encoded transcriptional activators InvF and HilA. *Infect. Immun.* **67**, 4099–4105.
- Ellermeier, J. R. & Schlauch, J. M. (2007). Adaption to the host environment: regulation of the SPI1 type III secretion system in *Salmonella enterica* serovar Typhimurium. *Curr. Opin. Microbiol.* **10**, 24–29.
- Ellermeier, C. D., Ellermeier, J. R. & Schlauch, J. M. (2005). HilD, HilC, and RtsA constitute a feed forward loop that controls the expression of the SPI-1 type III secretion system regulator *hilA* in *Salmonella enterica* serovar Typhimurium. *Mol. Microbiol.* **57**, 691–705.
- Enninga, J., Mounier, J., Sansonetti, P. & Nhieu, G. T. V. (2005). Secretion of type III effectors into host cells in real time. *Nat. Methods*, **2**, 959–965.
- Eriksson, S., Lucchini, S., Thompson, A., Rhen, M. & Hinton, J. C. D. (2003). Unravelling the biology of macrophage infection by gene expression profiling of intracellular *Salmonella enterica*. *Mol. Microbiol.* **47**, 103–118.
- Galan, J. E. & Collmer, A. (1999). Type III secretion machines: bacterial devices for protein delivery into host cells. *Science*, **284**, 1322–1328.
- Galan, J. E. & Zhou, D. (2000). Striking a balance: modulation of the actin cytoskeleton by *Salmonella*. *Proc. Natl Acad. Sci. USA*, **97**, 8754–8761.
- Gall, T. L., Marvis, M., Martino, M. C., Bernardini, M. L., Denamur, E. & Parsot, C. (2005). Analysis of virulence plasmid gene expression defines three classes of effectors in the type III secretion system of *Shigella flexneri*. *Microbiology*, **151**, 951–962.
- Groisman, E. A. & Ochman, H. (1996). Pathogenicity islands: bacterial evolution in quantum leaps. *Cell*, **87**, 791–794.
- Guiney, D. G. (2005). The role of host cell death in *Salmonella* infections. *Curr. Top. Microbiol.* **289**, 131–150.
- Hautefort, I., Proenca, M. J. & Hinton, J. C. D. (2003). Single-copy green fluorescent protein gene fusions

- allow accurate measurement of *Salmonella* gene expression *in vitro* during infection of mammalian cells. *Appl. Environ. Microbiol.* **69**, 7480–7491.
31. Hersh, D., Monack, D. M., Smith, M. R., Ghori, N., Falkow, S. & Zychlinsky, A. (1999). The *Salmonella* invasion SipB induces macrophage apoptosis by binding to caspase-1. *Proc. Natl Acad. Sci. USA*, **96**, 2396–2401.
 32. Hooshangi, S., Thiberge, S. & Weiss, R. (2005). Ultra-sensitivity and noise propagation in a synthetic transcriptional cascade. *Proc. Natl Acad. Sci. USA*, **102**, 3581–3586.
 33. Jones, B. D., Ghori, N. & Falkow, S. (1994). *Salmonella typhimurium* initiates murine infection by penetrating and destroying the specialized epithelial M cells of Peyer's patches. *J. Exp. Med.* **180**, 15–23.
 34. Kalir, S., Mangan, S. & Alon, U. (2005). A coherent feed-forward loop with a SUM input function prolongs flagella expression in *Escherichia coli*. *Mol. Syst. Biol.* **1**, E1–E6.
 35. Kalir, S., McClure, J., Pabbaraju, K., Southward, C., Ronen, M., Leibler, S. *et al.* (2001). Ordering genes in a flagella pathway by analysis of expression kinetics from living bacteria. *Science*, **292**, 2080–2083.
 36. Kubori, T., Matsushima, Y., Nakamura, D., Uralil, J., Lara-Tejero, M., Sukhan, A. *et al.* (1998). Supramolecular structure of the *Salmonella typhimurium* type III protein secretion system. *Science*, **280**, 602–605.
 37. Laub, M. T., McAdams, H. H., Feldblum, T., Fraser, C. M. & Shapiro, L. (2000). Global analysis of the genetic network controlling a bacterial cell cycle. *Science*, **290**, 2144–2148.
 38. Lee, C. A. & Falkow, S. (1990). The ability of *Salmonella* to enter mammalian cells is affected by bacterial growth state. *Proc. Natl Acad. Sci. USA*, **87**, 4304–4308.
 39. Lostroh, C. P. & Lee, C. A. (2001). The HilA box and sequences outside it determine the magnitude of HilA-dependent activation of PprgH from *Salmonella* pathogenicity island 1. *J. Bacteriol.* **183**, 4876–4885.
 40. Lostroh, C. P., Bajaj, V. & Lee, C. A. (2000). The *cis* requirements for transcriptional activation by HilA, a virulence determinant encoded on SPI-1. *Mol. Microbiol.* **37**, 300–315.
 41. Lucas, R. L. & Lee, C. A. (2000). Unraveling the mysteries of virulence gene regulation in *Salmonella typhimurium*. *Mol. Microbiol.* **36**, 1024–1033.
 42. Lucas, R. L. & Lee, C. A. (2001). Roles of *hilC* and *hilD* in regulation of *hilA* expression in *Salmonella enterica* serovar Typhimurium. *J. Bacteriol.* **183**, 2733–2745.
 43. Lundberg, U., Vinatzer, U., Berdik, D., von Gabain, A. & Baccarini, M. (1999). Growth phase-regulated induction of *Salmonella*-induced macrophage apoptosis correlates with transient expression of SPI-1 genes. *J. Bacteriol.* **181**, 3433–3437.
 44. Mangan, S., Zaslaver, A. & Alon, U. (2003). The coherent feedforward loop serves as a sign-sensitive delay element in transcription networks. *J. Mol. Biol.* **334**, 197–204.
 45. Marvis, M., Page, A.-L., Tournebise, R., Demers, B., Sansonetti, P. & Parsot, C. (2002). Regulation of transcription by the activity of the *Shigella flexneri* type III secretion apparatus. *Mol. Microbiol.* **43**, 1543–1553.
 46. Monack, D. M., Detweiler, C. S. & Falkow, S. (2001). *Salmonella* pathogenicity island 2-dependent macrophage cell death is mediated in part by the host cysteine protease caspase-1. *Cell. Microbiol.* **3**, 825–837.
 47. Marlovits, T. C., Kubori, T., Sukhan, A., Thomas, D. R., Galan, J. E. & Unger, V. M. (2004). Structural insights into the assembly of the type III secretion needle complex. *Science*, **306**, 1040–1042.
 48. Matsui, H., Bacot, C. M., Garlington, W. A., Doyle, T. J., Roberts, S. & Gulig, P. A. (2001). Virulence plasmid-borne *spvB* and *spvC* genes can replace the 90-kilobase plasmid in conferring virulence to *Salmonella enterica* serovar Typhimurium in subcutaneously inoculated mice. *J. Bacteriol.* **183**, 4652–4658.
 49. Menard, R., Sansonetti, P., Parsot, C. & Vasselon, T. (1994). Extracellular association and cytoplasmic partitioning of the IpaB and IpaC invasins of *S. flexneri*. *Cell*, **79**, 515–525.
 50. Novick, A. & Weiner, M. (1957). Enzyme induction is an all-or-none phenomenon. *Proc. Natl Acad. Sci. USA*, **47**, 553–567.
 51. Olekhovich, I. N. & Kadner, R. J. (2002). DNA-binding activities of the HilC and HilD virulence regulatory proteins of *Salmonella enterica* serovar Typhimurium. *J. Bacteriol.* **184**, 4148–4160.
 52. Osiecki, J. C., Barker, J., Picking, W. L., Serfis, A. B., Berring, E., Shah, S. *et al.* (2001). IpaC from *Shigella* and SipC from *Salmonella* possess similar biochemical properties but are functionally distinct. *Mol. Microbiol.* **42**, 469–481.
 53. Ozbudak, E. M., Thattai, M., Lim, H. N., Shraiman, B. I. & van Oudenaarden, A. (2004). Multistability in the lactose utilization network of *Escherichia coli*. *Nature*, **427**, 737–740.
 54. Pedraza, J. M. & van Oudenaarden, A. (2005). Noise propagation in gene networks. *Science*, **307**, 1965–1969.
 55. Rosenfeld, N., Young, J. W., Alon, U., Swain, P. S. & Elowitz, M. B. (2005). Gene regulation at the single-cell level. *Science*, **307**, 1962–1965.
 56. Rossi, F. M. V., Kringstein, A. M., Spicher, A., Guicherit, O. M. & Blau, H. M. (2000). Transcriptional control: rheostat converted to on/off switch. *Mol. Cell*, **6**, 723–728.
 57. Schechter, L. M. & Lee, C. A. (2001). AraC/XylS family members, HilC and HilD, directly bind and derepress the *Salmonella typhimurium* *hilA* promoter. *Mol. Microbiol.* **40**, 1289–1299.
 58. Schechter, L. M., Jain, S., Akbar, S. & Lee, C. A. (2003). The small nucleoid-binding proteins H-NS, HU, and Fis affect *hilA* expression in *Salmonella enterica* serovar Typhimurium. *Infect. Immun.* **71**, 5432–5435.
 59. Schlumberger, M. C., Muller, A. J., Ehrbar, K., Winnen, B., Duss, I., Stecher, B. & Hardt, W. D. (2005). Real-time imaging of type III secretion: *Salmonella* SipA injection into host cells. *Proc. Natl Acad. Sci. USA*, **102**, 12548–12553.
 60. Shen-Orr, S. S., Milo, R., Mangan, S. & Alon, U. (2002). Network motifs in the transcriptional regulation network of *Escherichia coli*. *Nat. Genet.* **31**, 64–68.
 61. Spudich, J. L. & Koshland, D. E., Jr (1976). Non-genetic individuality: chance in the single cell. *Nature*, **262**, 467–471.
 62. Stamm, L. M., Morisaki, J. H., Gao, L. Y., Jeng, R. L., McDonald, K. L., Roth, R. *et al.* (2003). *Mycobacterium marinum* escapes from phagosomes and is propelled by actin-based motility. *J. Exp. Med.* **198**, 1361–1368.
 63. Suel, G. M., Garcia-Ojalvo, J., Liberman, L. M. & Elowitz, M. B. (2006). An excitable gene regulatory circuit induces transient cellular differentiation. *Nature*, **440**, 545–550.
 64. Sukhan, A., Kubori, T., Wilson, J. & Galan, J. E. (2001). Genetic analysis of assembly of the *Salmonella enterica* serovar Typhimurium type III secretion-associated needle complex. *J. Bacteriol.* **183**, 1159–1167.

65. Takaya, A., Suzuki, A., Kikuchi, Y., Eguchi, M., Isogai, E., Tomoyasu, T. & Yamamoto, T. (2005). Derepression of *Salmonella* pathogenicity island 1 genes within macrophages leads to rapid apoptosis via caspase-1- and caspase-3-dependent pathways. *Cell. Microbiol.* **7**, 79–90.
66. Takaya, A., Kubota, Y., Isogai, E. & Yamamoto, T. (2005). Degradation of the HilC and HilD regulator proteins by ATP-dependent Lon protease leads to downregulation of *Salmonella* pathogenicity island 1 gene expression. *Mol. Microbiol.* **55**, 839–852.
67. Tucker, S. C. & Galan, J. E. (2000). Complex function for SicA, a *Salmonella enterica* serovar Typhimurium type III secretion-associated chaperone. *J. Bacteriol.* **182**, 2262–2268.
68. Voigt, C. A., Wolf, D. M. & Arkin, A. P. (2005). The *Bacillus subtilis* *sin* operon: an evolvable network motif. *Genetics*, **169**, 1187–1202.
69. Walker, K. A. & Miller, V. L. (2004). Regulation of the Ysa type III secretion system of *Yersinia enterocolitica* by YsaE/SycB and YsrS/YsrR. *J. Bacteriol.* **186**, 4056–4066.
70. Wolf, D. M. & Arkin, A. P. (2003). Motifs, modules, and games in bacteria. *Curr. Opin. Microbiol.* **6**, 125–134.
71. Xiong, W. & Ferrell, J. E., Jr (2003). A positive-feedback-based bistable 'memory module' that governs a cell fate decision. *Nature*, **426**, 460–465.

A Synthetic Genetic Edge Detection Program

Jeffrey J. Tabor,¹ Howard M. Salis,¹ Zachary Booth Simpson,^{2,3} Aaron A. Chevalier,^{2,3} Anselm Levskaya,¹ Edward M. Marcotte,^{2,3,4} Christopher A. Voigt,^{1,*} and Andrew D. Ellington^{2,3,4}

¹Department of Pharmaceutical Chemistry, School of Pharmacy, University of California San Francisco, San Francisco, CA 94158, USA

²Center for Systems and Synthetic Biology

³Institute for Cellular and Molecular Biology

⁴Department of Chemistry and Biochemistry

University of Texas, Austin, TX 78712, USA

*Correspondence: cavoigt@picasso.ucsf.edu

DOI 10.1016/j.cell.2009.04.048

SUMMARY

Edge detection is a signal processing algorithm common in artificial intelligence and image recognition programs. We have constructed a genetically encoded edge detection algorithm that programs an isogenic community of *E. coli* to sense an image of light, communicate to identify the light-dark edges, and visually present the result of the computation. The algorithm is implemented using multiple genetic circuits. An engineered light sensor enables cells to distinguish between light and dark regions. In the dark, cells produce a diffusible chemical signal that diffuses into light regions. Genetic logic gates are used so that only cells that sense light and the diffusible signal produce a positive output. A mathematical model constructed from first principles and parameterized with experimental measurements of the component circuits predicts the performance of the complete program. Quantitatively accurate models will facilitate the engineering of more complex biological behaviors and inform bottom-up studies of natural genetic regulatory networks.

INTRODUCTION

Living cells can be programmed with genetic parts, such as promoters, transcription factors and metabolic genes (Andriantoandro et al., 2006; Benner and Sismour, 2005; Canton et al., 2008; Endy, 2005; Haseltine and Arnold, 2007). These parts can be combined to construct genetic versions of electronic circuits, including switches (Atkinson et al., 2003; Gardner et al., 2000; Kramer and Fussenegger, 2005; Kramer et al., 2004), logic (Anderson et al., 2007; Guet et al., 2002; Rackham and Chin, 2005), memory (Ajo-Franklin et al., 2007; Gardner et al., 2000; Ham et al., 2006), pulse generators (Basu et al., 2004), and oscillators (Atkinson et al., 2003; Elowitz and Leibler, 2000; Fung et al., 2005; Stricker et al., 2008; Tiggles et al., 2009). The current challenge is to assemble multiple genetic circuits into larger programs for the engineering of more sophisticated behaviors (Purnick and Weiss, 2009).

The characterization of transfer functions or the quantitative relationship between circuit input(s) and output(s) (Bintu et al.,

2005a; Tabor et al., 2009; Voigt, 2006; Weiss et al., 1999) will aid the development of accurate mathematical models (Ajo-Franklin et al., 2007; Guido et al., 2006) which will allow complex genetic programs to be examined in silico prior to physical construction. Predictive models for the design of genetic programs will drive applications in biotechnology and aid bottom-up studies of natural regulatory systems.

Edge detection is a well-studied computational problem used to determine the boundaries of objects within an image (Suel et al., 2000). This process reduces the information content in a complex image and is used in applications ranging from retinal preprocessing (Maturana and Frenk, 1963) to the analysis of microarray data (Kim et al., 2001). For a digital black and white image, a typical algorithm operates by scanning for a white pixel and then comparing the intensity of that pixel to its eight neighboring pixels. If any of the neighbors is black, the algorithm classifies those pixels as being part of an edge. The serial nature of this search process results in a computation time that increases linearly with the number of pixels in the image. We aimed to implement a parallel edge detection algorithm wherein each bacterium within a spatially distributed population functions as an independent signal processor. In this design, each bacterium (up to 10^9 individuals for a 90 mm Petri dish image) processes a small amount of local information simultaneously, and the population cooperates to find the edges.

RESULTS

A Genetic Program for Edge Detection

The genetic edge detection algorithm programs a lawn of bacteria to identify the light-dark boundaries within a projected image of light (Figures 1A and 1B). To accomplish this, each bacterium in the population executes the following pseudocode (Figure 1C): IF NOT light, produce signal. IF signal AND NOT (NOT light), produce pigment.

The “produce signal” and “produce pigment” functions make the cell generate a diffusible communication signal and a black pigment, respectively. The conversion of this pseudocode into a molecular genetic system is shown in Figure 1D.

When cells sense that they are in the dark, they produce the diffusible signal (Figure 1B). Cells that sense light do not make the signal, but are allowed to respond to it. Thus only those cells that are in the light but proximal to dark areas activate the output which results in the enzymatic production of a black pigment. The biological edge detection algorithm requires: (1) a dark

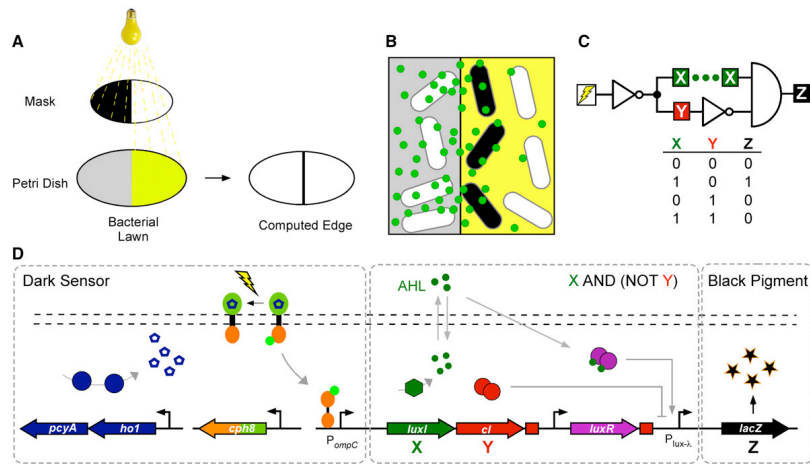


Figure 1. Bacterial Edge Detection

(A) Light is projected through a mask onto a large community (lawn) of bacteria grown on a Petri dish. The lawn computes the edges, or boundaries between light and dark regions, and visually presents the output.

(B) To find the edges, bacteria in the dark produce a communication signal (green circles) that diffuses across the dark/light boundary. Bacteria in the dark cannot respond to the communication signal. Only bacteria that are exposed to light and receive the signal become positive for the expression of a visible reporter gene. The sum of this activity over the entire two-dimensional population is equivalent to the edges of the input image.

(C) (Top) A NOT light gate (lightning box + adjacent triangle) drives a cell-cell communication circuit (green X) and an inverter (red Y + adjacent triangle). These two signals combine as inputs for a downstream AND gate (semi-circle) which drives the final output (Z). Because signal is inverted at Y, the gate driving Z can also be described as an X AND (NOT Y) gate, and it is referred to as such throughout this work. (Bottom) Z is produced in only one of four possible combinations of X and Y (presence of X, absence of Y).

(D) Conversion of the edge detection algorithm into a molecular genetic system. (Left) The light-sensitive protein Cph8 is a chimeric sensor kinase bearing the photoreceptor domain of the *Synechocystis* phytochrome Cph1 and the kinase domain of *E. coli* EnvZ (Levskaya et al., 2005). Cph8 requires the covalently associated chromophore phycocyanobilin (PCB, blue pentagons) which is produced from heme by the products of the two constitutively expressed genes *ho1* and *pcyA* (Gambetta and Lagarias, 2001). In the presence of red light, the kinase activity of Cph8 is inhibited, precluding the transfer of a phosphoryl group (light green circle) to the response regulator OmpR (orange dumbbell) and subsequent transcription from the *ompC* promoter (P_{ompC}). The dark sensor therefore functions as a NOT light transcriptional logic gate. (Center) *luxI* and *cl* are expressed polycistronically from the NOT light gate. LuxI is a biosynthetic enzyme from *V. fischeri* that produces the cell-cell communication signal 3-oxohexanoyl-homoserine lactone (AHL). Cl is the transcriptional repressor protein from phage λ . AHL binds to the constitutively expressed transcription factor LuxR to activate expression from the P_{luxX} promoter while Cl dominantly represses it. P_{luxX} therefore functions as an X AND (NOT Y) transcriptional logic gate. (Right) The output of P_{luxX} is *lacZ*, the product of which (β -galactosidase) cleaves a substrate in the media to produce black pigment (Experimental Procedures). The edge detection algorithm is encoded as 10,020 basepairs of DNA, carried on three plasmid backbones (Experimental Procedures).

sensor (NOT light), (2) cell-cell communication, and (3) X AND (NOT Y) genetic logic. Each of these components is constructed as an independent genetic circuit and the behavior is characterized. This data is used to parameterize a mathematical model which in turn is used to analyze the complete system.

Construction and Characterization of Genetic Circuits

In an effort to make photographic bacteria, we previously constructed a dark sensor (Levskaya et al., 2005) based on genetic parts from the blue-green algae *Synechocystis* (Yeh et al., 1997). The sensor consists of a chimeric two-component system and a two gene metabolic pathway to make the chromophore phycocyanobilin (PCB) (Gambetta and Lagarias, 2001). To rewire the two-component system, the osmosensing domain of the *E. coli* protein EnvZ was replaced with the photoreceptor domain

of the *Synechocystis* phytochrome Cph1. This programmed phosphotransfer from EnvZ to OmpR and subsequent transcription from the P_{ompC} to be repressed as a function of red light. The sensor therefore functions as a genetic circuit with NOT light logical behavior. When the dark sensor is connected to the production of β -galactosidase, a plate of bacteria can print an image of light as a pattern of black pigment (Figure 3A).

The transfer function, which characterizes how the output of a circuit varies with input at steady-state, has been shown to be a useful tool for connecting genetic circuits (Anderson et al., 2007; Bintu et al., 2005a; Voigt, 2006; Weiss et al., 1999; Yokobayashi et al., 2002). Here, the transfer function of the dark sensor is determined in response to light in the 650 nm band (Figure 2A). The dark sensor generates maximal transcriptional output at light intensities between 0.000 and 0.002W/m², reaches minimal

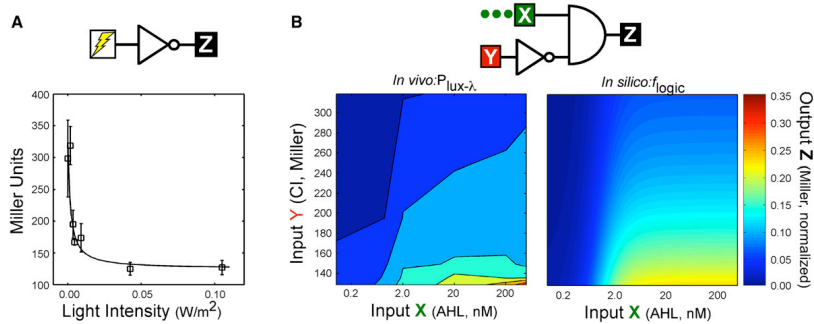


Figure 2. Transfer Functions of the Dark Sensor and X AND (NOT Y) Logic Gate
 (A) The transfer function of the dark sensor is determined in batch culture (Experimental Procedures and Figure S4) and fit to a sigmoidal function (Equation 1). The error bars indicate ± 1 standard deviation. (B) (Left) The transfer function of the X AND (NOT Y) logic gate as determined in batch culture experiments. AHL (X) was added exogenously to the growth media while CI (Y) levels were controlled by varying the intensity of light (Experimental Procedures and Figure S5). The data shown are single replicates of 5 assays taken over 5 separate days where the concentration of CI was altered in each assay. (Right) Mathematical Model. The output of f_{logic} (Equation 2) as a function of AHL and CI. β -galactosidase output levels (Z) for the experiment and the model are normalized by dividing by the output value in the absence of CI with maximum exogenous AHL (Experimental Procedures).

output at $\sim 0.04 \text{ W/m}^2$ and is repressed rapidly and continuously as a function of light (Figure 2A). The transfer function has the form

$$f_{light} = \frac{K}{K + L} (\beta_{max} - \beta_{min}) + \beta_{min} \quad (1)$$

where $\beta_{max} = 298$ and $\beta_{min} = 125$ are the maximum and minimum output values (in Miller units), L is the intensity of light (W/m^2) and the fit parameter is $K = 0.0017 \text{ W/m}^2$ ($R^2 = 0.75$) (Experimental Procedures).

The edge detection algorithm also requires that neighboring bacteria communicate. It has previously been shown that *E. coli* can be programmed to communicate using the quorum sensing system from *V. fischeri* (Anderson et al., 2006; Balagadde et al., 2008; Basu et al., 2005; Weiss and Knight, 2001; You et al., 2004). We placed this communication system under the control of the dark sensor (Figure 3B). In this circuit, dark activates transcription of *luxI*, the product of which catalyzes the formation of the membrane diffusible compound 3-oxohexanoyl-homoserine lactone (AHL) (Engelbrecht and Silverman, 1984). AHL binds to the constitutively expressed transcription factor LuxR to activate expression of β -galactosidase. This produces a pattern of β -galactosidase expression similar to the photographic bacteria, but with an additional blurring component due to AHL diffusion across the dark/light boundary (Figure 3B).

In addition to communication, the edge detection algorithm requires that β -galactosidase be expressed only where AHL AND light, or equivalently NOT (NOT light), are present. This requires genetic circuits that encode the NOT and AND logic functions to be combined with the NOT light circuit. Genetic logic can be constructed by rewiring regulatory interactions (Anderson et al., 2007; Cox et al., 2007; Guet et al., 2002; Mayo et al., 2006; Weiss et al., 1999). The NOT function can be achieved using a genetic inverter, which has previously been shown to invert the activity of an input promoter (Yokobayashi et al., 2002). We con-

structed an inverter using the *cI* gene from phage λ , the product of which forms a dimeric transcriptional repressor that turns OFF the output promoter when the input promoter is ON. By inserting the inverter between the dark sensor input and β -galactosidase output, a negative bacterial photograph can be generated where black pigment is produced only in the light (Figure 3C).

The full logic function AHL AND NOT (NOT light) is implemented at the two-input promoter P_{lux-2} , which is activated by AHL-bound LuxR but dominantly repressed by CI. By adding a constitutively expressed copy of the *luxR* gene to the inverter, the two-dimensional transfer function of this promoter can be determined in batch culture experiments by exogenously varying AHL and light while measuring β -galactosidase activity as the output. Transcription from P_{lux-2} increases proportional to the concentration of AHL between 2 nM and 200 nM. At a given AHL concentration, transcription is repressed approximately 4-fold by maximal (dark) CI levels as compared to those in saturating light (Figure 2B, left). The experimental data is used to fit a two-dimensional transfer function (Figure 2B, right) that uses the Shea-Ackers formalism (Shea and Ackers, 1985) to model transcription factor binding to P_{lux-2} as a function of AHL (u_1) and CI (u_2) concentrations,

$$f_{logic}(u_1, u_2) = \frac{(C_0 + C_1 f_{Lux})}{1 + C_0 + C_1 f_{Lux} + C_2 f_{CI}^n + C_1 C_2 f_{Lux} f_{CI}^n} \quad (2)$$

where f_{Lux} is the concentration of LuxR dimers bound to AHL (Urbanowski et al., 2004) and f_{CI} is the concentration of dimeric CI (Koblan and Ackers, 1991). The parameters c_0 to c_2 are determined by fitting the output of f_{logic} to the transcription measurements ($c_0 = 0.04$, $c_1 = 0.05$, $c_2 = 0.011$, $R^2 = 0.81$) (Experimental Procedures) and n is 1.5. Taken together, the data in Figure 2 demonstrate that the dark sensor and the X AND (NOT Y) logic circuit function as needed for use in the edge detection algorithm. Moreover the transfer functions of the two circuits are

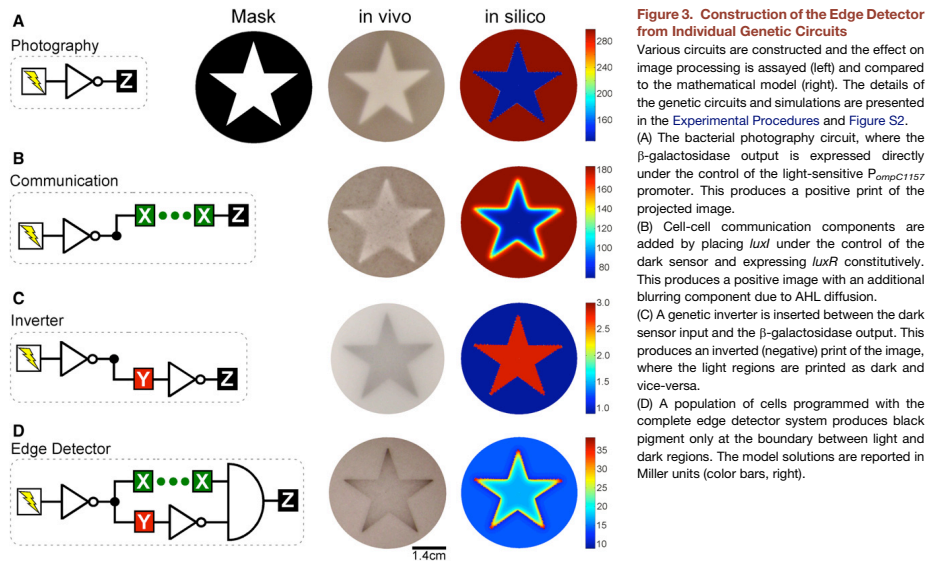


Figure 3. Construction of the Edge Detector from Individual Genetic Circuits

Various circuits are constructed and the effect on image processing is assayed (left) and compared to the mathematical model (right). The details of the genetic circuits and simulations are presented in the [Experimental Procedures](#) and [Figure S2](#).

(A) The bacterial photography circuit, where the β -galactosidase output is expressed directly under the control of the light-sensitive $P_{ompC1157}$ promoter. This produces a positive print of the projected image.

(B) Cell-cell communication components are added by placing *luxI* under the control of the dark sensor and expressing *luxR* constitutively. This produces a positive image with an additional blurring component due to AHL diffusion.

(C) A genetic inverter is inserted between the dark sensor input and the β -galactosidase output. This produces an inverted (negative) print of the image, where the light regions are printed as dark and vice-versa.

(D) A population of cells programmed with the complete edge detector system produces black pigment only at the boundary between light and dark regions. The model solutions are reported in Miller units (color bars, right).

properly matched; transcription from the X AND (NOT Y) gate can be controlled by AHL and CI over the output ranges generated by the dark sensor.

Assembling Circuits into the Full Program

[Figure 3](#) shows the stepwise assembly of the edge detection algorithm from the component genetic circuits. When a lawn of bacteria programmed with the edge detection algorithm is exposed to an image of light, the community prints the dark-light edges ([Figure 3D](#)), with an average edge width of 6.0 ± 1.8 mm ($n = 3$) ([Figure 5A](#)). [Figure 4](#) demonstrates that the bacterial lawns can accurately solve the edges of a circle, a square, and the silhouette of a man.

Reaction-Diffusion Model

A model of the complete edge detector system is constructed based on the individually measured dark sensor and logic transfer functions f_{light} and f_{logic} ([Experimental Procedures](#)). The model quantifies the dynamics of light-dependent production of AHL and CI, AHL diffusion, production of the β -galactosidase reporter and degradation of all products. Assuming that AHL diffusion is the slowest process, the system is described by the equations,

$$\frac{\partial u_1}{\partial t} = D \nabla^2 u_1 + \kappa_1 f_{\text{light}} - \kappa_2 u_1 \quad (3)$$

$$u_2 = \kappa_3 f_{\text{light}} \quad (4)$$

$$u_3 = \kappa_4 f_{\text{logic}}(u_1, u_2) \quad (5)$$

where u_1 is the AHL concentration on the plate (nM), u_2 is the concentration of CI dimers (nM), and u_3 is the concentration of β -galactosidase in Miller Units. The diffusivity and half-life of AHL are obtained from previously published values ($D = 1.67 \times 10^{-7}$ cm²/sec, $\kappa_2 = 0.012$ hr⁻¹) ([Basu et al., 2005](#); [Flagan et al., 2003](#)). The production rate of AHL is a function of the density of the bacteria on the plate and is obtained by fitting to the edge profile ($\kappa_1 = 0.03$ nM/hr). The maximum CI and β -galactosidase concentrations are determined by fitting the experimental data to the individual transfer functions ($\kappa_3 = 0.8$ nM/Miller, $\kappa_4 = 289$ Miller) ([Experimental Procedures](#)). Because the system is an agarose plate, the reaction-diffusion model is defined on polar coordinates with a no-flux boundary condition on the outer border.

The model accurately describes the pattern of β -galactosidase on a plate of bacteria expressing the edge detector and each of the sub-circuits for each of the light patterns shown in [Figures 3 and 4](#). The quantitative accuracy of the model is evaluated in [Figure 5](#). [Figure 5A](#) shows a one-dimensional analysis of the circle pattern where the in silico and in vivo edge intensity profiles are compared as a function of radial distance from the center. For complex images, the edge intensity is greater at acute angles and along convex arcs than flat edges. In these areas there are more cells producing AHL per unit area. This increases the local AHL concentration and consequently the β -galactosidase output in adjacent illuminated areas. The relationship between edge intensity and the angle of line intersection is also accurately captured by the model ([Figure 5B](#)).

Plate-Based Assays

The output of the edge detector and other circuits are assayed using plates that are developed in the light camera. Detailed instructions for these assays are provided in the [Supplemental Data](#). The agar slabs containing the bacteria are grown and exposed to light for 14 hr (Edge Detector, Inverter, Communication). The projector is then turned off and the slabs are allowed to 'develop' at 36°C in the dark for 10 hr. For photography the slabs are exposed to the image for 45 hr. The slabs are placed at 4°C overnight to stop bacterial growth and gene expression, before being photographed.

Image Analysis

Photographs of the bacterial plates are taken with a Canon SD900 digital camera. All four sample plates shown in [Figure 3](#) of the main text were taken in a single photograph and the brightness, levels and contrasts were optimized identically. This preserves the relative signal intensity of each of the plates.

Determination of Background Intensity

The background intensity is measured to be 75 (where 0 is pure white and 255 is pure black), which is the "leaky" pixel intensity value taken from the illuminated region of the plate of bacteria expressing the inverter circuit in [Figure 3C](#). This background intensity value is a constant through the entire image analysis.

Radial Edge Intensity Profiles

The radial edge intensity profiles in [Figure 5A](#) are extracted from the three circle images ([Figure S3](#)) (Matlab Image Processing Toolbox, Mathworks). These high resolution images are first converted to grayscale and subjected to a 5 point nearest neighbor smoothing to reduce digital artifacts. For each circle image, the radial pixel profile is calculated in the following way: starting from the center of each circle, the pixel intensities at each radial position ($r = 0$ to 2.8 cm) and at a constant θ coordinate are extracted. A set of radial pixel profiles are then extracted by performing this procedure while varying the θ coordinate. This set is then averaged together to create a mean radial pixel profile. This analysis is repeated for each circle image, creating a total of three independent mean radial pixel profiles. The background intensity is subtracted from each mean radial pixel profile. Then, each profile is divided by its radial pixel value at the $r = 0$ cm position, which is at the center of the circle, creating three independent fold-change edge profiles. The average and standard deviation of the fold-change edge profiles is computed.

Edge Intensity versus Angle

The raw grayscale pixel intensities from the asymmetrical silhouette mask are extracted at selected angle intersections (ImageJ, 1.40 g, Wayne Rasband, NIH) and background corrected. The background corrected intensities are then normalized by dividing by the maximum value in the data set ($x = 51^\circ$, $y = 1.0$ in [Figure 5B](#)). The experimental values are compared to Miller Unit predictions from varying the angle of intersection in the reaction diffusion model as described below.

Determination of an Average Edge Width

The average edge width and error presented in the main text is determined by repeating three separate 36 mm circle pattern plates on three different days. The plates ([Figure S3](#)) are photographed and analyzed using ImageJ 1.40 g (Wayne Rasband, NIH). Raw images are converted to grayscale and inverted. The horizontal pixel intensity profile across the plate is determined using rectangle probe traversing the center of the circle. The width of the edge is determined from the pixel intensity profile by drawing a straight line from the start of the edge (point of rapid signal intensity rise) to the point at which the signal intensity drops to the approximate average maximum signal intensity in the nearby internal illuminated area. Two edges (one from the left side of the circle and one from the right) are measured on each plate. The individual widths measured from the three plates in [Figure S3](#) are 0.86 cm, 0.76 cm, 0.46 cm, 0.62 cm, 0.37 cm, and 0.53 cm. The error values reported are the standard deviation.

Determination of the Dark Sensor Transfer Function, f_{light}

The transfer function of the dark sensor is determined in batch culture Miller Assay experiments using strain JW3367c carrying the plasmids pJT103,

pPLPCB and pCph8. pJT103 is comprised of the shortened P_{ompC} promoter (BBa_R0082) upstream of the strong RBS (BBa_B0034) (Elowitz and Leibler, 2000) and the *lacZ* ORF in the pSB4A3 backbone ([Figure S4](#)).

Overnight starter cultures are inoculated from -80°C stocks in 3 mL LB + Ampicillin, Kanamycin and Chloramphenicol and grown to $\text{OD}_{600} \sim 4$. Cultures are then diluted into 1 mL LB + 0.1M HEPES pH = 6.6 to a final OD_{600} of 0.001 and added to a single, internal well of a sterile 24-well plate (Falcon, Part# 351147). The plate (with lid on) is then fixed onto a VWR incubating mini shaker (Cat# 12620-942) from which the plastic lid has been removed, placed inside of a dark incubator, illuminated with a defined amount of 650 nm filtered light and shaken at 420 rpm for 330–345 min at 36°C. The light is measured as previously (Levsikaya et al., 2005) with the spectrometer probe placed at the position equivalent to the x, y center of the assay plate. The cultures, which have reached log phase (final OD_{600} between 0.6 and 1.2), are immediately collected under a safe green light and pipetted into black 1.7 mL microcentrifuge tubes. Then, 100 μL of each sample is immediately used to determine the OD_{600} while 350 μL is used for the Miller Assay.

The quantity f_{light} is the expression rate of the light-repressed BioBrick *ompC* promoter as a function of light input and has been experimentally determined using a β -galactosidase readout ([Figure 2A](#)). We fit the experimental data to the sigmoidal function,

$$f_{\text{light}} = \frac{K}{K + L} (\beta_{\text{max}} - \beta_{\text{min}}) + \beta_{\text{min}} \quad (1)$$

where the fit parameter is $K = 0.0017 \text{ W/m}^2$ ($R^2 = 0.75$), the maximum expression level $\beta_{\text{max}} = 298$ Miller Units, the minimum expression level $\beta_{\text{min}} = 125$ Miller Units, and the light intensity in units of W/m^2 passing through the mask at position (r, θ) is $L_{r,\theta}$.

Determination of the Logic Transfer Function, f_{logic}

The two-input transfer function of the signal integrating promoter $P_{\text{Lux-2}}$ (BBa_R0065) is determined in strain JW3367c carrying plasmids pJT104, pPLPCB and pCph8. pJT104 is the edge detection plasmid pED_3 from which the *luxI* ORF (BBa_C0061) has been removed ([Figure S5](#)). This allows independent control of CI and AHL abundance via light and exogenous addition to the media, respectively. The readout of the $P_{\text{Lux-2}}$ (BBa_R0065) promoter is β -galactosidase in Miller Units.

The quorum signal 3OC₆HSL (N-(b-Ketocaproyl)-L-homoserine lactone, Sigma-Aldrich# K3007) is added at different concentrations across different wells of the plate while a single light intensity is applied to the entire plate. The data in [Figure 2B](#) are the result of 25 data points taken as 5 sets of 5 points over 5 days, where the 5 data points for a given light intensity are collected on a single day. The cell cultures are in mid-log phase and typically between OD_{600} 0.6 and 0.85 at the time of the assay.

The steady-state concentration of β -gal is determined by the transcription rate of the LuxR-activated, CI-repressed $P_{\text{Lux-2}}$ promoter, which is quantified by the f_{logic} function. The Shea-Ackers formalism is used to enumerate the binding states of LuxR and CI bound to the promoter (Ackers et al., 1982; Bintu et al., 2005b). The steady-state concentration of β -galactosidase is proportional to the probability of RNA polymerase initiating transcription. The expression for $f_{\text{logic}}(u_1, u_2)$ is

$$f_{\text{logic}}(u_1, u_2) = \frac{(c_0 + c_1 f_{\text{Lux}})}{1 + c_0 + c_1 f_{\text{Lux}} + c_2 f_{\text{CI}} + c_1 c_2 f_{\text{Lux}} f_{\text{CI}}} \quad (2)$$

where $n = 1.5$ and f_{Lux} is the concentration of LuxR dimer bound to AHL ($K_D^{\text{LuxR}} = 270,000 \text{ nM}^3$, $\text{LuxR}_{\text{tot}} = 2000 \text{ nM}$) (Urbanowski et al., 2004), which is

$$f_{\text{Lux}} = \frac{1}{2} \left[\left(\text{LuxR}_{\text{tot}} + \frac{K_D^{\text{LuxR}}}{4u_1^2} \right) - \sqrt{\left(\text{LuxR}_{\text{tot}} + \frac{K_D^{\text{LuxR}}}{4u_1^2} \right)^2 - \text{LuxR}_{\text{tot}}} \right] \quad (6)$$

and f_{CI} is the concentration of dimeric CI ($K_D^{\text{CI}} = 5 \text{ nM}$ (Kobian and Ackers, 1991)), which is

$$f_{\text{CI}} = \frac{u_2}{2} + \frac{1}{8K_D^{\text{CI}}} \left(1 - \sqrt{1 + 8K_D^{\text{CI}} u_2} \right) \quad (7)$$

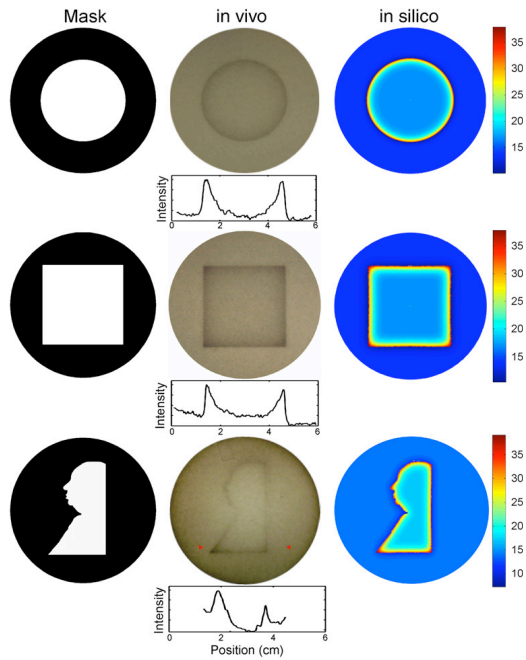


Figure 4. Edge Detection of Complex Patterns
 Circle (top), square (middle) and silhouette (bottom) images are projected onto lawns of bacteria programmed with the edge detector. Signal intensities and distances are shown under each bacterial lawn. For the asymmetrical silhouette pattern, the signal intensity profile is computed for a small horizontal rectangle centered at the two red arrows. The model solutions are reported in Miller units (color bars, right).

others, without unforeseen higher-order effects (Kim and Tidor, 2003). Here, we have demonstrated that a number of well-characterized genetic circuits can be reliably combined to create a larger program. Different circuit combinations produce expected behaviors that can be predicted by a mathematical model parameterized with data from the characterization of the individual circuits. This will not be true for all circuit combinations, and understanding the origins of higher-order effects and how they can be accounted for in the design process is an outstanding challenge (Arkin and Fletcher, 2006). As the programs become larger, it will also become increasingly important to include information on how the engineered circuits impose burdens upon the host cells, including transcriptional, translational, metabolic, and energy resources (Canton et al., 2008; Tabor et al., 2008). Detailed studies of the interactions between synthetic circuits and host systems (Guido et al., 2007) may lead to new conclusions regarding regulatory and metabolic cross-talk and the ability of cells to tolerate or adapt to increased genetic load.

DISCUSSION

Individual genetic circuits that mimic basic electronic functions have previously been constructed (Anderson et al., 2007; Atkinson et al., 2003; Basu et al., 2004; Elowitz and Leibler, 2000; Gardner et al., 2000; Guet et al., 2002; Ham et al., 2006; Yokobayashi et al., 2002). The next step is to understand how to combine these functions to create more complex genetic programs (Purnick and Weiss, 2009). This requires well-characterized parts and circuits that perform reliably when linked to

Logic and cell-cell communication form the core of regulatory networks that drive fundamental biological processes such as pattern formation (Kondo and Asai, 1995; Meinhardt and Gierer, 2000; Sick et al., 2006) and development (Freeman, 2000; Materna and Davidson, 2007). The combination of these two functions allows each cell in a population to respond appropriately to local signals without the need for information regarding its position within the global system. Here, we have programmed a population of bacteria to form a pattern corresponding to the edges within a projected image of light. As in natural systems,

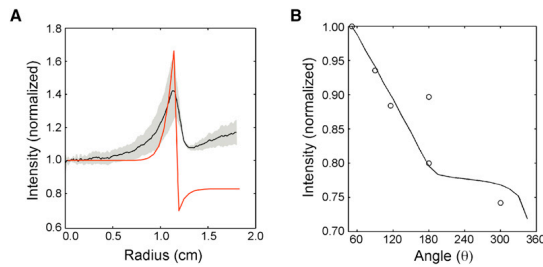


Figure 5. Quantitative Comparison of Model and Experimental Edges in One and Two Dimensions
 (A) Comparison of the in vivo (black) and in silico (red) radial intensity profiles for the circle pattern. The average of three circle images (Figure S3) is shown along with the standard deviation (gray region) (Experimental Procedures).
 (B) The relationship between the intersection angle (θ = degrees of light) of edges and the signal intensity is shown. Six points with five different θ values are sampled from the silhouette plate in Figure 4 (circles). The background intensity is subtracted from each point and the data is divided by the maximum intensity value. For each intersection angle, the maximum edge intensity is computed from the solution of the model with a unit circle mask with θ degrees of light (solid line) (Experimental Procedures).

communication greatly reduced the information-processing requirement for each member of the population while simple genetic logic allowed the proper integration of local signals for the formation of the final pattern.

Edge Detection is used for the identification of objects in a wide variety of *in silico* image processing applications (Suel et al., 2000) and has also been shown to be a natural function of the retina (Maturana and Frenk, 1963). *In silico* edge detection algorithms address each pixel of an image in series, resulting in a computation time that increases linearly with the number of pixels. In the bacterial edge detector the computation is massively parallel, resulting in a computation time that is independent of image size. This strategy is also an example of "Amorphous Computing" (Abelson et al., 2000) whereby a computation is performed as the emergent result of many spatially distributed processors working together locally without the need for global coordination. The applications of biological amorphous computers are still largely unexplored but are intriguing in light of the astounding feats of self-organization and information processing seen in natural pattern forming and neural network systems.

Several other efforts have leveraged cell-cell communication to program coordinated multicellular behaviors. These include a genetically-encoded turbidostat (You et al., 2004), one (Kobayashi et al., 2004) and two (Brenner et al., 2007) cell density-dependent transcription regulators, a transcriptional pulse generator (Basu et al., 2004), synthetic ecosystems (Balagadde et al., 2008; Weber et al., 2007) and a pattern forming system (Basu et al., 2005). In the latter case, two genetically distinct populations of bacteria (AHL senders and receivers) were manually overlaid in different configurations in order to generate different patterns. By contrast, the edge detector is implemented within an isogenic cell population that forms patterns in response to an external input with no requirements for cell placement.

Synthetic systems such as these could be used as early in vivo models for studying the 'design principles' that govern natural processes. Their simplicity and tractability makes them amenable to rigorous mathematical analysis, which can be used to generate rapidly testable hypotheses regarding the contribution of specific parameters to overall function. Because regulatory motifs recur ubiquitously in biology, the synthetic systems can then serve as working models for their natural counterparts (Sprinzak and Elowitz, 2005). The connection between primary DNA sequence and phenotype then closes the design cycle, expediting the engineering of novel biological behaviors.

The construction of very large fragments of DNA (Cello et al., 2002; Chan et al., 2005; Endy, 2008; Gibson et al., 2008a; Gibson et al., 2008b; Smith et al., 2003; Tumpey et al., 2005) is no longer a limitation in the engineering of biological systems. Predicting the behavior of complex genetic programs *de novo* is now the limiting step in the programming of cellular behavior. Thorough characterization of the performance of simple genetic parts and their resulting circuits will allow the development of predictive mathematical tools which will be required to program cells and cellular communities for functions which approach the sophistication of natural systems. This, in turn, will enable rigorous bottom-up testing of structure-function relationships in natural genetic systems.

EXPERIMENTAL PROCEDURES

Strain and Media

The strain for all experiments in this study is *E. coli* JW3367 (*E. coli* K12 W3110, *envZ-lacZ*- NCBI-GI: 89110606) from which the Kanamycin resistance marker is removed (termed JW3367c). Transformations are plated on LB agar supplemented with 50 µg/mL Kanamycin, 34 µg/mL Chloramphenicol and 50 µg/mL Ampicillin as necessary. The strains are maintained in LB + 0.1M HEPES pH = 8.0 supplemented with the antibiotics. Glycerol stocks of the strains are maintained by adding 300 µL 60% glycerol (sterile) to 700 µL actively growing culture (log phase) and freezing at -80°C.

Edge Detection Plasmids

E. coli JW3367c is transformed with the light sensing plasmids pPLPCB (p15a Kan^r) (Gambetta and Lagarias, 2001), pCph8 (ColE1, Cm^r) (Levskaya et al., 2005) and a third plasmid carrying the circuit. All of the circuit plasmids are based on the pSB4A3 BioBrick vector backbone (Shetty et al., 2008), which contains the pSC101⁺ origin of replication and Amp^r. The pSC101⁺ origin is carried at 2-3 copies per cell (Lutz and Bujard, 1997). The edge detector plasmid, pED₃, is constructed from a series of DNA parts many of which are BioBricks (Knight, 2002) (see the Supplemental Data available with this article online). Other functional DNA elements used in the construction of the edge detector are the weak ribosome binding site RBS3 (Weiss, 2001) and the ORF of the *lacZ* gene. The *lacZ* ORF is amplified from the plasmid pEXPlacZ (Invitrogen) using primers that encode the BioBricks prefix and suffix sequences, which carry the restriction sites EcoRI, XbaI (forward) and SpeI and PstI (reverse) respectively. This allows the *lacZ* gene to be cloned downstream of J13023 in its host plasmid via a suffix operation (Knight, 2002) using XbaI and PstI.

Photography, Inverter, and Communication Circuit Plasmids

The plasmids that carry the photography, inverter and cell-cell communication circuits are pJT108, pJT106 and pJT105, respectively. The plasmids pJT105 and pJT106 are constructed by deleting single genes from pED₃ using seamless inverse PCR and ligation with the Phusion Site Directed Mutagenesis Kit (Finnzymes, Woburn, MA) according to manufacturer's instructions. Plasmid pJT108 is constructed by amplifying the P_{ompC1157} genomic region of *E. coli* RU1012 (Utsumi et al., 1989) with overhanging homology regions to pJT103 and seamlessly replacing R0082 via the MEGAWHOP method (Miyazaki, 2003). The P_{ompC1157} promoter (pJT108) is used for the bacterial photographs because when read out by β-galactosidase directly, it produces smoother, higher contrast images than the shorter *ompC* promoter BBa_R0082.

Miller Assays

Miller Assays are conducted in 700 µL total volume with the Yeast β-Galactosidase Assay Kit (Pierce, Cat# 75768) in sterile, clear 1.7 mL microcentrifuge tubes at 28°C in ambient light according to the manufacturer's instructions. The reactions are quenched after visible yellow color develops and the OD₄₂₀ measurements are taken in VWR disposable cuvettes (VWR Cat# 97000-586) on a Cary 50 Bio spectrophotometer. The equation to calculate Miller Units is $(1000 \cdot OD_{420}) / (t \cdot V \cdot OD_{600})$, where *t* is the reaction time of the assay in minutes, and *V* is the volume of cell culture added to the reaction.

The Light Camera

A "Light Camera" (Incubator-Projector), which enables the projection of an image onto a plate of growing bacteria, is constructed as described before (Levskaya et al., 2005). A Kodak Ektagraphic III AMT projector equipped with an 82 V, 300 W Philips FocusLine quartz bulb is used as the light source. The broad wavelength light is filtered through a 650 nm bandpass filter (Edmund Optics catalog #43-189), stenciled through a 34x24 mm slide printed with a black and white image at 2032 dpi (mask), and focused through a lens. The images projected onto the slabs have power characteristics of 0.08 to 0.15 W/m² in the 620-680 nm band as determined by a EPP2000C Concave Grating spectrometer (Stellarnet, Oldsmar, FL). Dark areas of the images typically have 0.0000 to 0.0003 W/m² light over the same range. Bleedthrough light outside this band is negligible.

The constants c_0 to c_2 reflect the apparent in vivo Gibbs free energies of binding for each state and are determined by minimizing the differences between the output of f_{logic} and the two-input transfer function over the 25 different conditions of 3OC₆HSL concentration and light intensity. The best fit values are $c_0 = 0.04$, $c_1 = 0.05$ and $c_2 = 0.011$ ($R^2 = 0.81$).

Reaction-Diffusion Model

Given a light mask, the reaction-diffusion model calculates the time- and position-dependent expression level of the β -galactosidase (β -gal) output gene. The model consists of (1) a partial differential equation describing 3OC₆HSL production, degradation, and diffusion and (2) two algebraic equations describing the steady-state concentrations of Cl and β -gal in response to 3OC₆HSL and light. In dimensionless form, these equations are

$$\frac{\partial u_1}{\partial t^*} = \frac{1}{r} \frac{\partial u_1}{\partial r^*} + \frac{\partial^2 u_1}{\partial r^{*2}} + \frac{1}{r^2} \frac{\partial^2 u_1}{\partial \theta^2} + \kappa_1 f_{\text{light}} - \kappa_2 u_1 \quad (8)$$

$$u_2 = \kappa_3 f_{\text{light}} \quad (9)$$

$$u_3 = \kappa_4 f_{\text{logic}}(u_1, u_2) \quad (10)$$

Where u_1 , u_2 , and u_3 represent the concentrations of 3OC₆HSL, Cl, and β -gal at a position on the plate whose polar coordinates are given by (r, θ) . The f_{light} and f_{logic} functions quantify the transcription rates of the light-dependent *ompC* promoter and the Cl-repressed, LuxR::3OC₆HSL-activated *luxX*- λ promoter, respectively.

The constants κ_1 and κ_2 quantify the maximum production rate and the degradation rate of 3OC₆HSL, respectively. The production rate of 3OC₆HSL is estimated so that the maximum concentration on the plate is 2.5 nM while the degradation rate of 3OC₆HSL is slow; it has a half-life of about 2.5 days at pH 6.6 (Flagan et al., 2003). The conversion factor between the *ompC* transcription rate, characterized by f_{light} , and Cl concentration is $\kappa_3 = 0.8$ nM/Miller. The constant κ_4 is the maximum β -gal concentration, which is 289 Miller units. This value was determined in batch culture experiments as described above at 500 nM (maximum) exogenous AHL in the absence of any Cl protein (plasmid pJ105).

When solving these equations, the space and time coordinates are de-dimensionalized so that $r^* = r/R$ and $t^* = tD/R^2$ where r is the radial position from the center of the plate, R is the radius of the plate, t is time and $D = 1.67 \times 10^{-7}$ cm²/sec is the diffusivity of 3OC₆HSL (Basu et al., 2005). The system is an agarose plate with radius $R = 4.25$ cm (3.55 mm operating depth), homogeneously filled with stationary bacteria. Because the bacterial photographs are crisp in our system we assume that there is no appreciable bacterial movement in the agarose plates. There is a no-flux boundary condition (Neumann type) at $r^* = 1$ and a uniformly zero initial 3OC₆HSL concentration.

The differential equations in Equations (8–10) are solved using the finite difference method. We substitute 2nd order central differences for all spatial derivatives to create a sparse system of ordinary differential equations. The ordinary differential equations are solved using the Matlab (Mathworks, Natick, MA) ode23 s stiff numerical integrator with a final time of 24 hr ($t^* = 0.0027$). A sufficient number of radial and axial elements are used to accurately resolve each light mask. The solution yields the dynamics of edge formation in response to a given light mask.

Quantifying the Effect of Angle of Intersection on Edge Intensity

The effect of changing the angle of intersection between light and dark boundaries on the edge intensity is examined, comparing the model predictions to the experimentally observed behaviors. We create a series of unit circle *in silico* masks where θ degrees of the circle are in the light with 360- θ degrees in the dark and where θ is varied from 50 to 345 degrees. For each mask, the solution of the reaction-diffusion model is computed, which predicts the maximum edge intensity. The maximum edge intensity is the β -galactosidase concentration at the edge location. The model predictions compare favorably with the experimentally observed edge intensities of the asymmetrical silhouette mask at the selected angle intersections (Figure 5B). The image analysis procedure to obtain the experimental data is described above.

Calculating the Radial β -gal Profile

The radial edge intensity profile of the circle images are compared to the in silico radial β -galactosidase profile from the model solution (Figure 5A). We compute the in silico radial β -galactosidase profile by first inputting the circle light mask into the model and determining the solution. Then, the β -galactosidase concentration in terms of Miller units (u_3) is outputted along the radial coordinate ($r = 0$ to 1.8 cm) and divided by the value of u_3 at $r = 0$ to obtain the normalized intensity in Figure 5A.

SUPPLEMENTAL DATA

Supplemental Data include Supplemental Experimental Procedures, five figures, and Supplemental References and can be found with this article online at [http://www.cell.com/supplemental/S0092-8674\(09\)00509-1](http://www.cell.com/supplemental/S0092-8674(09)00509-1).

ACKNOWLEDGMENTS

We thank E.A. Davidson, L.A. Lavery, M. Levy, K. McGary, and A. Scouras for helpful discussions; A. Nishimura for the JW3367 *E. coli* strain; and L.A. Lavery, C. Conboy, and D. Endy for assistance with Biobrick construction. This work was supported by the National Science Foundation (SynBERC), NSF-BES0547637, NIH EY016546, NIH AI067699, NIH R01GM077040, Office of Naval Research, and the Pew and Packard Foundations. J.J.T. is supported by a Kirschstein National Research Service Award.

Received: January 30, 2009

Revised: March 9, 2009

Accepted: April 13, 2009

Published: June 25, 2009

REFERENCES

- Abelson, H., Allen, D., Coore, D., Hanson, C., Homsy, G., Knight, T.F., Nagpal, R., Rauch, E., Sussman, G.J., Weiss, R., et al. (2000). Amorphous computing. *Commun. ACM* 43, 74–82.
- Ackers, G.K., Johnson, A.D., and Shea, M.A. (1982). Quantitative model for gene regulation by lambda phage repressor. *Proc. Natl. Acad. Sci. USA* 79, 1129–1133.
- Ajo-Franklin, C.M., Drubin, D.A., Eskin, J.A., Gee, E.P., Landgraf, D., Phillips, I., and Silver, P.A. (2007). Rational design of memory in eukaryotic cells. *Genes Dev.* 21, 2271–2276.
- Anderson, J.C., Clarke, E.J., Arkin, A.P., and Voigt, C.A. (2006). Environmentally controlled invasion of cancer cells by engineered bacteria. *J. Mol. Biol.* 355, 619–627.
- Anderson, J.C., Voigt, C.A., and Arkin, A.P. (2007). Environmental signal integration by a modular AND gate. *Mol. Syst. Biol.* 3, 133.
- Andrianantoandro, E., Basu, S., Karig, D.K., and Weiss, R. (2006). Synthetic biology: New engineering rules for an emerging discipline. *Mol. Syst. Biol.* 2, 28.
- Arkin, A.P., and Fletcher, D.A. (2006). Fast, cheap and somewhat in control. *Genome Biol.* 7, 114.
- Atkinson, M.R., Savageau, M.A., Myers, J.T., and Ninfa, A.J. (2003). Development of genetic circuitry exhibiting toggle switch or oscillatory behavior in *Escherichia coli*. *Cell* 113, 597–607.
- Balagadde, F.K., Song, H., Ozaki, J., Collins, C.H., Barnet, M., Arnold, F.H., Quake, S.R., and You, L. (2008). A synthetic *Escherichia coli* predator-prey ecosystem. *Mol. Syst. Biol.* 4, 187.
- Basu, S., Gerchman, Y., Collins, C.H., Arnold, F.H., and Weiss, R. (2005). A synthetic multicellular system for programmed pattern formation. *Nature* 434, 1130–1134.
- Basu, S., Mehreja, R., Thiberge, S., Chen, M.T., and Weiss, R. (2004). Spatiotemporal control of gene expression with pulse-generating networks. *Proc. Natl. Acad. Sci. USA* 101, 6355–6360.

- Benner, S.A., and Sismour, A.M. (2005). Synthetic biology. *Nat. Rev. Genet.* 6, 533–543.
- Bintu, L., Buchler, N.E., Garcia, H.G., Gerland, U., Hwa, T., Kondev, J., Kuhlman, T., and Phillips, R. (2005a). Transcriptional regulation by the numbers: applications. *Curr. Opin. Genet. Dev.* 15, 125–135.
- Bintu, L., Buchler, N.E., Garcia, H.G., Gerland, U., Hwa, T., Kondev, J., and Phillips, R. (2005b). Transcriptional regulation by the numbers: models. *Curr. Opin. Genet. Dev.* 15, 116–124.
- Brenner, K., Karig, D.K., Weiss, R., and Arnold, F.H. (2007). Engineered bidirectional communication mediates a consensus in a microbial biofilm consortium. *Proc. Natl. Acad. Sci. USA* 104, 17300–17304.
- Canton, B., Labno, A., and Endy, D. (2008). Refinement and standardization of synthetic biological parts and devices. *Nat. Biotechnol.* 26, 787–793.
- Cello, J., Paul, A.V., and Wimmer, E. (2002). Chemical synthesis of poliovirus cDNA: generation of infectious virus in the absence of natural template. *Science* 297, 1016–1018.
- Chan, L., Kosuri, S., and Endy, D. (2005). Refactoring bacteriophage T7. *Mol. Syst. Biol.* 26, 787.
- Cox, R.S., 3rd, Surette, M.G., and Elowitz, M.B. (2007). Programming gene expression with combinatorial promoters. *Mol. Syst. Biol.* 3, 145.
- Elowitz, M.B., and Leibler, S. (2000). A synthetic oscillatory network of transcriptional regulators. *Nature* 403, 335–338.
- Endy, D. (2005). Foundations for engineering biology. *Nature* 438, 449–453.
- Endy, D. (2008). Genomics. Reconstruction of the genomes. *Science* 319, 1196–1197.
- Engelbrecht, J., and Silverman, M. (1984). Identification of genes and gene products necessary for bacterial bioluminescence. *Proc. Natl. Acad. Sci. USA* 81, 4154–4158.
- Flagan, S., Ching, W.K., and Leadbetter, J.R. (2003). Arthrobacter strain VAI-A utilizes acyl-homoserine lactone inactivation products and stimulates quorum signal biodegradation by *Variovorax paradoxus*. *Appl. Environ. Microbiol.* 69, 909–916.
- Freeman, M. (2000). Feedback control of intercellular signalling in development. *Nature* 408, 313–319.
- Fung, E., Wong, W.W., Suen, J.K., Bulter, T., Lee, S.G., and Liao, J.C. (2005). A synthetic gene-metabolic oscillator. *Nature* 435, 118–122.
- Gambetta, G.A., and Lagarias, J.C. (2001). Genetic engineering of phytochrome biosynthesis in bacteria. *Proc. Natl. Acad. Sci. USA* 98, 10566–10571.
- Gardner, T.S., Cantor, C.R., and Collins, J.J. (2000). Construction of a genetic toggle switch in *Escherichia coli*. *Nature* 403, 339–342.
- Gibson, D.G., Benders, G.A., Andrews-Pfannkoch, C., Denisova, E.A., Baden-Tilson, H., Zaveri, J., Stockwell, T.B., Brownley, A., Thomas, D.W., Algire, M.A., et al. (2008a). Complete chemical synthesis, assembly, and cloning of a *Mycoplasma genitalium* genome. *Science* 319, 1215–1220.
- Gibson, D.G., Benders, G.A., Axelrod, K.C., Zaveri, J., Algire, M.A., Moodie, M., Montague, M.G., Venter, J.C., Smith, H.O., and Hutchison, C.A., 3rd. (2008b). One-step assembly in yeast of 25 overlapping DNA fragments to form a complete synthetic *Mycoplasma genitalium* genome. *Proc. Natl. Acad. Sci. USA* 105, 20404–20409.
- Guet, C.C., Elowitz, M.B., Hsing, W., and Leibler, S. (2002). Combinatorial synthesis of genetic networks. *Science* 296, 1466–1470.
- Guido, N.J., Lee, P., Wang, X., Elston, T.C., and Collins, J.J. (2007). A pathway and genetic factors contributing to elevated gene expression noise in stationary phase. *Biophys. J.* 93, 55–57.
- Guido, N.J., Wang, X., Adalsteinsson, D., McMillen, D., Hastly, J., Cantor, C.R., Elston, T.C., and Collins, J.J. (2006). A bottom-up approach to gene regulation. *Nature* 439, 856–860.
- Ham, T.S., Lee, S.K., Keasling, J.D., and Arkin, A.P. (2006). A tightly regulated inducible expression system utilizing the *fin* inversion recombination switch. *Biotechnol. Bioeng.* 94, 1–4.
- Haseltine, E.L., and Arnold, F.H. (2007). Synthetic gene circuits: design with directed evolution. *Annu. Rev. Biophys. Biomol. Struct.* 36, 1–19.
- Kim, J.H., Kim, H.Y., and Lee, Y.S. (2001). A novel method using edge detection for signal extraction from cDNA microarray image analysis. *Exp. Mol. Med.* 33, 83–88.
- Kim, P.M., and Tidor, B. (2003). Limitations of quantitative gene regulation models: a case study. *Genome Res.* 13, 2391–2395.
- Knight, T. (2002). Idempotent vector design for the standard assembly of biobricks. MIT Synthetic Biology Working Group Technical Report 0.
- Kobayashi, H., Kaern, M., Araki, M., Chung, K., Gardner, T.S., Cantor, C.R., and Collins, J.J. (2004). Programmable cells: interfacing natural and engineered gene networks. *Proc. Natl. Acad. Sci. USA* 101, 8414–8419.
- Koblan, K.S., and Ackers, G.K. (1991). Energetics of subunit dimerization in bacteriophage lambda cI repressor: linkage to protons, temperature, and KCl. *Biochemistry* 30, 7817–7821.
- Kondo, S., and Asai, R. (1995). A Reaction-Diffusion Wave on the Skin of the Marine Angelfish *Pomacanthus*. *Nature* 376, 765–768.
- Kramer, B.P., and Fussenegger, M. (2005). Hysteresis in a synthetic mammalian gene network. *Proc. Natl. Acad. Sci. USA* 102, 9517–9522.
- Kramer, B.P., Viretta, A.U., Daoud-El-Baba, M., Auel, D., Weber, W., and Fussenegger, M. (2004). An engineered epigenetic transgene switch in mammalian cells. *Nat. Biotechnol.* 22, 867–870.
- Levsikaya, A., Chevalier, A.A., Tabor, J.J., Simpson, Z.B., Lavery, L.A., Levy, M., Davidson, E.A., Scouras, A., Ellington, A.D., Marcotte, E.M., et al. (2005). Synthetic biology: engineering *Escherichia coli* to see light. *Nature* 438, 441–442.
- Lutz, R., and Bujard, H. (1997). Independent and tight regulation of transcriptional units in *Escherichia coli* via the LacR/O, the TetR/O and AraC/1–12 regulatory elements. *Nucleic Acids Res.* 25, 1203–1210.
- Materna, S.C., and Davidson, E.H. (2007). Logic of gene regulatory networks. *Curr. Opin. Biotechnol.* 18, 351–354.
- Maturana, H.R., and Frenk, S. (1963). Directional Movement and Horizontal Edge Detectors in the Pigeon Retina. *Science* 142, 977–979.
- Mayo, A.E., Setty, Y., Shavit, S., Zaslaver, A., and Alon, U. (2006). Plasticity of the cis-regulatory input function of a gene. *PLoS Biol.* 4, e45. 10.1371/journal.pbio.0040045.
- Meinhardt, H., and Gierer, A. (2000). Pattern formation by local self-activation and lateral inhibition. *Bioessays* 22, 753–760.
- Miyazaki, K. (2003). Creating random mutagenesis libraries by megaprimer PCR of whole plasmid (MEGAWHOP). *Methods Mol. Biol.* 231, 23–28.
- Purnick, P.E., and Weiss, R. (2009). The second wave of synthetic biology: from modules to systems. *Nat. Rev. Mol. Cell. Biol.* 10, 410–422.
- Rackham, O., and Chin, J.W. (2005). Cellular logic with orthogonal ribosomes. *J. Am. Chem. Soc.* 127, 17584–17585.
- Shea, M.A., and Ackers, G.K. (1985). The OR control system of bacteriophage lambda. A physical-chemical model for gene regulation. *J. Mol. Biol.* 181, 211–230.
- Shetty, R.P., Endy, D., and Knight, T.F., Jr. (2008). Engineering BioBrick vectors from BioBrick parts. *J. Biol. Eng.* 2, 5.
- Sick, S., Reinker, S., Timmer, J., and Schlake, T. (2006). WNT and DKK determine hair follicle spacing through a reaction-diffusion mechanism. *Science* 314, 1447–1450.
- Smith, H.O., Hutchison, C.A., 3rd, Pfannkoch, C., and Venter, J.C. (2003). Generating a synthetic genome by whole genome assembly: phiX174 bacteriophage from synthetic oligonucleotides. *Proc. Natl. Acad. Sci. USA* 100, 15440–15445.
- Sprinzak, D., and Elowitz, M.B. (2005). Reconstruction of genetic circuits. *Nature* 438, 443–448.
- Stricker, J., Cookson, S., Bennett, M.R., Mather, W.H., Tsirring, L.S., and Hastly, J. (2008). A fast, robust and tunable synthetic gene oscillator. *Nature* 456, 516–519.
- Suel, M., O’Gorman, L., and Sammon, M.J. (2000). Practical Algorithms for Image Analysis.

- Tabor, J.J., Bayer, T.S., Simpson, Z.B., Levy, M., and Ellington, A.D. (2008). Engineering stochasticity in gene expression. *Mol. Biosyst.* 4, 754–761.
- Tabor, J.J., Groban, E.S., and Voigt, C.A. (2009). Performance characteristics for sensors and circuits used to program *E.coli*. In *Systems Biology and Biotechnology of Escherichia coli*, S.Y. Lee, ed. (New York: Springer), pp. 401–439.
- Tigges, M., Marquez-Lago, T.T., Stelling, J., and Fussenegger, M. (2009). A tunable synthetic mammalian oscillator. *Nature* 457, 309–312.
- Tumpey, T.M., Basler, C.F., Aguilar, P.V., Zeng, H., Solorzano, A., Swayne, D.E., Cox, N.J., Katz, J.M., Taubenberger, J.K., Palese, P., et al. (2005). Characterization of the reconstructed 1918 Spanish influenza pandemic virus. *Science* 310, 77–80.
- Urbanowski, M.L., Lostroh, C.P., and Greenberg, E.P. (2004). Reversible acyl-homoserine lactone binding to purified *Vibrio fischeri* LuxR protein. *J. Bacteriol.* 186, 631–637.
- Utsumi, R., Brissette, R.E., Rampersaud, A., Forst, S.A., Oosawa, K., and Inouye, M. (1989). Activation of bacterial porin gene expression by a chimeric signal transducer in response to aspartate. *Science* 245, 1246–1249.
- Voigt, C.A. (2006). Genetic parts to program bacteria. *Curr. Opin. Biotechnol.* 17, 548–557.
- Weber, W., Daoud-Ei Baba, M., and Fussenegger, M. (2007). Synthetic ecosystems based on airborne inter- and intrakingdom communication. *Proc. Natl. Acad. Sci. USA* 104, 10435–10440.
- Weiss, R. (2001). *Cellular Computation and Communications Using Engineered Genetic Regulatory Networks*.
- Weiss, R., Homsy, G.E., and Knight, T.F., Jr. (1999). Toward in vivo digital circuits. *DIMACS Workshop on Evolution as Computation* 1, 1–18.
- Weiss, R., and Knight, T.F., Jr. (2001). *Engineering Communications for Microbial Robotics*. In *Lecture Notes In Computer Science* (Heidelberg: Springer), pp. 1–16.
- Yeh, K.C., Wu, S.H., Murphy, J.T., and Lagarias, J.C. (1997). A cyanobacterial phytochrome two-component light sensory system. *Science* 277, 1505–1508.
- Yokobayashi, Y., Weiss, R., and Arnold, F.H. (2002). Directed evolution of a genetic circuit. *Proc. Natl. Acad. Sci. USA* 99, 16587–16591.
- You, L., Cox, R.S., 3rd, Weiss, R., and Arnold, F.H. (2004). Programmed population control by cell-cell communication and regulated killing. *Nature* 428, 868–871.

Spatiotemporal Control of Cell Signalling and Morphology Using a Genetically-Encoded Light-Switchable Interaction

Anselm Levskaya^{1,2,3}, Orion D. Weiner^{1,4}, Wendell A. Lim^{1,5*}, Christopher A. Voigt^{1,3}

¹*The Cell Propulsion Lab, UCSF/UCB NIH Nanomedicine Development Center*

²*Graduate Program in Biophysics*

³*Dept. of Pharmaceutical Chemistry*

⁴*Cardiovascular Research Institute*

⁵*Howard Hughes Medical Institute and Dept. of Cellular and Molecular Pharmacology*

University of California, San Francisco, California, 94158-2517

*To whom correspondence should be addressed (email: lim@cmp.ucsf.edu)

Genetically-encodable optical reporters, such as Green Fluorescent Protein, have revolutionized the observation and measurement of cellular states. However, the inverse challenge of using light to precisely control cellular behavior has only recently begun to be addressed; semi-synthetic chromophore-tethered receptors¹ and naturally-occurring channel rhodopsins have been used to directly perturb neuronal networks^{2,3}. The difficulty of engineering light sensitive proteins remains a significant impediment to the optical control to most cell-biological processes. Here we demonstrate the use of a new genetically-encoded light-control system based on an optimized reversible protein-protein interaction from the phytochrome signaling network of *Arabidopsis thaliana*. Because protein-protein interactions are one of the most general currencies of cellular information, this system can in principal be generically used to control diverse functions. Here we show that this system can be used to precisely and reversibly translocate target proteins to the membrane with micrometer spatial resolution and second time resolution. We show that light-gated translocation of the upstream activators of rho-family GTPases, which control the actin cytoskeleton, can be used to precisely reshape and direct the cell morphology of mammalian cells. The light-gated protein-protein interaction that has been optimized in this work should be useful for the design of diverse light-programmable reagents, potentially enabling a new generation of perturbative, quantitative experiments in cell biology.

In order to experimentally address the quantitative behaviour of living cells it is necessary to develop general strategies for both monitoring and dynamically controlling the activities of their constituent proteins at fine spatial and temporal resolutions. By measuring the responses to time-varying perturbations of the cell's networks as they propagate through signalling and effector nodes, predictive models of systems can be tested and iteratively improved. Recent work employing oscillating nutrient concentrations in yeast has demonstrated the utility of such dynamic perturbations for systems biology.^{4,5} However, it is generally difficult to control the

activity of an arbitrary signalling pathway at the relevant length- and time-scales. One promising approach is to couple the activity of targeted proteins to light signals, either by incorporating photoactive allosteric modulators semisynthetically^{1,6,7}, or by exploiting naturally-occurring light-sensitive domains^{2,3,8-10}. A particularly useful light-sensitive interaction for creating a general genetically-encoded light-control system for cell biology comes from the phytochrome signalling network of plants.

Phytochromes are photoreceptive signalling proteins responsible for mediating many light-sensitive processes in plants, including seed germination, seedling de-etiolation, and shade-avoidance.¹¹ They detect red and near-infrared light through the photoisomerization of a covalently-bound tetrapyrrole chromophore such as phycocyanobilin (PCB).¹¹ This photoisomerization event is coupled to an allosteric transition in the phytochrome between two conformational states called Pr (Red-absorbing) and Pfr (Far-Red-absorbing). (Fig. 1a) In one well-studied signalling pathway, upon stimulation with red (650 nm) light, the *Arabidopsis thaliana* phytochrome B (phyB) protein binds directly to a downstream transcription factor, Phytochrome Interaction Factor 3 (PIF3), translocates to the nucleus as a heterodimer and directly modulates the transcription of response genes. PIF3 binds only the red-light exposed form of phytochrome, Pfr, and shows no measurable binding affinity for the dark- or infrared-exposed Pr state.¹² Thus, this interaction can be reversed by infrared light. This light-sensitive interaction has been mapped to the 650 residue N-terminal photosensory core of PhyB and a conserved 100 residue N-terminal Activated Phytochrome Binding (APB) domain of PIF3.¹³

In previous work, this light-sensitive interaction has been used in yeast to construct a photoreversible two-hybrid transcriptional activator to tune the expression level of a targeted reporter gene¹⁰, to target split intein domains to titrate the conditional protein splicing of a reporter gene¹⁴, and *in vitro* to directly target Cdc42 to its effector WASP to regulate actin

Levsikaya et.al.

nucleation.¹⁵ Collectively this work suggests that the phyB-PIF interaction can be functionally coupled to a wide variety of signalling processes through engineered fusion proteins.

To date, however, no reported system employing the phyB-PIF interaction has been demonstrated to enable fine spatiotemporal control of dimerization *in vivo*. Indeed, the relatively weak binding strength and slow reverse kinetics of the reported domains¹⁵ have prevented us from successfully applying these earlier interaction pairs for *in vivo* control of signalling. We have optimized the phytochrome interaction to enable its spatiotemporal control in experiments with live mammalian cells.

We first confirmed that PhyB could covalently bind externally supplied PCB chromophore in mammalian cells by utilizing a PhyB mutant (Y276H) that fluoresces at far-red frequencies in the PCB-coupled state only.¹⁶ NIH3T3 cells transfected with this construct show fluorescence after only 30min of exposure to 5 μ M PCB, confirming rapid autoligation at physiological conditions.(Fig. S1) Multiple potential phytochrome-PIF pairs were screened by a fluorescence translocation assay in NIH3T3 cells with confocal microscopy. We measured the red-light-induced translocation of Yellow Fluorescent Protein (YFP) fused to PIF domains to coexpressed phytochrome domains fused through a flexible linker to mCherry and localized to the plasma membrane by a C-terminal polybasic, prenylation sequence from Kras.¹⁷ (Fig. 1b). Of all previously reported PIF domains^{13,18,19}, only the N-terminus of PIF6 is strong enough to cause significant translocation of YFP to the membrane. (Fig. 1c) However, its interaction with the PhyB photosensory core (residues 1-650) is irreversible in infra-red light. Assaying it against different variants of PhyB revealed that the tandem C-terminal PAS domains of plant phytochromes are necessary to confer rapid photo-reversibility under infra-red light, underlining the importance of a previously reported autoinhibitory interaction for phytochrome signalling.²⁰ We refer to the optimized, reversible PhyB-PIF6 interaction simply as the “phy-pif” interaction.

Using this optimized phy-pif pair we observe rapid translocation to the plasma membrane under dilute red light ($650\text{nm } 20\mu\text{mol m}^{-2} \text{s}^{-1}$) and from the membrane under infra-red light ($>750\text{nm } 300\mu\text{mol m}^{-2} \text{s}^{-1}$). (Fig. 2a, Supplemental Movies 1,2) (These photon fluxes are tiny compared to those typical for GFP excitation: $40\text{mmol m}^{-2} \text{s}^{-1}$ from an arc-lamp or $10^4 \text{mol m}^{-2} \text{s}^{-1}$ from an argon laser). Kinetic measurements of the phy-induced cytoplasmic depletion of pif-YFP under maximum illumination yield translocation time constants of $1.3\pm 0.1\text{s}$ (s.d. $n=3$) for membrane recruitment and $4\pm 1\text{s}$ (s.d. $n=3$) for membrane release (Fig. 2a, S2), demonstrating second-timescale control. These rates are an order of magnitude faster than previous chemically-induced translocation systems²¹ and are very near the physical limits for whole-cell diffusion. (See Supplemental Calculation) The phy-pif translocation proved very robust -- it could be cycled over a hundred times by alternating red and infrared illumination with no measurable decrease in recruitment ratios over time, despite many cycles of imaging at photon fluxes far higher than those phytochromes are exposed to in natural lighting conditions. (Fig. 2b, Supplemental Movie 3).

The rapid forward and reverse kinetics of our phy-pif pair allow for fine spatial control of membrane recruitment by simultaneously exposing cells to patterned light at the two antagonizing wavelengths. In NIH3T3 cells coexpressing the above phy-KrasCAAX pif-YFP recruitment pair, a nitrogen dye cell laser was used to deliver pulses of “activating” red light (650nm , 20Hz) to a focused point on the sample plane, while the whole sample was bathed in continuous “inactivating” infrared light obtained by filtering the microscope brightfield source ($>750\text{nm}$). (Fig. 3a) When the cell membrane is imaged by total internal reflectance (TIRF) microscopy we observe a sharp spot of membrane-localized YFP several microns in diameter around the irradiated point. (Fig. 3c) The rapid ‘off’ kinetics of the phy-pif interaction traps the membrane-recruited YFP pool to this spot, since any YFP diffusing away is dissociated from the membrane by the surrounding infrared light. This spot of recruited YFP can be rapidly relocated across the cell by repositioning the point of incident light. (Supplemental Movie 4)

Levskaya et.al.

We developed a second, fully automated method of controlling the distribution of both light frequencies on the cell membrane by using a digital micromirror array to project patterned light onto the sample plane of the microscope at micron resolutions.²² By irradiating the sample with 650nm and 750nm light sources oriented to take advantage of both micromirror angle states a complementary two-color red/infrared pattern can be projected onto the sample plane, allowing one to “paint” high-resolution inverse distributions of Pfr and Pr phytochrome onto the membrane of the cell. (Fig. 3b) We were able to faithfully project a simple pixel-based movie into the membrane-recruited pif-YFP distribution of a NIH3T3 cell. TIRF imaging reveals fine features at five microns, demonstrating an unprecedented degree of control over protein localization in living cells.(Fig. 3d, Supplemental Movie 5). Additionally, by dithering the average amount of red-light in the target mask through software, we could smoothly titrate the fraction of active phy and recruited pif-YFP, demonstrating effective “greyscale” control of the chemical potential. (Fig. 3e, Supplemental Movie 6). Using this data, we estimate the in vivo dissociation constant of the phyB-pif6 interaction to be approximately $K_d = 20\text{-}100\text{nM}$ (Fig. S5).

We were motivated to engineer a membrane recruitment system because many signalling proteins are, at least in part, activated by interactions that relocalize them to the membrane. Moreover, plasma membrane recruitment systems have been successfully used as a platform for small-molecule-induced chemical biology control systems.^{21,23-25} For example, chemically induced membrane translocation of the rho- and ras-family small G-proteins^{21,23} or the guanine nucleotide exchange factors (GEFs) that activate them²¹ can generate global morphological changes. We reasoned that phy-pif induced translocation could generate similar morphological changes, but with much higher spatial and temporal resolution. We chose to focus on spatiotemporal control of the Rho-family GTPases Rac1, Cdc42, and RhoA given their central role in the dynamic spatial regulation of the actin cytoskeleton at the polarized edges of motile cells. (Fig. 4a)

Gated-recruitment constructs were made from the isolated catalytic modules (the DH-PH domain) of the Rac-GEF Tiam, the Cdc42 GEF Intersectin, and the Rho-GEF Tim. The optimal construct topologies for DHPH activation were found by screening for Tiam DHPH activity via the global morphological changes that occurred in transfected, serum-depleted NIH3T3 cells when the entire field was exposed to red light. Global recruitment of the optimal pif-Tiam-DHPH chimera caused a pronounced lamellipodial phenotype within twenty minutes in the majority (>80%) of cotransfected cells, compared to pif-YFP-only recruitment or control cells lacking the PCB chromophore. (Fig. 4b). This potent effect of recruiting the Tiam GEF activity to the membrane is similar to that observed using chemical dimerizers²¹. We further tested the generality of this construct topology by confirming that global RhoGEF recruitment induced cell body contraction in fibroblasts. (Supplemental Movie 9)

Given the strong global morphological effects of Tiam DH-PH domain membrane translocation, we then tested the effects of spatially localized light-activated translocation. Red laser stimulation was used for localized recruitment of the Tiam DH-PH domain in serum-depleted NIH3T3 cells (within a background of global repression by infrared light), effecting within 5-10 minutes a localized lamellipodial ‘bloom’. (Supplemental Movie 8) By slowly extending the point of activating light away from the cell, it is even possible to “draw out” an extended process up to 30µm from the main body of the cell that is stable after the light has been withdrawn. This suggests the future possibility of programmatically specifying cell geometries and intercellular connections with light. (Fig. 4c, Supplemental Movies 7-8).

We further verified the signalling activity of our pif-DHPH reagents by verifying that point induction causes local, transient increases of the active form of GTPase as measured by the membrane enrichment of biosensors—either mCherry tagged GBD binding domains from WASP (Fig 4d, Supplemental Movie 11) or PAK (Fig. S4)—by TIRF microscopy. Using these biosensors we see that GTPase activation occurs rapidly—within seconds—indicating that a

Levskaya et.al.

subsequent signalling step is responsible for the typical delay of 5-10 minutes for lamellipodial and filopodial protrusions.

In summary, we have developed a genetically-encoded, light-switchable “phy-pif” interaction module which, because it has a properly titrated tight but reversible interaction, has the potential to be applied to control any live cell process that is dependent on a recruitment event. Unlike classical uncaging techniques, photoreversibility allows our system to defeat diffusive spreading by using patterned light. Further, the direct relationship between the recruited fluorescent fraction and signalling activity also enables measurable ‘dosage’ of signalling flux for quantitative perturbations. We show here that the system works robustly in mammalian cells with external PCB, extending previous demonstrations in yeast¹⁰ and its natural domain in plants, suggesting that it is compatible with most eukaryotic cells. For genetically manipulable cells, it is in principle simple to include genes for enzymes that will generate PCB from heme or biliverdin.²⁶

The high spatial and temporal resolution of light control allows this module to function as novel analytical tool, in which highly complex spatial or temporal patterns can be used to drive a process. We have also demonstrated here how this module can be used as a high resolution control module to sculpt cell shape in an unprecedented manner. Because of the generic nature of this interaction module, it is likely that it can be used to control an extremely broad range of cell biological processes without the need for laborious case-by-case protein engineering.

Methods

For detailed information on all methods, see Supplementary Information.

Phycocyanobilin (PCB) Purification. PCB was extracted by methanolysis at 70°C from protein precipitates of *Spirulina* cell lysate (Seltzer Chemical) that were pre-washed to remove other tetrapyrroles species. Free PCB was handled under a green safelight (λ_{\max} 550nm).

Light Control Experiments. NIH3T3 cells transiently transfected with the phytochrome and PIF constructs were pre-incubated in the dark with 5 μ M PCB for 30min and then washed before experiments. Noncoherent control-light frequencies were obtained by filtering white-light sources with 650nm and 750nm 20nm bandpass filters (Edmund Optics) or a near-infrared RG9 glass filter (Newport). For morphology experiments, cells were serum-depleted (1% Bovine Calf Serum) for at least twelve hours before imaging.

References

1. Szobota, S. *et al.* Remote control of neuronal activity with a light-gated glutamate receptor. *Neuron* **54**, 535-45 (2007).
2. Boyden, E.S., Zhang, F., Bamberg, E., Nagel, G. & Deisseroth, K. Millisecond-timescale, genetically targeted optical control of neural activity. *Nat. Neurosci.* **8**, 1263-8 (2005).
3. Han, X. & Boyden, E.S. Multiple-color optical activation, silencing, and desynchronization of neural activity, with single-spike temporal resolution. *PLoS ONE* **2**, e299 (2007).
4. Mettetal, J.T., Muzzey, D., Gómez-Urbe, C. & van Oudenaarden, A. The frequency dependence of osmo-adaptation in *Saccharomyces cerevisiae*. *Science* **319**, 482-4 (2008).
5. Bennett, M.R. *et al.* Metabolic gene regulation in a dynamically changing environment. *Nature* **454**, 1119-22 (2008).
6. Ghosh, M. *et al.* Cofilin promotes actin polymerization and defines the direction of cell motility. *Science* **304**, 743-6 (2004).

Levskaya et.al.

7. Gorostiza, P. & Isacoff, E.Y. Optical switches for remote and noninvasive control of cell signaling. *Science* **322**, 395-9 (2008).
8. Levskaya *et al.* Synthetic biology: engineering *Escherichia coli* to see light. *Nature* **438**, 441-2 (2005).
9. Lee, J. *et al.* Surface sites for engineering allosteric control in proteins. *Science* **322**, 438-42 (2008).
10. Shimizu-Sato, S., Huq, E., Tepperman, J.M. & Quail P.H. A light-switchable gene promoter system. *Nat. Biotechnol.* **20**, 1041-4 (2002).
11. Quail, P.H. Phytochrome photosensory signalling networks. *Nat. Rev. Mol. Cell Biol.* **3**, 85-93 (2002).
12. Ni, M. Tepperman, J.M. & Quail, P.H. Binding of phytochrome B to its nuclear signalling partner PIF3 is reversibly induced by light. *Nature* **400**, 781-4 (1999).
13. Khanna, R. *et al.* A novel molecular recognition motif necessary for targeting photoactivated phytochrome signaling to specific basic helix-loop-helix transcription factors. *Plant Cell* **16**, 3033-44 (2004).
14. Tyszkiewicz, A.B. & Muir, T.W. Activation of protein splicing with light in yeast. *Nat Methods* **5**, 303-5 (2008).
15. Leung, D.W., Otomo, C., Chory, J. & Rosen, M.K. Genetically encoded photoswitching of actin assembly through the Cdc42-WASP-Arp2/3 complex pathway. *Proc. Natl. Acad. Sci. U.S.A.* **105**, 12797-802 (2008).
16. Su, Y. & Lagarias J.C. Light-Independent Phytochrome Signaling Mediated by Dominant GAF Domain Tyrosine Mutants of Arabidopsis Phytochromes in Transgenic Plants. *Plant Cell* **19**, 2124-39 (2007).

17. Heo, W.D. *et al.* PI(3,4,5)P3 and PI(4,5)P2 lipids target proteins with polybasic clusters to the plasma membrane. *Science* **314**, 1458-61 (2006).
18. Al-Sady, B., Ni, W., Kircher, S., Schäfer, E., & Quail, P.H. Photoactivated phytochrome induces rapid PIF3 phosphorylation prior to proteasome-mediated degradation. *Mol. Cell* **23**, 439-46 (2006).
19. Genoud, T. *et al.* FHY1 mediates nuclear import of the light-activated phytochrome A photoreceptor. *PLoS Genet* **4**, e1000143 (2008).
20. Chen, M., Tao, Y., Lim, J., Shaw, A. & Chory J. Regulation of phytochrome B nuclear localization through light-dependent unmasking of nuclear-localization signals. *Curr. Biol.* **15**, 637-42 (2005).
21. Inoue, T., Heo, W.D., Grimley, J.S., Wandless, T.J. & Meyer T. An inducible translocation strategy to rapidly activate and inhibit small GTPase signaling pathways. *Nat. Methods* **2**, 415-8 (2005).
22. Wang, S. *et al.* All optical interface for parallel, remote, and spatiotemporal control of neuronal activity. *Nano Lett* **7**, 3859-63 (2007).
23. Castellano, F. *et al.* Inducible recruitment of Cdc42 or WASP to a cell-surface receptor triggers actin polymerization and filopodium formation. *Curr. Biol.* **9**, 351-60 (1999).
24. Suh, B., Inoue, T., Meyer, T. & Hille, B. Rapid chemically induced changes of PtdIns(4,5)P2 gate KCNQ ion channels. *Science* **314**, 1454-7 (2006).
25. Inoue, T. & Meyer, T. Synthetic activation of endogenous PI3K and Rac identifies an AND-gate switch for cell polarization and migration. *PLoS ONE* **3**, e3068 (2008).
26. Gambetta, G.A. & Lagarias, J.C. Genetic engineering of phytochrome biosynthesis in bacteria. *Proc. Natl. Acad. Sci. U.S.A.* **98**, 10566-71 (2001).

Levskaya et.al.

Supplementary Information is linked to the online version of the paper at www.nature.com/nature.

Acknowledgements We thank Bassem El-Sady, James Tepperman, Kurt Thorn, Greg Kapp, and members of the Voigt, Weiner, and Lim laboratories of assistance and discussion. We thank Molecular Devices and Photonics Instruments for the loan and customization of a Mosaic spatial light modulator. Data for this study were acquired at the Nikon Imaging Center at UCSF. This work was supported by a NSFGR fellowship (A.L.); NIH R01 GM084040 and Searles Scholar Award.(O.D.W.); Packard Fellowship, the Howard Hughes Medical Institute, and NIH grants GM55040, GM62583, EY016546 (NIH Roadmap Nanomedicine Development Centers).(W.A.L.); Pew Fellowship, the Office of Naval Research, Packard Fellowship, NIH EY016546, NIH AI067699, NSF BES-0547637, UC-Discovery, and the SynBERC NSF ERC (www.synberc.org).(C.A.V.)

Author Information Reprints and permissions information is available at npg.nature.com/reprintsandpermissions. The authors declare no competing financial interests. Correspondence and request for materials should be addressed to W.A.L. (lim@cmp.ucsf.edu).

Figure Legends

Figure 1 The phytochrome-APB interaction can be used to reversibly translocate proteins to the plasma membrane in a light-controlled fashion. **a**, apoPhyB covalently binds to the chromophore phycocyanobilin (PCB) to form a light-sensitive holoprotein. PhyB undergoes conformational changes between the Pr and Pfr states catalyzed by red and infrared light, reversibly associating with the PIF domain only in the Pfr state. **b**, This heterodimerization interaction can be used to translocate a YFP-tagged PIF domain to PhyB tagged by mCherry and localized to the plasma membrane by the C-terminal caax motif of Kras. **c**, Phytochrome and PIF domains functional in mammalian cells were tested by their ability to reversibly recruit YFP to the plasma membrane under

the action of red and infrared light. Of previously published PIFs, only the PhyB interacting 100aa N-terminus of PIF6 showed visible recruitment activity in mammalian cells with confocal microscopy; however, this recruitment was irreversible when recruited with the previously used PhyB(1-650). PhyB constructs harboring its tandem PAS repeat unique to the plant phytochromes were able to reverse the interaction under infrared light and free YFP back into the cytosol.

Figure 2 Confocal microscopy demonstrating the second-scale kinetics and photostability of the photoswitchable membrane recruitment system. **a**, Confocal microscopy of NIH3T3 cells reveals rapid whole cell translocation of YFP between cytosol and plasma membrane under red and infrared light. Fitting exponentials to the cytoplasmic depletion of YFP in these series gives typical time-constants of 1.3 ± 0.1 s for recruitment and 4 ± 1 s for dissociation ($n=3$). White rectangles show regions sampled for plotted traces. Arrows in graphs mark the timepoints shown. (Supplemental Movies 1,2) **b**, Rapid alternation between the two light frequencies can generate oscillations in the cytoplasmic concentrations of YFP. The absolute cytoplasmic concentration of YFP for this series is plotted along with the ratio change between time-points to adjust for photobleaching and cell-drift. The red and grey bars represent the standard deviations of the recruited and released cytosolic fluorescence, demonstrating near-fixed recruitment ratios over more than a hundred iterations. (Supplemental Movie 3) Scale bars $20 \mu\text{m}$.

Figure 3 Recruitment to the plasma membrane can be controlled spatially by simultaneously irradiating cells with patterned red and infra-red light. **a**, A nitrogen dye cell laser exciting a 650nm rhodamine dye was focused onto the sample plane of the microscope at 20Hz while IR-filtered white light continuously bathed the entire sample. **b**, A digital micromirror device focused onto the sample plane was used to send high-resolution patterns of 650nm/750nm light from a DG-4 source into the microscope under

software control. This results in complementary red and infra-red distributions on the sample plane. **c**, TIRF imaging of localized membrane recruitment by a point source as in **a** shows highly localized YFP recruitment. (Supplementary movie 4) The recruited YFP spot's diameter is roughly $3\mu\text{m}$ and can be quickly moved by repositioning the laser. The final frame shows that the YFP spot is not merely bleed-through of the excitatory laser light, but genuine local fluorescent protein recruitment. **d**, TIRF movies of structured membrane recruitment by programmatically updating masks for red and infrared light by a digital micromirror device as in **b** were collected, revealing a faithful reproduction in the recruited YFP distribution of a movie of the cellular automaton 'game-of-life glider' that was projected (Supplementary movie 5). **e**, Images show the raw traces of titrated input 650nm light and recruited PIF-YFP. The plot at left shows the recruitment level as a function of 650nm ratio for three typical experiments. Inset shows the non-saturated regime. Scale bars $20\mu\text{m}$.

Figure 4 Rho-family G-protein signalling can be controlled by the light-activated translocation system. **a**, The catalytic DH-PH domains of RhoGEFs Tiam and Intersectin activate their respective G-proteins Rac1 and Cdc42 which in turn act through effector proteins to modify the actin cytoskeleton. **b**, Recruitee constructs with Tiam DH-PH domains were assayed for their ability to induce lamellipodia in NIH3T3 by exposing serum-depleted cells transfected with the indicated constructs to red (650nm) light and counting the percentage of cells that produced lamellipodia within 20min under live microscopy. Error bars s.e.m., (n=2, avg. 30 cells; p-value=.0004 for Tiam) **c**, Local induction and 'extrusion' of lamellipodia in live NIH3T3 cells was demonstrated by globally irradiating the whole sample with a infrared (750nm) light source while focusing a red (650nm) laser onto a small portion of the cell as in **2a** and slowly extending this red-targeted region from the cell body. Superimposed outlines of the cell show directed extension $30\mu\text{m}$ along the line of light movement. (Supplemental Movie 7) **d**, Cdc42-

GTP binding domains linked to mCherry were used to measure the “response function” of Intersectin DHPH recruitment over several iterations in time and in space at equilibrium. (Supplemental Movie 11) Scale bars 20 μ m.

Figure 1

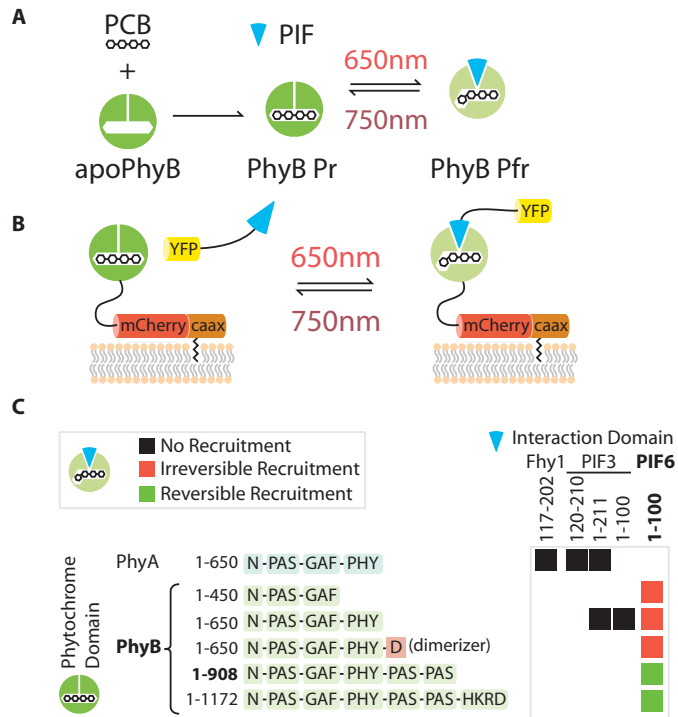


Figure 2

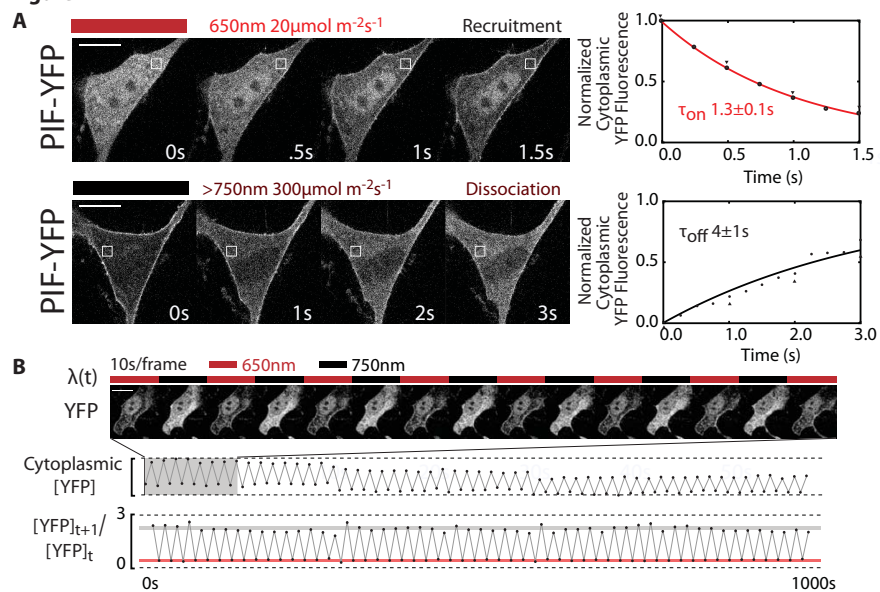


Figure 3

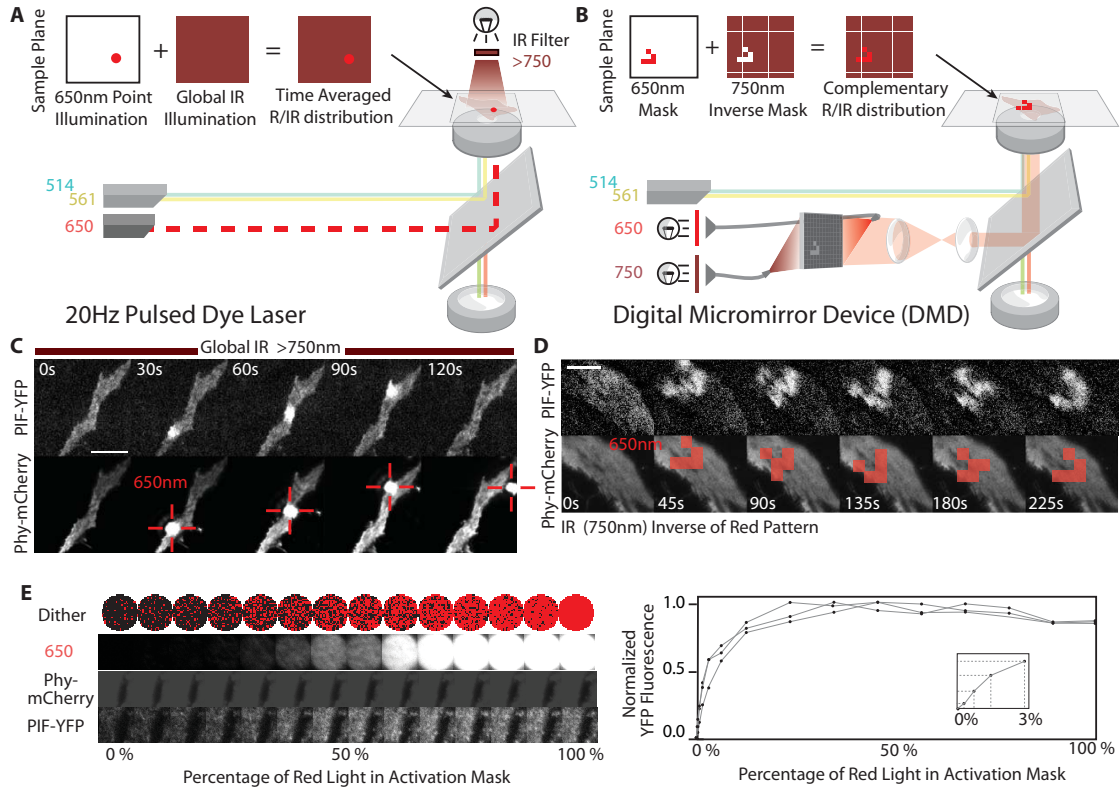
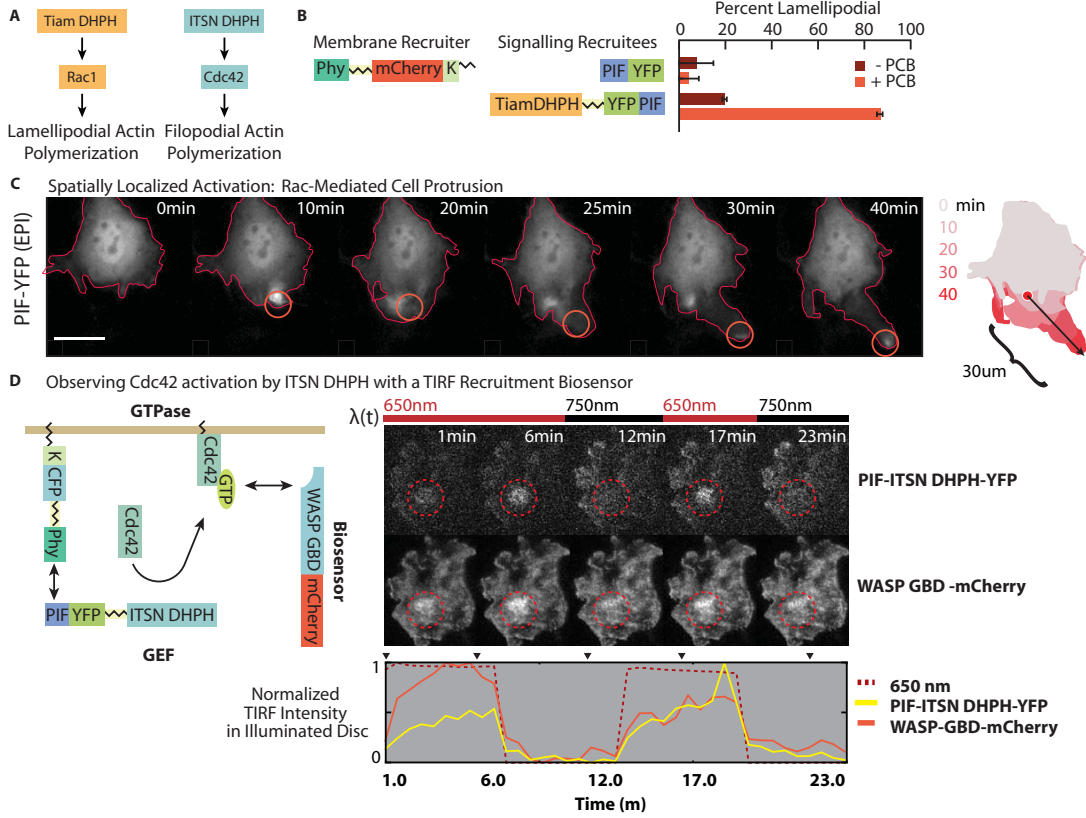


Figure 4



Spatiotemporal Control of Cell Signalling and Morphology Using a Genetically-Encoded Light-Switchable Interaction

Anselm Levskaya, Orion Weiner, Wendell A. Lim, Christopher A. Voigt

Supplementary Methods

Design and Construction of Plasmids. Most constructs were assembled whole by two-step overlap PCR and subcloned into the mammalian vector pcDNA3 or a modified version with a truncated SV40 promoter (10-fold lower expression relative to CMV). Unique cut-sites flanked most fused domains such that some constructs were assembled by replacing signalling domains via standard subcloning. (Complete plasmid sequences are available upon request.)

Table S1 Plasmids

| | | |
|--------|---|-----------------------|
| pAL113 | pCMV-PhyBNT(Y276H)-10aaLinker-mCFP-HrasCT | Fig. S1 |
| pAL161 | pCMV-PhyB(1-450)-10aaLinker-mCherry-Kras4BCT | Fig. 1c |
| pAL117 | pCMV-PhyB(1-650)-10aaLinker-mCherry-Kras4BCT | Fig. 1c |
| pAL148 | pCMV-PhyB(1-650)-Gal4DD-10aaLinker-mCherry-Kras4BCT | Fig. 1c |
| pAL149 | pCMV-PhyB(1-908)-10aaLinker-mCherry-Kras4BCT | ~All Figs, Movies 1-9 |
| pAL162 | pCMV-PhyBFL-10aaLinker-mCherry-Kras4BCT | Fig. 1c |
| pAL140 | pCMV-PhyA(1-650)-10aaLinker-mCherry-Kras4BCT | Fig. 1c |
| pAL139 | pCMV-mYFP-Fhy1CT | Fig. 1c |
| pAL138 | pCMV-PIF3APA-mYFP | Fig. 1c |

Supplementary Information

Levskaya, *et al.*

| | | |
|--------|--|---------------------------|
| pAL130 | pCMV-PIF3NT-mYFP | Fig. 1c |
| pAL100 | pCMV-PIF3APB-mYFP | Fig. 1c |
| pAL101 | pCMV-PIF6APB-mYFP | Fig. 1c,4b |
| pAL175 | pΔSV40-mYFP-PIF6APB | Fig. 2,3,S2 Movies 1-6,10 |
| pAL167 | pCMV-TiamDHPH-20aaLinker-mYFP-PIF6APB | Fig. 4b |
| pAL188 | pΔSV40-TiamDHPH-20aaLinker-mYFP-PIF6APB | Fig. 4c Movies 7,8 |
| pAL189 | pΔSV40-IntersectinDHPH-20aaLinker-mYFP-PIF6APB | Fig. 4d Movie 11 |
| pAL190 | pΔSV40-TimDHPH-20aaLinker-mYFP-PIF6APB | Movie 9 |
| pAL197 | pΔSV40-PakGBD-mCherry | Fig. S4 |
| pAL198 | pΔSV40-mCherry-WaspGBD | Fig. 4d Movie 11 |
| pAL204 | pCMV-PhyB(1-908)-10aaLinker-mCFP-Kras4BCT | Fig. 4d Movie 11 |

Phytochrome, PIF domains PhyB-CBD (PhyB450NT), PhyB-NT (PhyB650NT), PhyB-908NT, and PhyB-FL domains were amplified by PCR from vector PhyBFL-GBD; this vector contains full-length phyB [Entrez Gene ID: 816394] cDNA from *Arabidopsis thaliana*. PhyA-NT (1-650) was cloned from previously subcloned cDNA. PIF3NT, PIF3APA (aa120-210), PIF3APB (PIF3-100NT) and PIF6APB (PIF6-100NT) domains were amplified by PCR from vectors PIF3-GAD and PIF6APB, respectively; these vectors contain subsequences of the PIF3 [Entrez Gene ID: 837479] and PIF6 [Entrez Gene ID: 825382] genes from *Arabidopsis thaliana*. All three vectors were gifts from Peter Quail. *Arabidopsis* Fhy1CT(117-202) [Entrez Gene ID: 5007942] was amplified from *Arabidopsis thaliana* cDNA.

Linker domains The linker domains used are standard polyglycine-serine flexible linkers and were made by oligo annealing: 10aa-linker: DSAGSAGSAG [gat agt gct ggt agt gct ggt agt

gct ggt], 20aa-linker: SAGGSAGGSAGGSAGGSAGG [agt gct ggt ggt agt gct ggt ggt agt gct ggt ggt agt gct ggt ggt agt gct ggt ggt]

Dimerization domain The Gal4 dimerization domain¹ (residues 50-106) was cloned from a *Saccharomyces cerevisiae* cDNA library.

Localization domains Small C-terminal localization tags were created by oligo annealing: Hras [Entrez Gene ID: 3265] palmitoylation CaaX sequence (GCMSCKCVLS), [ggc tgc atg agc tgc aag tgt gtg ctc tcc], Kras4B [Entrez Gene ID: 3845] polybasic CaaX terminus (KKKKKKSKTKCVIM) [ggt aaa aag aag aaa aag aag tca aag aca aag tgt gta att atg]

Fluorescent Proteins mCFP and mYFP (ECFP and EYFP with monomerizing A206K mutation) were amplified by PCR from Invitrogen vectors. mCherry was amplified by PCR from vector supplied by Rogen Tsien.

RhoGEFs DHPH domains from human RhoGEFs Tiam [Entrez Gene ID: 7074], Intersectin [Entrez Gene ID: 6453], and Tim [Entrez Gene ID: 7984] were amplified by PCR from vectors carrying previously subcloned copies of these cDNAs.

Mammalian Promoters The standard CMV promoter from the pcDNA3 vector was used in most constructs. In some plasmids a truncated sv40 promoter was used instead to lower expression levels of recruitee constructs in transiently transfected cells (10-fold lower expression than CMV).

Phycocyanobilin (PCB) Purification. 50g *Spirulina* powder (Seltzer Chemical) was resuspended in 1.5L doubly distilled water (30mL/g), stirred for 10minutes, then spun at 8000rpm at 4°C for 1 hour. The dark green cell pellet was discarded and the cyan supernatant was treated with 15g TCA (1% w/v) to precipitate soluble protein. This solution was stirred at

4°C in the dark for an hour then spun at 8000rpm at 4°C for 10 minutes. The pellet was resuspended and washed three times by adding 1.5L methanol and spinning at 8000rpm for 10 minutes at 4°C to remove free tetrapyrroles (repeated until supernatant was clear). Great care was taken from this point on to shield the free PCB-containing mixtures from all light by wrapping glassware in aluminum foil or by using a green safelight (Sylvania F40G fluorescent tube wrapped once with a Roscolene 874 sheet and once with a Roscolene 877 sheet, 550nm) in a darkroom. The washed cyan pellet was collected and subjected to methanolysis in 500mL methanol by refluxing at 70°C for eight hours. To increase the yield the remaining pellet was subjected to a second, identical methanolysis for a second pool that was further handled in parallel with the first. Each methanolysis extraction was evaporated to 50mL using a roto-evaporator. This concentrated PCB solution was extracted twice with 50mL chloroform and 100mL water, the chloroform layers were removed with a separatory funnel and dried with a roto-evaporator to a dry residue. The residue was resuspended in 3mL DMSO, aliquoted and stored at -80°C. The final PCB concentration was quantified by spectroscopy by diluting the DMSO stock 1:100 into 1mL MeOH:HCl(37.5%) 95%:5% solution and reading the absorbance at 680nm. The concentration in mM was calculated as $A_{680} \times 2.64$, typical final concentrations were 3-15mM.

Cell culture and transfections. NIH3T3 cells were obtained from ATCC and maintained in DMEM supplemented with 10% (v/v) BCS, glutamine, and antimicrobials at 37°C in a humidified, CO₂-controlled (5%) incubator. For experiments, 120,000 NIH3T3 cells were plated on poly-d-lysine coated glass-bottomed petri dishes (Mattek) before transfection. Transfections were performed with Lipofectamine 2000 (Invitrogen) at a 3:1 $\mu\text{L}/\mu\text{g}$ ratio of reagent to DNA, mixed in Optimem (Invitrogen) for 25 minutes and added directly to cells for five hours before washing reagent out with serum-containing media. Microscopic observations took place at least twelve hours post-transfection. Serum depletion was performed where indicated by dilution of serum-containing media by DMEM supplemented with 1% (w/v) fatty-

acid free BSA, followed by at least six hours of depletion. PCB was added to cells under green safelight at least half an hour before experiments by prediluting the concentrated DMSO stock in BSA-supplemented DMEM and then adding to cells for a final concentration of 5 μ M. This weakly fluorescent PCB-containing media was swapped immediately before imaging with mHBSS [150mM NaCl, 4mM KCl, 1mM MgCl₂, 10mM glucose, 20mM Hepes pH 7.2] supplemented by 1% fatty-acid free BSA.

Global Recruitment Assays. Global recruitment assays were performed at 37°C on a spinning disk confocal microscope consisting of a Nikon TE2000-U inverted microscope surrounded by a temperature-control chamber, equipped with a Yokogawa CSU22 confocal scanning unit (Solamere Technology Group) using Ar and Ar/Kr laser lines at 568nm, 488nm and emission filters for YFP and mCherry (Nikon 100x Apochrom 1.49NA). Images were captured with a Photometrics Cascade II EMCCD camera. Cells were exposed to activating or deactivating wavelengths by filtering brightfield light with either a 650nm 20nm-bandpass filter (Edmund Optics) or a near-IR RG9 glass filter (Newport). Total photon fluence was measured at the sample plane by using a portable calibrated fiber-optic spectroradiometer (EPP2000C, Stellarnet Inc). To measure kinetics of recruitment and release, cells were exposed to fixed periods of red or infrared light, the π -YFP distribution was imaged, then the ϕ - π pool was returned to fully-recruited or fully-released equilibrium by exposure to 10s of the opposite wavelength of light, then exposed again for a longer fixed period of the original wavelength in a loop. Such iterative measurements are necessary to eliminate the strong activating perturbations induced by the imaging light itself.

Localized Recruitment and Signal Induction. Localized recruitment assays were performed at 37°C using total internal reflectance (TIRF) microscopy on a Nikon TE2000E inverted microscope surrounded by a temperature-control chamber, equipped with a Nikon laser TIRF illuminator (Nikon 60x Apochrom 1.49NA). Ar laser lines 488nm, and 514nm and solid state 561nm lasers were used through a LEP MAC5000 shutter system. Images were collected with a

Photometrics Cascade II EMCCD camera. Local induction was performed with a MicroPoint microscope laser system (Photonic Instruments) using a pulse UV-pumped Rhodamine 650nm dye cell laser. The illumination point was made parfocal with microscope optics by test-ablation of a metal-sputtered glass slide. To locally recruit fluorescently tagged signalling factors, continuous 20Hz pulses of the 650nm light at low intensity were centered on a patch of plasma membrane while simultaneously irradiating the whole cell with inhibitory IR light from a brightfield source at maximal intensity filtered by an RG9 IR long-pass glass filter (Newport).

Patterned Membrane Recruitment Recruitment of YFP-tagged APB to patterned regions of the cell membrane was performed at room temperature using total internal reflectance (TIRF) microscopy on a Nikon TE2000E inverted microscope equipped with a Nikon laser TIRF illuminator (Nikon 60x Apochrom 1.49NA). Ar laser lines 488nm, and 514nm and solid state 561nm lasers were used and emission light filtered by a Sutter Lambda 10-3 Filter Wheel. Images were collected with a Photometrics Cascade II EMCCD camera. To produce patterned Red/IR profiles at the cell surface, alternating 650nm and 750nm light was produced using 20nm bandpass filters (Chroma) with a broad-spectrum arclamp in a Lambda DG-4 source. These wavelengths were patterned by use of a commercial digital micromirror device brought into a conjugate focal plane with the sample. (Mosaic Digital Diaphragm, Photonic Instruments) The illumination frequencies were switched at the maximum update speed for the device, which was roughly 8Hz. Illumination, acquisition and light patterning of the glider motif were orchestrated by a custom script written in Metamorph.

Morphological Induction Assays. Morphology induction assays were performed by exposing cotransfected, PCB-preincubated (30min) or PCB-free control cells to red light while observing on a Nikon TE2000E inverted microscope in widefield with a 514/561 dichroic mirror and YFP and mCherry channel emission light filtered by a Sutter Lambda 10-3 Filter Wheel. Images were collected with a Photometrics Cascade II EMCCD camera. The constructs were scored by

counting the percentage of cotransfected cells exhibiting lamellipodia within the twenty-minute observation window.

Spot Titration and TIRF Recruitment Biosensor Assays. Localized TIRF biosensor recruitment assays were performed at RT using total internal reflectance (TIRF) microscopy on a Nikon Ti inverted microscope equipped with a Nikon laser TIRF illuminator (Nikon 100x Apochrom 1.49NA). Ar laser lines 488nm, and 514nm and solid state 440nm, 561nm lasers were used through a LEP MAC5000 shutter system. Images were collected with a Andor iXon EMCCD camera. Local induction was patterned by use of a commercial digital micromirror device brought into a conjugate focal plane with the sample. (Mosaic Digital Diaphragm, Photonic Instruments) This micromirror array device was custom modified to allow two input light sources such that both ‘on’ and ‘off’ mirror states were used to reflect 650nm and 750nm light into the optical axis of the microscope simultaneously.

Supplemental Calculation Membrane Capture Time Constant for Perfect Spherical Absorber

An approximate time constant for capture of molecules diffusing in a cell with diffusion constant D to a perfectly absorbing spherical membrane (radius R) can be easily calculated by solving the poisson equation for the “mean-first-capture-time field”.²

Mean time equation for a particle encountering a non-attracting boundary for the first time by diffusion (diffusion constant D):

$$D\Delta W + 1 = 0$$

W is mean time to encounter (shown by electrostatic analogy). Solving this equation for the inside of a spherical cell of radius R yields a solution of the form:

$$B - A/r - r^2/(6D)$$

Boundary conditions (mean-capture-time at $r=R$ is zero, continuity requires derivative must be zero at origin) fix constants for a solution:

$$(R^2 - r^2)/(6D)$$

Averaging this value over the inside of the spherical cell yields an approximation for the time constant for membrane capture:

$$R^2/(15D)$$

For typical cell values: (20 μm cell diameter, 30 $\mu\text{m}^2\text{s}^{-1}$ D for cytoplasmic GFP) this equals **.22 seconds**. Given that this calculation assumes capture at the *first* membrane-encounter it serves as a lower bound.

Supplemental Movies

(Movies are also available for viewing with any flash-enabled web-browser at the URL:
<http://www.anselmlevskaya.com/phygif-movies.html>)

1 YFP membrane recruitment Cytosolic PIF-YFP is recruited onto the membrane by PhyB under the action of 650nm light. A confocal slice of a NIH3T3 cell is shown.

2 YFP membrane dissociation Membrane-bound PIF-YFP is released back to the cytosol by PhyB under the action of >750nm light. A confocal slice of a NIH3T3 cell is shown.

3 oscillating YFP translocation The photostability of the system is shown by repeated rounds of recruitment and release of PIF-YFP to and from the membrane by PhyB under action of oscillating 650nm and IR (>750nm) light.

4 YFP point recruitment PIF-YFP is recruited to a single, moving point by action of a focused 650nm laser with global inhibition by >750nm irradiation. The membrane of a NIH3T3 cell is shown using TIRF microscopy.

5 patterned recruitment of YFP PIF-YFP is recruited in a patterned fashion to the plasma membrane. Sequential frames of a movie of a “glider” pattern from the “game of life” cellular automaton is projected onto the membrane as an inverse R/IR light distribution. The membrane of a NIH3T3 cell is shown using TIRF microscopy.

6 titrated recruitment of YFP PIF-YFP is recruited to a circular region on the plasma membrane. The time-average ratio of 650nm-reflecting pixels from the micromirror array is steadily increased by dithering the illumination mask with rapidly updating white noise with pixel densities that increase with each frame (resulting in a steady time average increase). The amount of Pfr PhyB, and thus recruited YFP is thereby titrated.

7 cell extrusion by Tiam(Rac GEF) recruitment An extended process from a cell is induced and guided by locally stimulating Rac1 via membrane-recruited Tiam(Rac GEF) DHPH. A NIH3T3 cell is shown using standard epifluorescence microscopy.

8 dynamic lamellipodia by Tiam(Rac GEF) recruitment Lamellipodia are induced and released on a physiological timescale by local Tiam(Rac GEF) recruitment, showing the quick responsiveness of the system. A NIH3T3 cell is shown using standard epifluorescence microscopy.

9 periodic contractions by Tim(Rho GEF) recruitment Alternating global irradiation of NIH3T3 cells transfected with a Tim (Rho GEF) DHPH recruitee construct causes rhythmic contractions of the cell tightly coupled to the light condition. A NIH3T3 cell is shown using standard epifluorescence microscopy.

10 PIF-YFP only recruitment control This movie shows the typical result that pif-YFP recruitment alone does not seem to produce any detectable polymerization or ruffling activity in the cytoskeleton. (Such spurious morphological effects have not been seen in any of our YFP-only system characterization experiments.)

11 monitoring membrane-bound Cdc42-GTP dynamics via recruited mCherry-WASP-GBD in TIRF A small circular region of a NIH3T3 cell's plasma membrane is illuminated off and on with red light. Phy-pif recruitment of IntersectinDHPH to the plasma membrane causes it to bind and activate Cdc42 by inducing nucleotide

exchange to the GTP bound form. The WASP GBD domain specifically recognizes this form and is preferentially recruited to regions of high Cdc42-GTP content. By exploiting this fact in TIRF mode we can monitor the downstream effects of GEF activity in NIH3T3 cells.

Supplemental References

1. Hidalgo *et al.* Recruitment of the transcriptional machinery through GAL11P: structure and interactions of the GAL4 dimerization domain. *Genes Dev* **15**, 1007-20 (2001).
2. Berg, Howard C. Random Walks in Biology. Princeton University Press (1993).

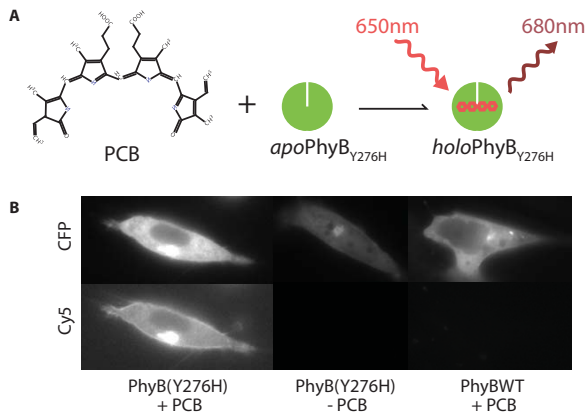


Figure S1 PhyB-PCB holoprotein formation was tested in live mammalian cells by epi-fluorescence microscopy. **A** PhyB Y276H mutant forms a bright far-red fluorophore upon conjugation to PCB chromophore. Free PCB and wildtype holoprotein are only very weakly fluorescent. **B** Images of CFP-tagged membrane-localized phytochrome constructs in NIH3T3 cells. PCB-free and wildtype PhyB controls show no fluorescence above background in Cy5 channel, whereas PhyB(Y276H) pre-incubated with PCB shows bright membrane localized fluorescence after 30min 5 μ M PCB incubation at 37C, showing rapid formation of holoprotein in living cells at standard conditions.

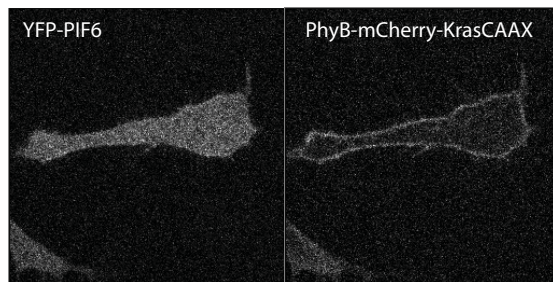


Figure S2 Confocal images of unrecruited YFP-PIF6apb and PhyB908-mCherry-KrasCAAX constructs showing their respective (uninduced) cytosolic and plasma-membrane localizations in NIH3T3 cells a day post-transfection.

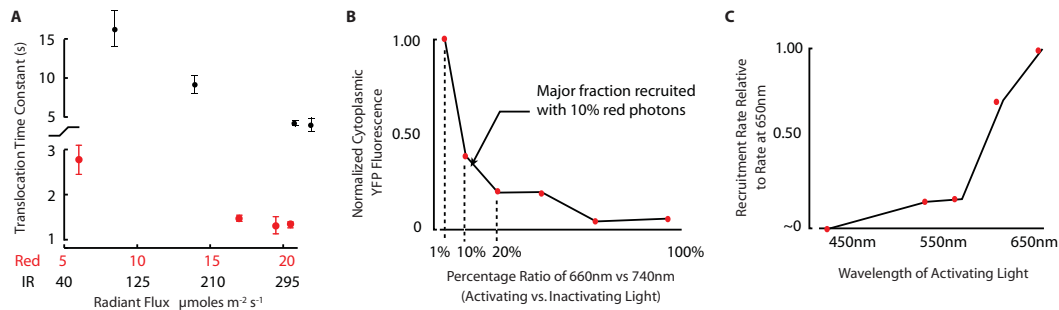


Figure S3 Quantitative characterization of the effects of light strength and quality were measured for the PhyB908-PIF6APB pair. **a**, The photon flux was titrated to test for saturation of the phytochrome pool. For red light, saturation appears to occur at around $20 \mu\text{moles m}^{-2} \text{s}^{-1}$, even laser activation (with significantly higher fluxes) does not speed membrane translocation. For infrared reverse stimulation it is not clear that saturation occurred with the low intensity infrared sources used in our experiments. Stronger infrared light (for instance, in 2-photon microscopy) could drive even faster “OFF” kinetics and tighten the ultimate spatial resolution of recruitment. (error bars s.e.m., $n=3$) **b**, The fraction of red photons in combined red and infrared illumination necessary to activate the phytochrome pool was measured by varying intensities of calibrated LEDs at 640nm and 740nm. A 10% fraction of red light was sufficient to activate a major fraction of the phytochromes at equilibrium. **c**, Relative rate of recruitment under various wavelengths of light of approximately equivalent intensity as determined by cytoplasmic depletion. Blue light is nearly two orders of magnitude less efficient at inducing phytochrome activation than red light.

Following Rac1 activation by recruited TIAM DHPH with a TIRF Recruitment Biosensor

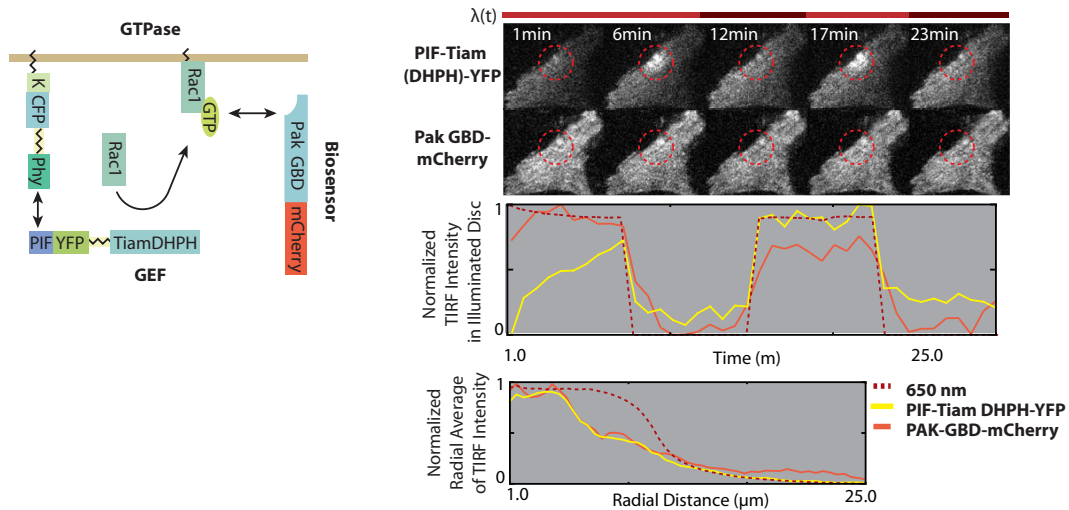


Figure S4 Response dynamics of Rac1-GTP monitored by use of a TIRF recruitment biosensor. Left panel depicts the activation (nucleotide exchange) of Rac1 to its active, GTP-bound form. mCherry-labelled PAK GBD domain binds specifically to the GTP-bound form of Rac1 and is thereby concentrated near localized sources of GEF activity. Microscopy panels show TIRF images of Tiam DHPH-YFP-PIF and PAK-GBD-mCherry. The PAK-GBD-mCherry increase at the point of red-light activation is subtle visually but easily followed by tracing the integrated intensity of the region. Plots show the overall rapid behavior in time within the illuminated region as the red light is turned on and off and the relative spatial distribution of DHPH and sensor during the first “activation peak”.

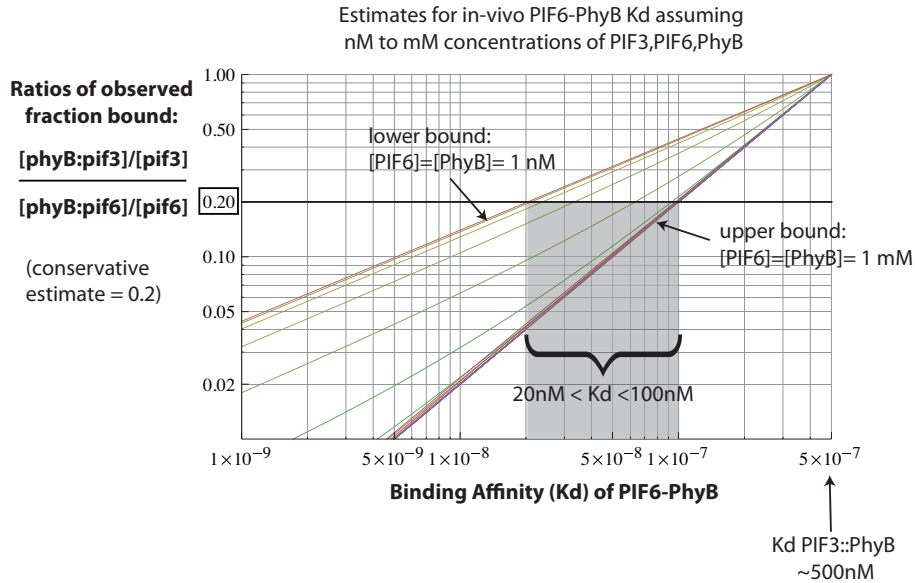


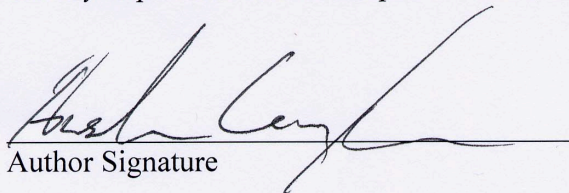
Figure S5 Conservative bounds for the K_d for the PIF6::PhyB interaction can be obtained by comparing the experimental membrane/cytoplasmic fraction ratios of YFP-PIF6 and YFP-PIF3 from identical experimental designs. The steady-state recruitment levels depend on few parameters: 1) the total concentration of membrane-localized phytochrome, 2) the total concentration of cytosolic PIF-YFP, 3) the K_d . Assuming equal physiological concentration ranges, we can compare relative equilibrium recruitment levels to bound the relative K_d s. Even overestimating the baseline degree of PIF3-PhyB recruitment to be 50% and underestimating the recruitment level of PIF6-PhyB to be only 84% yields a relative $K_d[\text{pif6:phyB908}]/K_d[\text{pif3:phyB908}]$ that is 5-10x fold lower. Using the previously measured value of $\sim 500 \text{ nM}$ for PIF3::PhyB, our interaction's K_d would then be bounded below 100-50nM.

Publishing Agreement

It is the policy of the University to encourage the distribution of all theses, dissertations, and manuscripts. Copies of all UCSF theses, dissertations, and manuscripts will be routed to the library via the Graduate Division. The library will make all theses, dissertations, and manuscripts accessible to the public and will preserve these to the best of their abilities, in perpetuity.

Please sign the following statement:

I hereby grant permission to the Graduate Division of the University of California, San Francisco to release copies of my thesis, dissertation, or manuscript to the Campus Library to provide access and preservation, in whole or in part, in perpetuity.


Author Signature

8/11/09
Date